BOSTON UNIVERSITY

GRADUATE SCHOOL OF ARTS AND SCIENCES

Dissertation

EFFECTS OF CONFINEMENT ON THE THERMODYNAMICS OF SUPERCOOLED WATER

by

ELENA G. STREKALOVA

B.Sc., University of Massachusetts Boston, 2006
M.S., University of Massachusetts Boston, 2006
M.A., Boston University, 2011

Submitted in partial fulfillment of the
requirements for the degree of
Doctor of Philosophy
2012

Approved by

First Reader

H. Eugene Stanley, Ph.D.
University Professor and Professor of Physics
Boston University

Second Reader

Giancarlo Franzese, Ph.D.
Professor of Physics
Universitat de Barcelona

I dedicate this dissertation to my parents who stood by me every step of the way and whose belief in me gave me the strength and courage to persevere.

Acknowledgments

First, I would like to acknowledge my parents, Larisa and Gennady, for raising me to value education and for supporting me in all my endeavors. The boundless love and support they have given me over the years was the greatest gift anyone has ever given me. I thank you for caring and praying for me, despite my success or failure.

Next, I would like to acknowledge my husband, Ilya, for his constant love, eternal optimism and strength. His unconditional support gave me inspiration throughout the research development. I thank you for encouraging me to give my best effort.

My deepest gratitude is to my advisor, Professor H. Eugene Stanley, for accepting me into his scientific family, for his perpetual encouragement, continuous trust, constant support, and strong influence throughout all my research development. Your passion for pursuing scientific beauty is contagious and it has been a great privilege for me to work with you and learn from your experience. I am also grateful for your kindness and warmth.

I would like to express my sincere acknowledgement to Professor Giancarlo Franzese for going above and beyond his role as a coadvisor. I thank you for your insightful guidance and support.

I am deeply grateful to Professor Sergey Buldyrev, who has taught me so much and without whom, I have never gotten to where I am today.

I thankfully acknowledge Marco Mazza, who helped me throughout this long journey, who was always there to listen and provide advice. You helped me get started in the group and passed me your experience. I would have never made it all the way to the end without your guidance, friendship and warm hearted help.

I am deeply thankful to Dario Corradini for fun collaboration, valuable advice, and all the time that he spent in front of my computer always ready to help. You have such a wonderful ability in turning even the most boring work into pleasant experience.

I am also thankful to the Boston University Department of Physics faculty for the quality of education they have provided me. In particular, I would like to thank Professor Sid Redner for his excellent courses on statistical mechanics.

I wish to thank Plamen Ichanov, Dario Corradini, Paola Gallo, Jiayuan Luo, Kevin Stokely, Erik Lascaris, Sungho Han, Jerry Paul, Bob Tomposki, Jerry Morrow, Mirtha Cabello for being a unique family that have supported me during my doctoral studies at Boston University.

EFFECTS OF CONFINEMENT ON THE THERMODYNAMICS OF SUPERCOOLED WATER

(Order No.)

ELENA G. STREKALOVA

Boston University Graduate School of Arts and Sciences, 2012

Major Professor: H. Eugene Stanley, University Professor and Professor of Physics

ABSTRACT

The main focus of this thesis is to understand how confinement alters the phase diagram of supercooled liquid water by employing methods of statistical mechanics and numerical simulations.

Water is very complex and anomalous when compared to simple liquids. For example, experimental data for liquid water reveals the presence of a temperature of maximum density (TMD) below which the density decreases under isobaric cooling. Another anomaly is the hypothesized liquid–liquid phase transition (LLPT) between two types of liquid water with different densities. In this thesis we study how confinement affects such anomalies as TMD and LLPT in supercooled liquid water.

This thesis is separated into three parts: (i) Monte Carlo simulations of a 2D coarse-grained model of a water layer confined in a fixed disordered matrix of hydrophobic nanoparticles, (ii) molecular dynamics simulations of a Jagla ramp model of liquid confined in fixed ordered and disordered matrices of hydrophobic nanoparticles, and (iii) all-atom simulations of trehalose and maltose in aqueous solution of lysozyme.

In Part (i), we perform Monte Carlo simulations and find that a nanoparticle concentration as small as 2.4% is enough to destroy the LLPT for pressure $P > 0.14$ GPa. Moreover, we find a substantial (more than 90%) decrease of compressibility, thermal expansion coefficient and specific heat at high P and low temperature T upon increase of nanoparticle concentration from 0% to 25%.

In Part (ii), we ask how, for single component systems interacting via a soft-core isotropic potential with two characteristic length scales, the geometry of hydrophobic confinement affects the phase diagram. We use molecular dynamics simulations to study

particles interacting through a ramp potential and a shoulder potential, each confined in a fixed matrix of nanoscopic particles with a fixed volume fraction. We find a substantial weakening of the LLPT and the disappearance of TMD upon the increase of disorder in the confining geometry.

In Part (iii), we study aqueous systems with all-atom simulations. We are currently investigating the mechanism of water-trehalose-protein and water-maltose-protein interaction upon supercooling for its relevance to bioprotection.

Contents

List of Figures

List of Abbreviations

CPF	Critical-Point Free
CUBE	Perfect Cubic Lattice
DIST	Cubic Lattice with Gaussian Distortions
DMD	Discrete Molecular Dynamics
HB	Hydrogen Bond
HS	Hard Spheres
HDA	High Density Amorphous Ice
HDL	High Density Liquid
LDA	Low Density Amorphous Ice
LDL	Low Density Liquid
LLCP	Liquid–Liquid Critical Point
LLPT	Liquid–Liquid Phase Transition
LMS	Limit Mechanical Stability
MC	Monte Carlo
MD	Molecular Dynamics
MF	Mean Field
NMR	Nuclear Magnetic Resonance
n.n.	Nearest Neighbor
NPs	Nanoparticles
NPT	Constant Pressure Constant Temperature
QENS	Quasi–Elastic Neutron Scattering

RF	Random Field
RND	Random
SF	Singularity–Free
SL	Stability Limit
TMD	Temperature of Maximum Density
TminD	Temperature of Minimum Density
VHDA	Very High Density Amorphous Ice

Part I

Introduction

Chapter 1

Water: A Mysterious And Complex Liquid

Water is so ubiquitous in our everyday lives that we tend to think about it as an ordinary colorless, odorless and testeless liquid. Moreover, we easily forget that this simple compound of one oxygen and two hydrogen atoms has a complex and crucial relationship with our lives. Liquid water is an extraordinary substance without witch life itself would not exist [1]. Water is not only a special medium in which most biological processes take place, it controls every aspect of life [3, 289]. It is often called the universal solvent that provides a liquid environment for biochemical reactions. It also acts as a temperature buffer, a metabolite, and a living environment for aquatic life. In addition, water is the medium of exchange and transport in living things.

The phase diagram of water is very complex with the extraordinary number of phases and stands out among other liquids. Stable phases of water include the vapour phase, the liquid phase and twelve different forms of solid phases, of which ordinary hexagonal ice Ih is the most common (at ambient pressure). Beyond stable phases, water can be found in metastable phases. These can be solid phases, both crystalline and amorphous and liquid phases. While most substances are present in only one phase at Earth's ordinary temperatures and atmospheric pressure, water occurs naturally in all three phases of matter: solid, liquid, and vapour, and it is common to have all three phases coexisting together at the same time.

Water is also the most abundant substance on Earth [4, 203]. It is so plentiful that we call Earth the “blue planet”. It covers three-fourth of the planet’s surface. Water is also in constant motion around us, carried around by storms, currents, and tides [5]. It frequently falls from the sky as rain, snow, or ice. As for the living world, water constitues about 60% by weight of all the living organisms.

1.1 Water is not a typical liquid

The abundance of water is not the only extraordinary phenomenon. Water is also special because of its comlex and puzzling behaviour. Many authors have pointed out that life on Earth strongly depends on the anomalous properties of water [4, 54, 203]. In particular the melting point and the boiling point can be found at temperatures much higher with respect to other hydride compounds of atoms of Group 6A in the periodic table, such as H_2S, H_2Se, H_2Te, H_2Po. This allows Earth to be bathed by liquid water.

The anomalies of water have been subject of intense studies for decades. One, well known anomaly, the density maximum at 277 K and atmospheric, dates backs to the seventeenth century [6]. Fig.1.1 shows that density of liquid water as a function of temperature T at different pressures displays maxima. The locus of the temperature at which the density is maximum at a given pressure is reffered to as the temperature of maximum density (TMD). From the TMD, the liquid water expands upon cooling and heating. The presence of the maximum density is referred to as the “density anomaly”, since for the vast majority of liquids the density decreases monotonically as T is lowered.

The density anomaly is crucial for the inhabitants of rivers, lakes, and oceans since it prevents water from freezing bottom to top. Instead, the freezing proceeds from top down, so that the layers of ice formed at the interface with air insulates the bottom body of water, preventing further freezing and allowing the survival of living organisms.

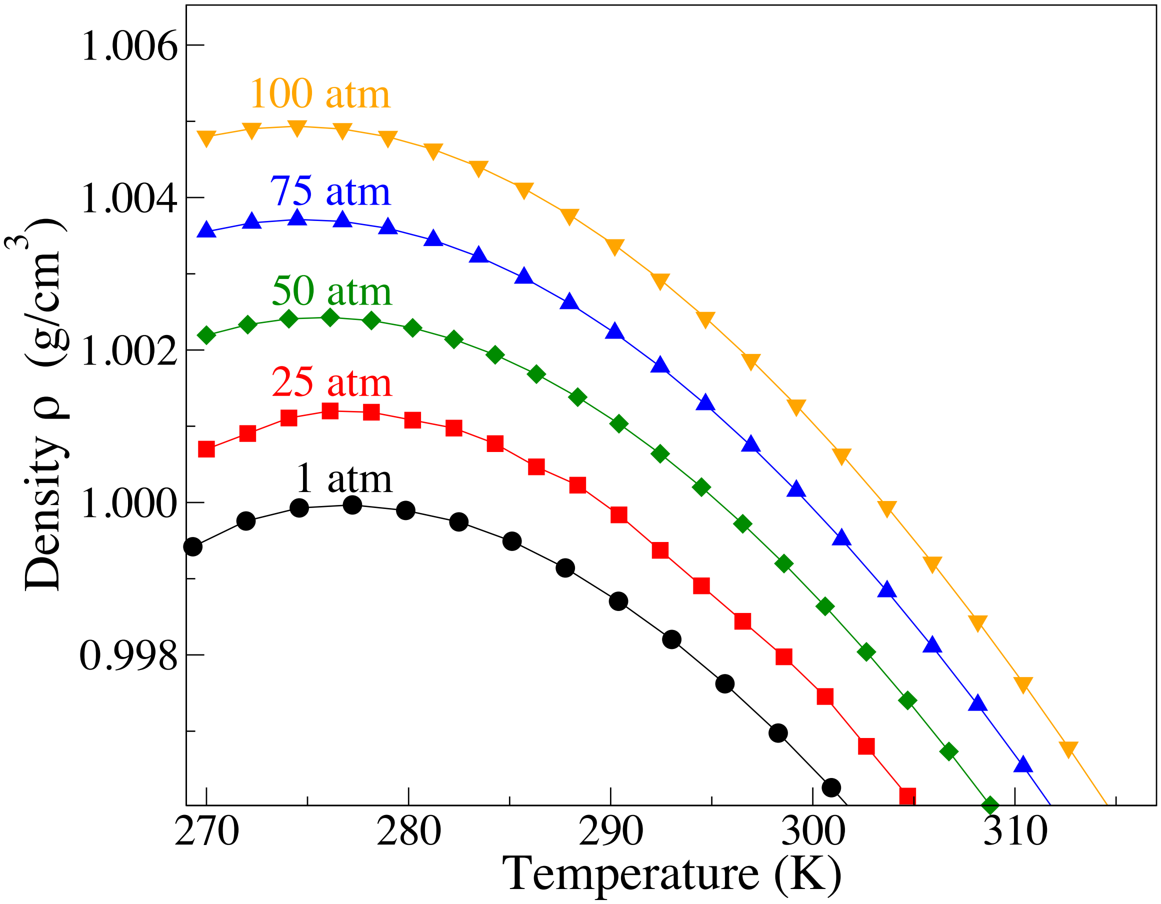

Figure 1.1: Density of liquid water as a function of temperature at 1 atm (black circles), 25 atm (red squares), 50 atm (green diamonds), 75 atm (blue triangles up), and 100 atm (orange triangles down). For pressures presented here, density of water displays the temperature of maximum density (TMD) wich is referred to as the "density anomaly". Data adapted and reploted from Ref. [7, 8]

1.2 Thermodynamic anomalies

Density anonomaly is not the only fascinating and crusial to life anomaly. Its high heat capacity allows temperature regulation on Earth. Water has a high specific heat capacity and it takes a lot of heat to raise its temperature. As the result, water can absorb a lot of heat without large temperature fluctuations in the environment and in living organisms. To date, sixty seven anomalies have been recognized, among which are phase anomalies, density anomalies, material anomalies, thermodynamic anomalies, and dynamic anomalies [1].

It is important to realize that liquid water's anomalies become more pronounced as temperature is lowered below the melting line, in the supercooled region [25]. Moreover, many thermophysical properties of supercooled liquid water exhibit a temperature dependence. At atmospheric pressure water's response functions, responce of volume V or entropy S to pressure or temperature perturbations, increase in magnitude with decreasing temperature [9, 52].

For instance, the isothermal compressibility K_T [Fig. 1.1(a)], associated with volume fluctuations [10].

$$\langle(\delta V)^2\rangle = V k_B T K_T \tag{1.1}$$

At ambient pressure the isothermal compressibility decreases at high temperatures, reaches a minimum around $T = 319$ K and then it increases rapidly, and appears to diverge in the supercooled region [Fig.1.2(a)]. The minimum of K_T moves to lower temperatures, when pressure is increased. In a simple liquid the isothermal compressibility decreases monotonically with decreasing temperature.

Another example of the thermodynamic response function is the isobaric heat capacity C_P [Fig.1.2(b)] which is characterized by the entropy fluctuations experienced by N molecules at fixed pressure.

$$\langle(\delta S)^2\rangle = N k_B T C_P \tag{1.2}$$

Intuitively, C_P should decrease upon decreasing temperature, as it is observed in typical liquids. In the case of water, instead, it increases upon cooling under atmospheric pressure for $T < 308$ K, and seems to diverge with a power-law at a lower temperature [9].

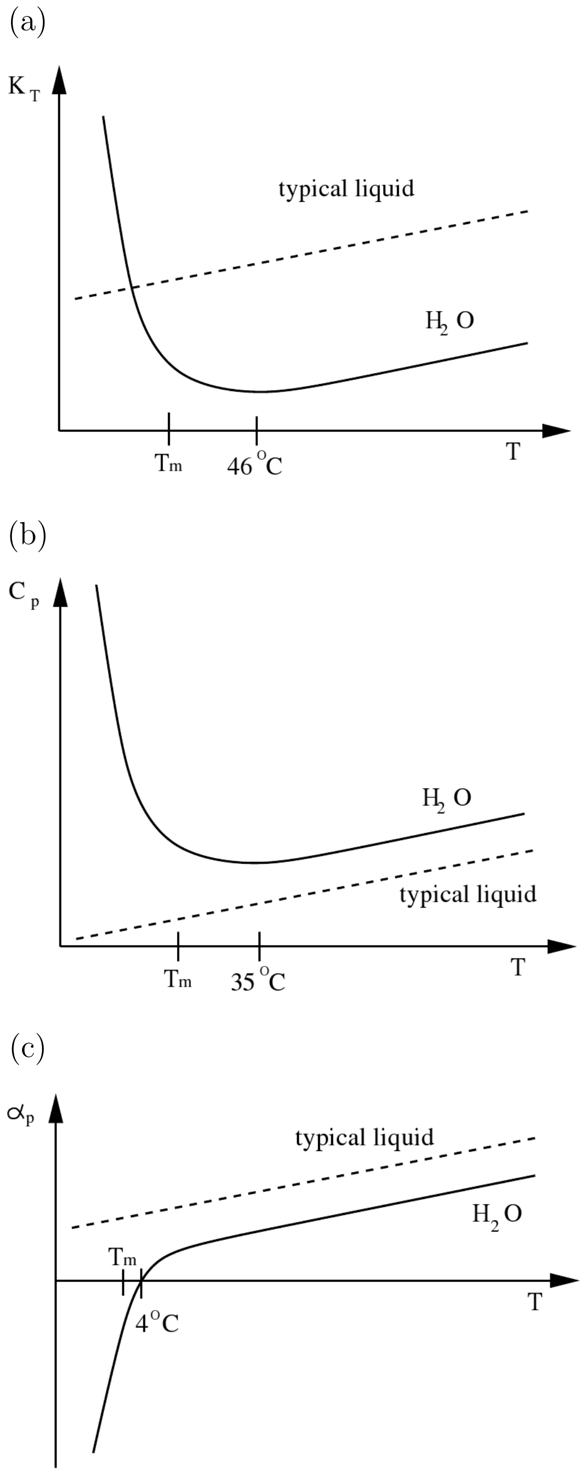

Figure 1.2: Schematic temperature dependence of (a) the isothermal compressibility K_T, (b) the isobaric heat capacity C_P, and (c) the coefficient of thermal expansion α_P. The behavior of a typical liquid is also shown with a dashed lines. Adapted from Ref. [9, 11, 52].

In addition, the coefficient of thermal expansion α_P [Fig.1.2(c)] which is the measures the cross-correlations of entropy and volume.

$$\langle(\delta S \delta V)\rangle = V k_B T \alpha \tag{1.3}$$

For typical liquids, α_P is positive becuase of the positive correlation of entropy and volume fluctuations, an increase in volume is accompanied by the increase in entropy. In water, on the other hand, α_P is negative below 277 K, where the fluctuations of entropy and volume are anti-correlated as the result of the formation of an open hydrogen bonded network for which a decrease in orientational enthropy is accompanied by an increase in volume.

This anomalous behavior is suddenly interrupted by crystallization for $T < 235$ K. This temperature is named *homogeneous nucleation temperature* T_H at ambient pressure [12]. It must be noted that the homogeneous nucleation temperature is a kinetic limit and not a thermodynamic one. As thus it can be considered as a practical limit, function of the cooling rate and of the observation time [25]. It is possible to avoid the crystalline phase altogether if the cooling rate is fast enough, ~ 100 K/min [13]. In that case, water can be obtained in *glassy* water or amorphous solid, a solid phase that lacks long range order. The temperature at which the molecular relaxation time reaches 100 s, and the viscosity of the system becomes $\nu = 10^{12}$ Pa$\cdot$ s, is conventionally called *glass transition* T_g. It is important to note that this is not a thermodynamic transition in the standard sense (such as the liquidgas transition), but rather a kinetic event. This implies that different cooling procedures can produce slightly different glass transition temperatures. The temperature at which the glass transition occurs in water is an open question, although a generally accepted value is $T_g = 136$ K at ambient pressure [14, 15, 25]. When glassy water is heated, it crystallizes sponteneously to cubic ice, Ic, at around the crystallization temperature $T_x = 150$ K. Above the glass transition and below the crystallization temperature, water can exist in an extremely viscous liquid state [25]. Water in this small region is defined *ultraviscous*. Therefore, the interval between the homogeneous nucleation temperature and the crystallization temperature is often called *no man's land*, where it is impossible to probe the supercooled liquid state of water with the available experimental techniques. In Fig. 1.3 we show a schematic of the phase diagram at 1 atm representing the stable, metastable and glassy phases of water.

Yet another interesting property of liquid water is that it shows polyamorphism, i.e., the presence of several liquid or glassy states. The concept of polyamorphism is relatively new [58, 62, 169]. The two glassy sates of water that have been extensively studied are the high density and the low density amorphous ice (HDA and LDA respectively). Furthermore, it has been shown that a first-order-like transition exists between LDA and HDA with a discontinuous jump in the density when the coexistence line is crossed [16].

1.3 Liquid-liquid critical point hypothesis

The origin of the anomalies in stable and metastable water is not yet fully understood. As the result, the unclear mechanism of these anomalies attacts a considerable interest in the scientific community [17, 18, 66, 169, 170, 172, 222]. Over the last few decades many experiments and computer simulations have played an important role in establishing the possible explanations for the origin of these anomalies [18, 52, 66, 169, 170, 222]. One of the most popular hypotheses was proposed in 1992 by Poole et. al. [66] based on computer simulations on ST2 water. The proposed hypothesis suggested that the first-order-like transition between LDA and HDA is a low temperature manifestation of the equilibrium phase transition between two distinct phases of liquid water in the deep supercooled region (the no mans land): the low density and the high density liquids (HDL and LDL respectively). This liquid-liquid phase transition (LLPT) terminates by a liquid-liquid critical point (LLCP) located by computer simulations [66] at ≈ 100 MPa and ≈ 220 K, above which the distinction between the two phases disappears. Liquid water near the hypothesized liquid-liquid critical point is a fluctuating mixture of molecules whose local structures resemble LDL and HDL. These enhanced fluctuations are observed as a line of maxima of the thermodynamic response functions, the *Widom line*.

According to the LLCP hypothesis, the apparent divergences of the thermodynamic response functions is a consequence of the increase of the correlation length upon approaching the critical point and divergence at it [10]. Even the anomalous behaviour of water at ambient temperature could be explained by LLCP hypothesis as the long range

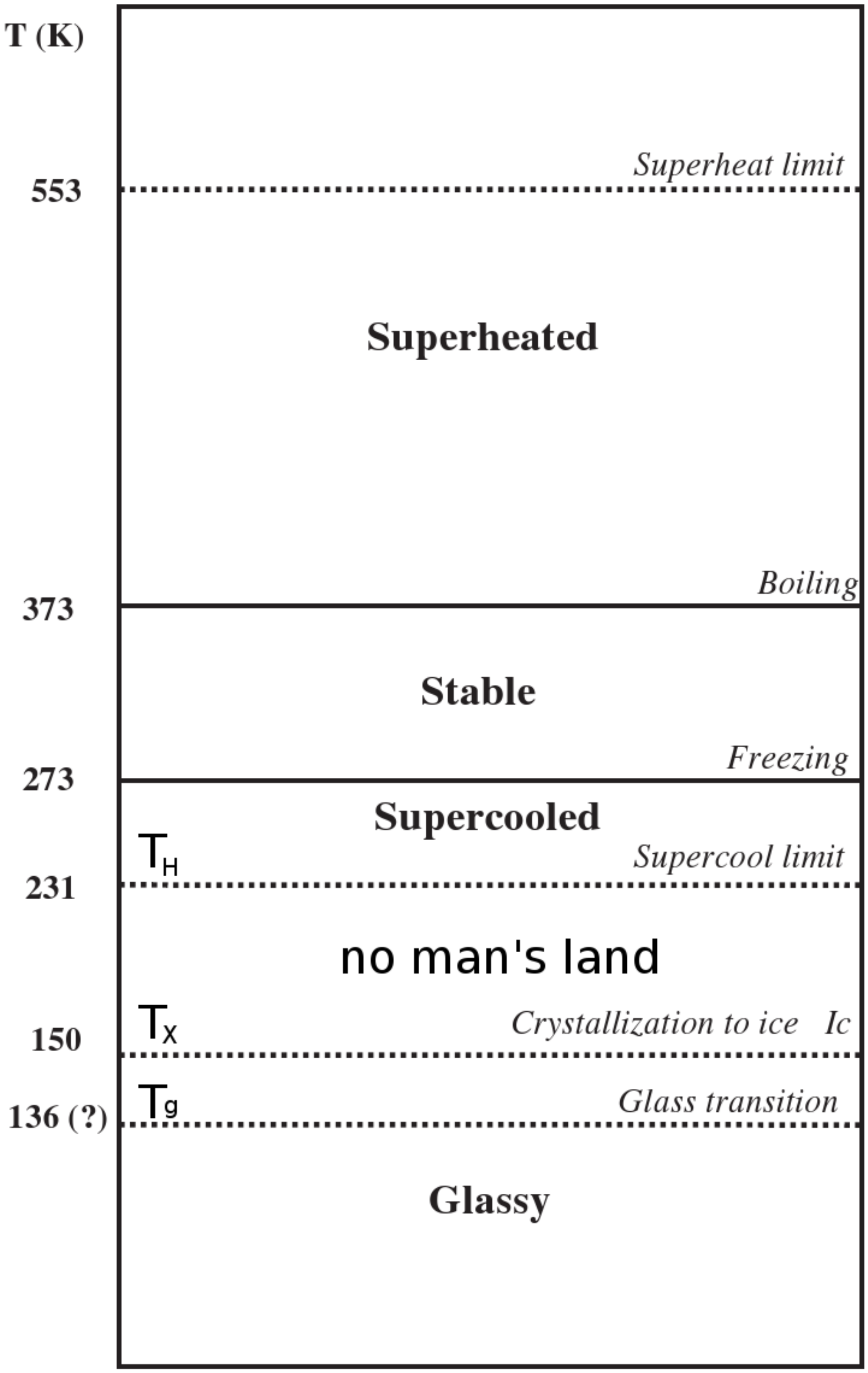

Figure 1.3: Schematic representation of the stable and metastable phases of water at atmospheric pressure. Equilibrium transitions are shown in full lines, kinetic transitions are in dotted lines. Adapted from Ref. [25].

fluctuations induced by the presence of the critical point. Thus, the LLCP is the source of all water anomalies.

The LLCP hypothesis is consistent with all the experimental evidence available to date. However, a direct verification of the LLCP is chalanged by the homogeneous nucleation of the crystal that prevents the access to the no mans land. Fig. 1.4 shows a schematic representation of the phase diagram of water as predicted by the LLCP scenario.

1.4 Nanoconfined water

To this day, the experimental study of supercooled bulk water is hampered by the homogeneous nucleation of the crystal. Therefore, to determine the validity of the liquid-liquid critical point hypothesis, one needs first to solve the technical difficulty of accessing the *no mans land* region.

Recently water confined in nanoscopic structures has attracted interest because nucleation can be delayed. Thus, experimentalists are able to explore the dynamic and thermodynamic behavior of water confined in nano-porous materials, such as vycor pores (a porous hydrophilic silica glass), micellar systems, and layered vermiculite clay [19, 90]. Using nanoconfinement, it is possible to perform NMR and quasi-elastic neutron scattering (QENS) experiments in the deeply supercooled region (280–190 K) [19–23, 90]. Therefore, experiments performed within this interval could be of fundamental interest for understanding the open questions on water.

Confined systems have a tremendous relevance also for current biological advances. In particular, the study of water behavior in the presence of apolar interfaces helps understanding such phenomena as self-assembling of micelles, membrane formations and protein folding [70, 130, 221]. It is also relevant to many important technological and industrial applications such as catalysis and soil chemistry.

However, one needs to be very careful in interpreting experimental and simulations results in confined water. The confinement can exhibit a complex effect on the dynamic and thermodynamic behavior of water. It is the goal of this thesis to examin possible modifications of the supercooled phase diagram of liquid water by the nanoconfinement.

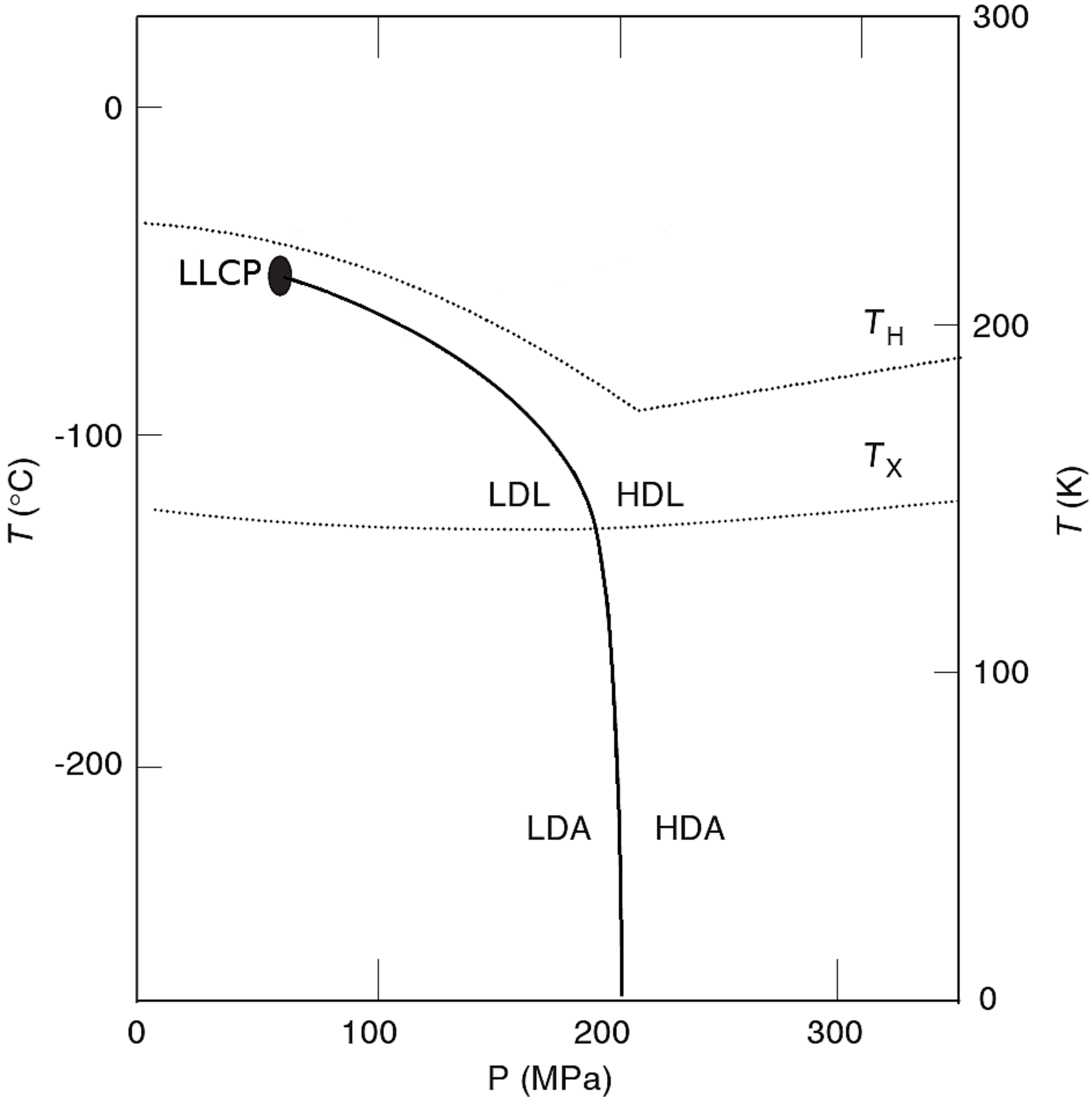

Figure 1.4: Schematic representation of the phases diagram of water on the (P, T) plane predicted by the liquid-liquid critical point hypothesis. The LDA and HDA are separated by a first order phase transition line that extends above the crystalization temperature and separates two liquid phases LDL and HDL. This first order phase transition terminates by a liquid-liquid critical point LLCP, above which the distinction between the two liquids disappears.T_H is the line of the homogeneous nucleation and T_x is the crystalization line. Adapted from Ref. [60].

1.5 Overview of the Dissertation

Coarse-grained model of water

The "liquid-liquid critical point" scenario was first developed by Poole et al. in 1992 [66]. Using molecular dynamics simulations they found a line of first-order transitions between two liquid phases, which ended at a critical point. In 1996, Sastry et al. [68] showed that the thermodynamic anomalies of water are consistent with a phase digram which does not include a singularity, the "singularity-free" scenario.

Experiments have not been able to discriminate among the different theories of liquid water. However, simulations can give insight on the low temperature phase diagram, but suffer from very slow dynamics. There is therefore need of faster simulation methods.

Here we introduce the implementation of a Wolff's cluster algorithm for the Monte Carlo (MC) simulations of a cell model for water [35]. This method, indeed, allows to greatly accelerate the equilibration time of the system, as shown by the direct comparison of its energy autocorrelation time with that of the Metropolis MC dynamics.

Phase Transitions and Dynamics in Bulk and Interficial Water

New experiments for water at the surface of proteins at very low temperature display intriguing dynamic behaviors. The extreme conditions of these experiments make it difficult to explore the wide range of thermodynamic state points needed to offer a suitable interpretation. Detailed simulations suffer the same problem, where equilibration times at low temperature become unreasonably long. We show how Monte Carlo simulations and mean field calculations of a tractable model of water help interpret the experimental results. Here we summarize the results for bulk water and investigate the thermodynamic and dynamic properties of supercooled water at an interface.

Supercooled water in a matrix of hydrophobic nanoparticles

Using Monte Carlo simulations we study a coarse-grained model of a water layer confined in a fixed disordered matrix of hydrophobic nanoparticles at different particle concentrations c. For $c = 0$ we find a first-order liquid-liquid phase transition (LLPT) ending in one critical point at low pressure P. For $c > 0$ our simulations are consistent with a LLPT line ending in two critical points at low and high pressure. For $c = 25\%$ at high P and low temperature, we find a dramatic decrease of compressibility K_T, thermal expansion coefficient α_P, and specific heat C_P. Surprisingly, the effect is present also for c as low as 2.4%. We conclude that even a small presence of hydrophobic nanoparticles can drastically suppress thermodynamic fluctuations, making the detection of the LLPT more difficult.

Hydrophobic nanoconfinement suppresses fluctuations in supercooled water

We perform very efficient Monte Carlo simulations to study the phase diagram of a water monolayer confined in a fixed disordered matrix of hydrophobic nanoparticles between two hydrophobic plates. We consider different hydrophobic nanoparticle concentrations c. We adopt a coarse-grained model of water that for $c = 0$ displays a first order liquid-liquid phase transition (LLPT) line with negative slope in the pressure-temperature $P-T$ plane, ending in a liquid-liquid critical point at about 174 K and 0.13 GPa. We show that upon increase of c the liquid-gas spinodal and the temperature of maximum density line are shifted with respect to $c = 0$ case. We also find dramatic changes in the region around the LLPT. In particular, we observe a substantial (more than 90%) decrease of isothermal compressibility, thermal expansion coefficient and constant-pressure specific heat upon increasing c, consistent with recent experiments. Moreover, we find that a hydrophobic nanoparticle concentration as small as $c = 2.4\%$ is enough to destroy the LLPT for $P \geq 0.16$ GPa. The fluctuations of volume apparently diverge at $P \approx 0.16$ GPa suggesting that the LLPT line ends in a LL critical point at 0.16 GPa. Therefore, nanoconfinement reduces the range of $P-T$ where the LLPT is observable. By increasing the hydrophobic nanoparticle concentration c, the LLPT becomes weaker and its $P-T$ range smaller. The model allows us to explain these phenomena in terms of proliferation of interfaces among domains with different local order, promoted by the hydrophobic effect of the water-hydrophobic nanoparticle interfaces.

Effect of hydrophobic environments on the hypothesized liquid-liquid critical point of water

The complex behavior of liquid water, along with its anomalies and their crucial role in the existence of life, continue to attract the attention of researchers. The anomalous behavior of water is more pronounced at subfreezing temperatures and numerous theoretical and experimental studies are directed towards developing a coherent thermodynamic and dynamic framework for understanding supercooled water. The existence of a liquid–liquid critical point in the deep supercooled region has been related to the anomalous behavior of water. However, the experimental study of supercooled water at very low temperatures is hampered by the homogeneous nucleation of crystals. Recently, water confined in nanoscopic structures or in solutions has attracted interest because nucleation can be delayed. These systems have a tremendous relevance also for current biological advances; for example, supercooled water is often confined in cell membranes and acts as a solvent for biological molecules. In particular, considerable attention has been recently devoted to understanding hydrophobic interactions or the behavior of water in the presence of apolar interfaces due to their fundamental role in self-assembly of micelles, membrane formation and protein folding. This article reviews and compares two very recent computational works aimed at elucidating the changes in the thermodynamic behavior in the supercooled region and the liquid–liquid critical point phenomenon for water in contact with hydrophobic environments. The results are also compared to previous reports for water in hydrophobic environments.

Nanoparticle Confinement in Anomalous Liquids

We investigate using molecular dynamics the effect of the structure of nanoconfinement for liquids with water-like anomalies and liquid-liquid phase transition (LLPT). We find that if the confinement is in an ordered matrix of nanoparticles (NPs) the anomalies are preserved, although the LLPT shifts to lower temperatures, higher pressures and higher densities with respect to bulk. On the contrary, if the NPs matrix is disordered, we find a drastically different phase diagram: the LLPT occurs only in a reduced interval of densities and the anomalies are washed out. To understand this effect we calculate the changes in the system at the microscopic level. In all the different confinements considered here we observe a dramatic increase of density of liquid near the confining NPs. In the disordered case the confinement induces larger heterogeneity in the local density, responsible for the weakening of the LLPT and the disappearance of anomalies.

Part II

Simulations of confined water

Chapter 2

Coarse-grained model of water

Water is possibly the most important liquid for life [24] and, at the same time, is a very peculiar liquid [25]. In the stable liquid regime its thermodynamic response functions behave qualitatively differently than a typical liquid. The isothermal compressibility K_T, for example, has a minimum as a function of temperature at $T = 46$ °C, while for a typical liquid K_T monotonically decreases upon cooling. Water's anomalies become even more pronounced as the system is cooled below the melting point and enters the metastable supercooled regime [26].

Different hypothesis have been proposed to rationalize the anomalies of water [27]. All these interpretations, but one, predict the existence of a liquid–liquid phase transition in the supercooled state, consistent with the experiments to date [27] and supported by different models [25].

To discriminate among the different interpretations, many experiments have been performed [28]. However, the freezing in the temperature-range of interest can be avoided only for water in confined geometries or on the surface of macromolecules [27, 29]. Since experiments in the supercooled region are difficult to perform, numerical simulations have played an important role in recent years to help interpret the data. However, also the simulations at very low temperature T are hampered by the glassy dynamics of the empirical models of water [30–32]. For these reasons is important to implement more efficient numerical simulations for simple models, able to capture the fundamental physics of water but also less computationally expensive. Here we introduce the implementation of a Wolff's cluster algorithm [33] for the Monte Carlo (MC) simulations of a cell model for water [34, 35]. The model is able to reproduce all the different scenarios proposed to interpret the behavior of water [36] and has been analyzed (i) with mean field (MF) [34, 35, 37, 38], (ii) with Metropolis MC simulations [32, 39] and (iii) with Wang-Landau MC density of state algorithm [40]. Recent Metropolis MC simulations [32] have shown that very large times are needed to equilibrate the system as $T \to 0$, as a consequence of the onset of the glassy dynamics. The implementation of the Wolff's clusters MC dynamics, presented here, allows us to (i) drastically reduce the equilibration times of the model at very low T and (ii) give a geometrical characterization of the regions of correlated water molecules (clusters) at low T and show that the liquid–liquid phase transition can be interpreted as a percolation transition of the tetrahedrally ordered clusters.

2.1 The model

The system consists of N particles distributed within a volume V in d dimensions. The volume is divided into N cells of volume v_i with $i \in [1, N]$. For sake of simplicity, these cells are chosen of the same size, $v_i = V/N$, but the generalization to the case in which the volume can change without changes in the topology of the nearest–neighbor (n.n.) is straightforward. By definition, $v_i \geq v_0$, where v_0 is the molecule hard-core volume. Each cell has a variable $n_i = 0$ for a gas-like or $n_i = 1$ for a liquid-like cell. We partition the total volume in a way such that each cell has at least four n.n. cells, e.g. as in a cubic lattice in $3d$ or a square lattice in $2d$. Periodic boundary conditions are used to limit finite–size effects.

The system is described by the Hamiltonian [34, 35]

$$\mathscr{H} = -\epsilon \sum_{\langle i,j \rangle} n_i n_j - J \sum_{\langle ij \rangle} n_i n_j \delta_{\sigma_{ij},\sigma_{ji}} - J_\sigma \sum_i n_i \sum_{(k,l)_i} \delta_{\sigma_{ik},\sigma_{il}}, \tag{2.1}$$

where $\epsilon > 0$ is the strength of the van der Waals attraction, $J > 0$ accounts for the hydrogen bond energy, with four (Potts) variables $\sigma_{ij} = 1, \ldots, q$ representing bond indices of molecule i with respect to the four n.n. molecules j, $\delta_{a,b} = 1$ if $a = b$ and $\delta_{a,b} = 0$ otherwise,

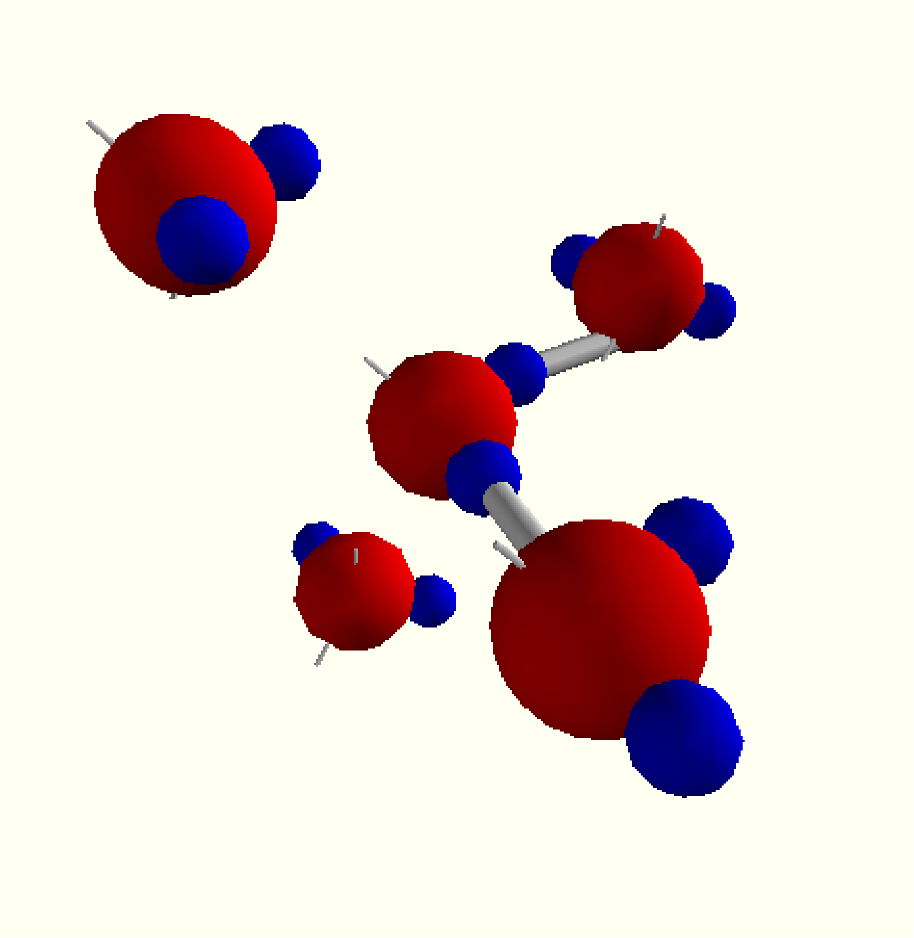

Figure 2.1: Pictorial representation of five water molecules in $3d$. Two hydrogen bonds (grey links) connect the hydrogens (in blue) of the central molecule with the lone electrons (small gray lines) of two nearest neighbor (n.n.) molecules. A bond index (arm) with $q = 6$ possible values is associated to each hydrogen and lone electron, giving rise to q^4 possible orientational states for each molecule. A hydrogen bond can be formed only if the two facing arms of the n.n. molecules are in the same state. Arms on the same molecule interact among themselves to mimic the O-O-O interaction that drives the molecules toward a tetrahedral local structure.

and $\langle i, j \rangle$ denotes that i and j are n.n. The model does not assume a privileged state for bond formation. Any time two facing bond indices (arms) are in the same (Potts) state, a bond is formed. The third term represents an intramolecular (IM) interaction accounting for the O–O–O correlation [41, 42], locally driving the molecules toward a tetrahedral configuration. When the bond indices of a molecule are in the same state, the energy is decreased by an amount $J_\sigma \geqslant 0$ and we associate this local ordered configuration to a local tetrahedral arrangement. The notation $(k, l)_i$ indicates one of the six different pairs of the four bond indices of molecule i (Fig.2.1). The model does not differentiate "donor" molecule and "acceptor" molecule in the hydrogen bond definition. This simplification increases the number of possible bonded configurations, hence increases the entropy associated to the local tetrahedral configurations. A simple modification of the model could explicitly take into account this feature, however the comparison of the results from the present version of the model with experiments and simulations from more detailed models shows good qualitative agreement.

Experiments show that the formation of a hydrogen bond leads to a local volume expansion [25]. Thus in our system the total volume is

$$V = N v_0 + N_{HB} v_{HB}, \tag{2.2}$$

where

$$N_{HB} \equiv \sum_{<i,j>} n_i n_j \delta_{\sigma_{ij},\sigma_{ji}} \tag{2.3}$$

is the total number of hydrogen bonds, and v_{HB} is the constant specific volume increase due to the hydrogen bond formation.

2.2 Mean–field analysis

In the mean–field (MF) analysis the macrostate of the system in equilibrium at constant pressure P and temperature T (NPT ensemble) may be determined by a minimization of the Gibbs free energy per molecule, $g \equiv (\langle \mathscr{H} \rangle + PV - TS)/N_w$, where

$$N_w = \sum_i n_i \tag{2.4}$$

is the total number of liquid-like cells, and $S = S_n + S_\sigma$ is the sum of the entropy S_n over the variables n_i and the entropy S_σ over the variables σ_{ij}.

A MF approach consists of writing g explicitly using the approximations

$$\sum_{<ij>} n_i n_j \longrightarrow 2Nn^2 \tag{2.5}$$

$$\sum_{<ij>} n_i n_j \delta_{\sigma_{ij},\sigma_{ji}} \longrightarrow 2Nn^2 p_\sigma \tag{2.6}$$

$$\sum_i n_i \sum_{(k,l)_i} \delta_{\sigma_{ik},\sigma_{il}} \longrightarrow 6Nnp_\sigma \tag{2.7}$$

where $n = N_w/N$ is the average of n_i, and p_σ is the probability that two adjacent bond indices σ_{ij} are in the appropriate state to form a hydrogen bond.

Therefore, in this approximation we can write

$$V = Nv_0 + 2Nn^2 p_\sigma v_{HB}, \tag{2.8}$$

$$\langle \mathscr{H} \rangle = -2\left[\epsilon n + \left(Jn + 3J_\sigma\right) p_\sigma\right] nN. \tag{2.9}$$

The probability p_σ, properly defined as the thermodynamic average over the whole system, is approximated as the average over two neighboring molecules, under the effect of the mean-field h of the surrounding molecules

$$p_\sigma = \left\langle \delta_{\sigma_{ij},\sigma_{ji}} \right\rangle_h . \tag{2.10}$$

The ground state of the system consists of all N variables $n_i = 1$, and all σ_{ij} in the same state. At low temperatures, the symmetry will remain broken, with the majority of the σ_{ij} in the preferred state. We associate this preferred state to the tetrahedral order of the molecules and define m_σ as the density of the bond indices in the tetrahedral state, with $0 \leq m_\sigma \leq 1$. Therefore, the number density n_σ of bond indices σ_{ij} is in the tetrahedral state is

$$n_\sigma = \frac{1 + (q-1)m_\sigma}{q}. \tag{2.11}$$

Since an appropriate form for h is [34, 35]

$$h = 3J_\sigma n_\sigma, \tag{2.12}$$

we obtain that $\frac{3J_\sigma}{q} \leq h \leq 3J_\sigma$.

The MF expressions for the entropies S_n of the N variables n_i, and S_σ of the $4Nn$ variables σ_{ij}, are then [37]

$$S_n = -k_B N(n\log(n) + (1-n)\log(1-n)) \tag{2.13}$$

$$S_\sigma = -k_B 4Nn[n_\sigma \log(n_\sigma) + (1-n_\sigma)\log(1-n_\sigma) + \log(q-1)], \tag{2.14}$$

where k_B is the Boltzmann constant.

Equating

$$p_\sigma \equiv n_\sigma^2 + \frac{(1-n_\sigma)^2}{q-1}, \tag{2.15}$$

with the approximate expression in Eq. (2.10), allows for solution of n_σ, and hence g, in terms of the order parameter m_σ and n.

By minimizing numerically the MF expression of g with respect to n and m_σ, we find the equilibrium values $n^{(eq)}$ and $m_\sigma^{(eq)}$ and, with Eqs. (2.4) and (3.5), we calculate the density ρ at any (T, P) and the full equation of state. An example of minimization of g is presented in Fig. 2.2 where, for the model's parameters $J/\epsilon = 0.5$, $J_\sigma/\epsilon = 0.05$, $v_{HB}/v_0 = 0.5$, $q = 6$, a discontinuity in $m_\sigma^{(eq)}$ is observed for $Pv_0/\epsilon > 0.8$. As discussed in Ref.s [34, 35, 39] this discontinuity corresponds to a first order phase transition between two liquid phases with different degree of tetrahedral order and, as a consequence, different density. The higher P at which the change in $m_\sigma^{(eq)}$ is continuous, corresponds to the pressure of a liquid–liquid critical point (LLCP). The occurrence of the LLCP is consistent with one of the possible interpretations of the anomalies of water, as discussed in Ref. [37]. However, for different choices of parameters, the model reproduces also the other proposed scenarios [36].

2.3 The simulation with the Wolff's clusters Monte Carlo algorithm

To perform MC simulations in the NPT ensemble, we consider a modified version of the model in which we allow for continuous volume fluctuations. To this goal, (i) we assume that the system is homogeneous with all the variables n_i set to 1 and all the cells

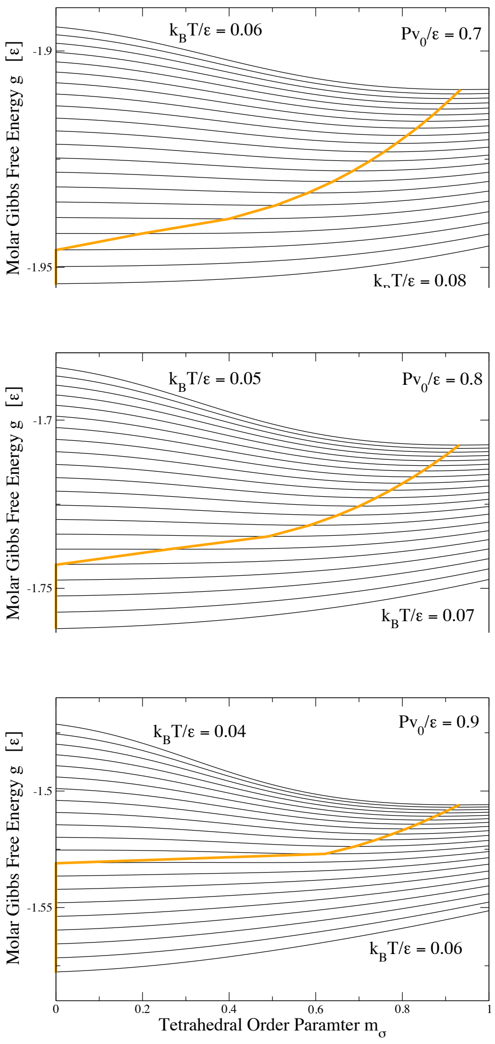

Figure 2.2: Numerical minimization of the molar Gibbs free energy g in the MF approach. The model's parameters are $J/\epsilon = 0.5$, $J_\sigma/\epsilon = 0.05$, $v_{HB}/v_0 = 0.5$ and $q = 6$. In each panel we present g (dashed lines) calculated at constant P and different values of T. The thick line crossing the dashed lines connects the minima $m_\sigma^{(eq)}$ of g at different T. Upper panel: $Pv_0/\epsilon = 0.7$, for T going from $k_BT/\epsilon = 0.06$ (top) to 0.08 (bottom). Middle panel: $Pv_0/\epsilon = 0.8$, for T going from $k_BT/\epsilon = 0.05$ (top) to 0.07 (bottom). Lower panel: $Pv_0/\epsilon = 0.9$, for T going from $k_BT/\epsilon = 0.04$ (top) to 0.06 (bottom). In each panel dashed lines are separated by $k_B\delta T/\epsilon = 0.001$. In all the panels $m_\sigma^{(eq)}$ increases when T decreases, being 0 (marking the absence of tetrahedral order) at the higher temperatures and $\simeq 0.9$ (high tetrahedral order) at the lowest temperature. By changing T, $m_\sigma^{(eq)}$ changes in a continuous way for $Pv_0/\epsilon = 0.7$ and 0.8, but discontinuous for $Pv_0/\epsilon = 0.9$ and higher P.

with volume $v = V/N$; (ii) we consider that $V \equiv V_{MC} + N_{HB}v_{HB}$, where $V_{MC} \geqslant Nv_0$ is a dynamical variable allowed to fluctuate in the simulations; (iii) we replace the first (van der Waals) term of the Hamiltonian in Eq. (2.1) with a Lennard-Jones potential with attractive energy $\epsilon > J$ and truncated at the hard-core distance

$$U_W(r) \equiv \begin{cases} \infty & \text{if } r \leqslant r_0, \\ \epsilon \left[\left(\frac{r_0}{r}\right)^{12} - \left(\frac{r_0}{r}\right)^{6} \right] & \text{if } r > r_0. \end{cases} \tag{2.16}$$

where $r_0 \equiv (v_0)^{1/d}$; the distance between two n.n. molecules is $(V/N)^{1/d}$, and the distance r between two generic molecules is the Cartesian distance between the center of the cells in which they are included.

The simplification (i) could be removed, by allowing the cells to assume different volumes v_i and keeping fixed the number of possible n.n. cells. However, the results of the model under the simplification (i) compares well with experiments [37]. Furthermore, the simplification (i) allows to drastically reduce the computational cost of the evaluation of the $U_W(r)$ term from $N(N-1)$ to $N-1$ operations. The changes (i)–(iii) modify the model used for the mean field analysis and allow off-lattice MC simulations for a cell model in which the topology of the molecules (i.e. the number of n.n.) is preserved. The comparison of the mean field results with the MC simulations show that these changes do not modify the physics of the system.

We perform MC simulations with $N = 2500$ and $N = 10000$ molecules, each with four n.n. molecules, at constant P and T, in 2d, and with the same parameters used for the mean field analysis. To each molecules we associate a cell on a square lattice.

The Wolff's algorithm is based on the definition of a cluster of variables chosen in such a way to be thermodynamically correlated [43–45]. To define the Wolff's cluster, a bond index (arm) of a molecule is randomly selected; this is the initial element of a stack. The cluster is grown by first checking the remaining arms of the same initial molecule: if they are in the same Potts state, then they are added to the stack with probability $p_{\text{same}} \equiv \min[1, 1 - \exp(-\beta J_\sigma)]$ [33], where $\beta \equiv (k_B T)^{-1}$. This choice for the probability p_{same} depends on the interaction J_σ between two arms on the same molecule and guarantees that the connected arms are thermodynamically correlated [45]. Next, the arm of a new molecule, facing the initially chosen arm, is considered. To guarantee that connected facing arms correspond to thermodynamically correlated variables, is necessary [43, 44] to link them with the probability $p_{\text{facing}} \equiv \min[1, 1 - \exp(-\beta J')]$ where $J' \equiv J - Pv_{HB}$ is the P–dependent effective coupling between two facing arms as results from the enthalpy $\mathscr{H} + PV$ of the system. It is important to note that J' can be positive or negative depending on P. If $J' > 0$ and the two facing arms are in the same state, then the new arm is added to the stack with probability p_{facing}; if $J' < 0$ and the two facing arms are in different states, then the new arm is added with probability p_{facing} [1]. Only after every possible direction of growth for the cluster has been considered the values of the arms are changed in a stochastic way; again we need to consider two cases: (i) if $J' > 0$, all arms are set to the same new value

$$\sigma^{\text{new}} = \left(\sigma^{\text{old}} + \phi\right) \mod q \tag{2.17}$$

where ϕ is a random integer between 1 and q; (ii) if $J' < 0$, the state of every single arm is changed (rotated) by the same random constant $\phi \in [1, \ldots q]$

$$\sigma_i^{\text{new}} = \left(\sigma_i^{\text{old}} + \phi\right) \mod q. \tag{2.18}$$

In order to implement a constant P ensemble we let the volume fluctuate. A small increment $\Delta r/r_0 = 0.01$ is chosen with uniform random probability and added to the current radius of a cell. The change in volume $\Delta V \equiv V^{\text{new}} - V^{\text{old}}$ and van der Waals energy ΔE_W is computed and the move is accepted with probability $\min\left(1, \exp\left[-\beta\left(\Delta E_W + P\Delta V - T\Delta S\right)\right]\right)$, where $\Delta S \equiv -Nk_B \ln(V^{new}/V^{old})$ is the entropic contribution.

2.4 Monte Carlo correlation times

The cluster MC algorithm described in the previous section turns out to be very efficient at low T, allowing to study the thermodynamics of deeply supercooled water with quite intriguing results [46]. To estimate the efficiency of the cluster MC dynamics with respect

---

[1] The results of [43–45] guarantee that the cluster algorithm described here satisfies the detailed balance and is ergodic. Therefore, it is a valid Monte Carlo dynamics.

to the standard Metropolis MC dynamics, we evaluate in both dynamics, and compare, the autocorrelation function of the average magnetization per site $M_i \equiv \frac{1}{4}\sum_j \sigma_{ij}$, where the sum is over the four bonding arms of molecule i.

$$C_M(t) \equiv \frac{1}{N}\sum_i \frac{\langle M_i(t_0+t)M_i(t_0)\rangle - \langle M_i\rangle^2}{\langle M_i^2\rangle - \langle M_i\rangle^2}. \tag{2.19}$$

For sake of simplicity, we define the MC dynamics autocorrelation time τ as the time, measured in MC steps, when $C_M(\tau) = 1/e$. Here we define a MC step as $4N$ updates of the bond indices followed by a volume update, i.e. as $4N+1$ steps of the algorithm.

In Fig. 2.3 we show a comparison of $C_M(t)$ for the Metropolis and Wolff algorithm implementations of this model for a system with $N = 50 \times 50$, at three temperatures along an isobar below the LLCP, and approaching the line of the maximum, but finite, correlation length, also known as Widom line $T_W(P)$ [37]. In the top panel, at $T \gg T_W(P)$ ($k_BT/\epsilon = 0.11$, $Pv_0/\epsilon = 0.6$), we find a correlation time for the Wolff's cluster MC dynamics $\tau_\mathrm{W} \approx 3 \times 10^3$, and for the Metropolis dynamics $\tau_\mathrm{M} \approx 10^6$. In the middle panel, at $T > T_W(P)$ ($k_BT/\epsilon = 0.09$, $Pv_0/\epsilon = 0.6$) the difference between the two correlation times is larger: $\tau_\mathrm{W} \approx 2.5 \times 10^3$, $\tau_\mathrm{M} \approx 3 \times 10^6$. The bottom panel, at $T \simeq T_W(P)$ ($k_BT/\epsilon = 0.06$, $Pv_0/\epsilon = 0.6$) shows $\tau_\mathrm{W} \approx 3.7 \times 10^2$, while τ_M is beyond the accessible time window ($\tau_\mathrm{M} > 10^7$).

Since as $T \to 0$ the system enters a glassy state [32], the efficiency $\tau_\mathrm{M}/\tau_\mathrm{W}$ grows at lower T allowing the evaluation of thermodynamics averages even at $T \ll T_C$ [46]. In particular, the cluster MC algorithm turns out to be very efficient when approaching the Widom line in the vicinity of the LLCP, with an efficiency of the order of 10^4. We plan to analyze in a systematic way how the efficiency $\tau_\mathrm{M}/\tau_\mathrm{W}$ grows on approaching the LLCP. This result is well known for the standard liquid-gas critical point [33] and, on the basis of our results, could be extended also to the LLCP. However, this analysis is very expensive in terms of CPU time and goes beyond the goal of the present work. Nevertheless, the percolation analysis, presented in the next section, helps in understanding the physical reason for this large efficiency.

The efficiency is a consequence of the fact that the average size of Wolff's clusters changes with T and P in the same way as the average size of the regions of correlated

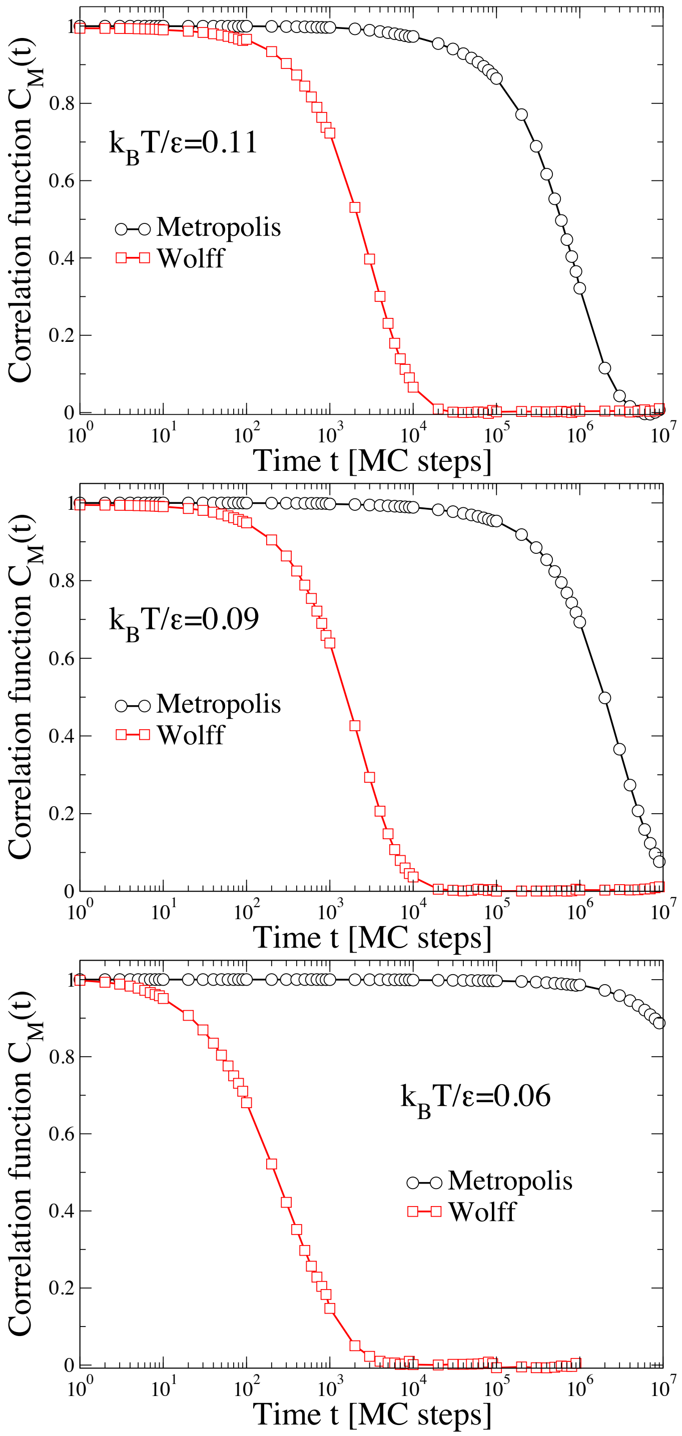

Figure 2.3: Comparison of the autocorrelation function $C_M(t)$ for the Metropolis (circles) and Wolff (squares) implementation of the present model. We show the temperatures $k_BT/\epsilon = 0.11$ (top panel), $k_BT/\epsilon = 0.09$ (middle panel), $k_BT/\epsilon = 0.06$ (bottom panel), along the isobar $Pv_0/\epsilon = 0.6$ close to the LLCP for $N = 50 \times 50$.

molecules [45], i.e. a Wolff's cluster statistically represents a region of correlated molecules. Moreover, the mean cluster size diverges at the critical point with the same exponent of the Potts magnetic susceptibility [45], and the clusters percolate at the critical point, as we will discuss in the next section.

2.5 Percolating clusters of correlated molecules

The efficiency of the Wolff's cluster algorithm is a consequence of the exact relation between the average size of the finite clusters and the average size of the regions of thermodynamically correlated molecules. The proof of this relation at any T derives straightforward from the proof for the case of Potts variables [45]. This relation allows to identify the clusters built during the MC dynamics with the correlated regions and emphasizes (i) the appearance of heterogeneities in the structural correlations [47–49], and (ii) the onset of percolation of the clusters of tetrahedrally ordered molecules at the LLCP [50], as shown in Fig. 2.4.

A systematic percolation analysis [43, 44] is beyond the goal of this report, however configurations such as those in Fig. 2.4 allow the following qualitative considerations. At $T > T_C$ the average cluster size is much smaller than the system size. Hence, the structural correlations among the molecules extends only to short distances. This suggests that the correlation time of a local dynamics, such as Metropolis MC or molecular dynamics, would be short on average at this temperature and pressure. Nevertheless, the system appears strongly heterogeneous with the coexistence of large and small clusters, suggesting that the distribution of correlation times evaluated among molecules at a given distance could be strongly heterogeneous. The clusters appear mostly compact but with a fractal surface, suggesting that borders between clusters can rapidly change.

At $T \simeq T_C$ there is one large cluster, in red on the right of the middle panel of Fig. 2.4, with a linear size comparable to the system linear extension and spanning in the vertical direction. The appearance of spanning clusters shows the onset of the percolation geometrical transition. At this state point the correlation time of local, such as Metropolis MC dynamics or molecular dynamics would be very slow as a consequence of the large

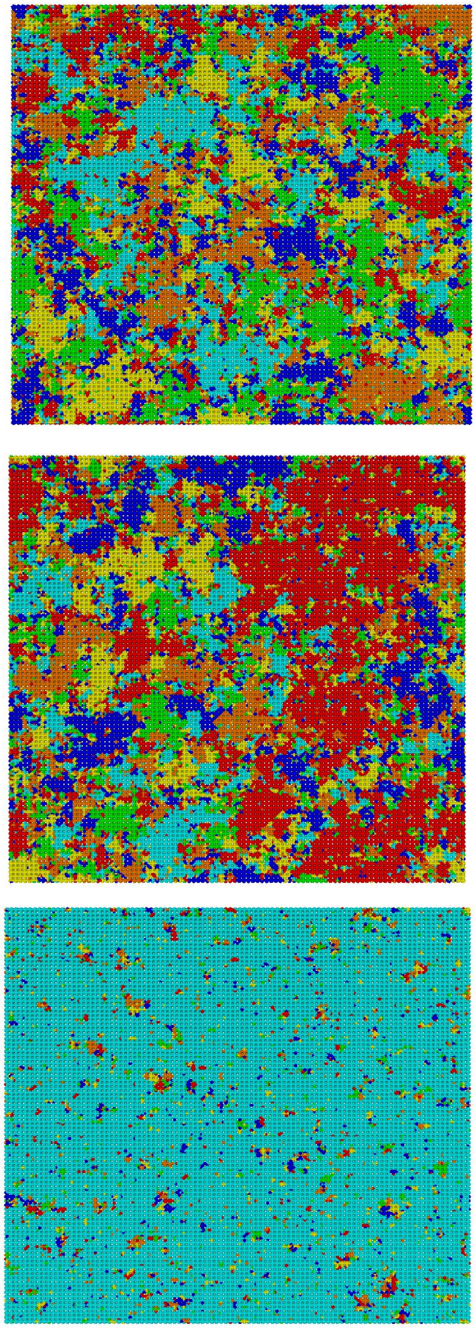

Figure 2.4: Three snapshots of the system with $N = 100 \times 100$, showing Wolff clusters of correlated water molecules. For each molecule we show the states of the four arms and associate different colors to different arm's states. The state points are at pressure close to the critical value P_C ($Pv_0/\epsilon = 0.72 \simeq P_C v_0/\epsilon$) and $T > T_C$ (top panel, $k_B T/\epsilon = 0.0530$), $T \simeq T_C$ (middle panel, $k_B T/\epsilon = 0.0528$), $T < T_C$ (bottom panel, $k_B T/\epsilon = 0.0520$), showing the onset of the percolation at $T \simeq T_C$.

extension of the structurally correlated region. On the other hand, the correlation time of the Wolff's cluster dynamics is short because it changes in one single MC step the state of all the molecules in clusters, some of them with very large size. Once the spanning cluster is formed, it breaks the symmetry of the system and a strong effective field acts on the molecules near its border to induce their reorientation toward a tetrahedral configuration with respect the molecules in the spanning cluster.

As shown in Fig.3, the spanning cluster appears as a fractal object, with holes of any size. The same large distribution of sizes characterizes also the finite clusters in the system. The absence of a characteristic size for the clusters (or the holes of the spanning cluster) is the consequence of the fluctuations at any length-scale, typical of a critical point.

At $T < T_C$ the majority of the molecules belongs to a single percolating cluster that represents the network of tetrahedrally ordered molecules. All the other clusters are small, with a finite size that corresponds to the regions of correlated molecules. The presence of many small clusters gives a qualitative idea of the heterogeneity of the dynamics at these temperatures.

2.6 Summary and conclusions

We describe the numerical solution of mean field equations and the implementation of the Wolff's cluster MC algorithm for a cell model for liquid water. The mean field approach allows us to estimate in an approximate way the phase diagram of the model at any state point predicting intriguing new results at very low T [46].

To explore the state points of interest for these predictions the use of standard simulations, such as molecular dynamics or Metropolis MC, is not effective due to the onset of the glassy dynamics [32]. To overcome this problem and access the deeply supercooled region of liquid water, we adopt the Wolff's cluster MC algorithm. This method, indeed, allows to greatly accelerate the autocorrelation time of the system. Direct comparison of Wolff's dynamics with Metropolis dynamics in the vicinity of the liquid-liquid critical point shows a reduction of the autocorrelation time of a factor at least 10^4.

Furthermore, the analysis of the clusters generated during the Wolff's MC dynamics allows to emphasize how the regions of tetrahedrally ordered molecules build up on approaching the liquid–liquid critical point, giving rise to the backbone of the tetrahedral hydrogen bond network at the phase transition [50]. The coexistence of clusters of correlated molecules with sizes that change with the state point gives a rationale for the heterogeneous dynamics observed in supercooled water [47–49].

Chapter 3

Phase Transitions and Dynamics in Bulk and Interficial Water

Water is essential in biology, because it participates in nearly every process necessary for life (including cell metabolism, transport of nutrients and residues, protein conformation changes, etc.), and is the most common solvent in chemistry. It regulates a large variety of processes, including atmospheric phenomena, the formation of geophysical structures, the propagation of cracks in stones and cement, the sliding of glaciers, the transport in plants, and is ubiquitous in the universe as ice in the interstellar space. In all these examples the properties of water are essential to understand what is observed.

Nevertheless, water has proven to be a complex puzzle to many researchers for its anomalous thermodynamic and dynamic properties at room temperature and pressure. For example, by decreasing temperature T at pressure $P = 1$ atm, water's volume fluctuations, proportional to the isothermal compressibility K_T, increase below $T = 46^o$C, and entropy fluctuations, proportional to the isobaric specific heat C_P increase below $T = 35^o$C, while in normal liquid any fluctuation decreases when T is decreased [26, 51, 52]. These water's anomalies grow upon cooling and increase in number. For example below $T = 4^o$C the cross-fluctuation of volume and entropy, proportional to the isobaric thermal expansion coefficient α_P, becomes negative [53], while it is always positive in normal liquids where the entropy decreases when the volume decreases [37].

By decreasing T even more, it is experimentally possible to supercool liquid water down to $T_H = -41^o$C at 1 atm and to $T_H = -92^o$C at 2000 atm, where the liquid is metastable with respect to crystal phases [26]. These extreme conditions are not unusual in nature, where water exists in its liquid form at -20^oC in insects, -37^oC in clouds or -47^oC in plants [54]. Below T_H the homogeneous nucleation of crystal ice occurs in a time too short to allow any measurements. But even the crystal phase of water is not simple. In fact, water is a polymorph with at least sixteen forms of crystal ices, the last one, Ice XV, was discovered in 2009 [55].

However, at very low T, crystal water is not the only possible kind of ice. By rapidly quenching liquid water below -123^oC [56], or by condensing the vapour at low T [57], or by compressing crystal ice at low T [58], or by irradiation (with ions for example [59]), it is possible to solidify water as an amorphous, or glass, i. e. a form that has the elastic properties of a solid, but the structure of a liquid with no long-range order [60]. As for the crystal state, the amorphous state of water is also not unique. Water is a polyamorph with at least three different amorphous states: low–density amorphous (LDA), discovered in 1935 [61], high–density amorphous (HDA), discovered in 1984 [62], and very high-density amorphous ice (VHDA), discovered in 2001 [63].

All these anomalies of water are a consequence of the properties of the hydrogen bond network that they form. The hydrogen bond interaction is characterized by a preferred geometrical configuration, that at low T and P is approximately a tetrahedron of four molecules around a central one, with an angle varying around 106.6^o (slightly smaller than a tetrahedral angle of 109.47^o) and a distance oscillating around 2.82 Å[37]. The local arrangement, including the number of nearest neighbours, can change with T and P. In particular, in 2000 Soper and Ricci observed at 268 K, compressing from 26 to 400 MPa, a continuous transformation from low–density liquid (LDL) local arrangement of water with an open, hydrogen-bonded tetrahedral structure, to high–density liquid (HDL) local arrangement with nontetrahedral O-O-O angles and a collapsed second coordination shell with broken hydrogen bonds, and a change in density of about 73% [64].

3.0.1 Thermodynamic Interpretations of Water Behavior

All the above results are consistent with theories that propose different mechanisms and different phase behaviors in the supercooled region. They can be summarized in four possible scenarios for the $P-T$ phase diagram.

(i) In the *stability limit* (SL) scenario [65] the behavior of the superheated liquid spinodal, i. e. the limit of stability of the liquid with respect to the gas, and the stretched water, i. e. water under tension as in a plant fibers, are related. In particular, it is hypothesized that the limits of stability of these two regions are continuously connected at negative pressure, forming a re-entrant curve toward the positive P region below $T_H(P)$. The response functions, including K_T, C_P and α_P, diverge when T is decreased a positive P as a consequence of the approaching of the re-entrant spinodal line.

(ii) In the *liquid–liquid critical point* (LLCP) scenario [66] it is hypothesized the existence of a LDL–HDL first–order phase transition line with negative slope in the $P-T$ plane and terminating in a critical point C'. Below the critical pressure $P_{C'}$ the response functions increase on approaching the Widom line (the locus of correlation length maxima emanating from C' into the one–phase region) [37], and for $P > P_{C'}$ by approaching the HDL–to–LDL spinodal line. The possibility with $P_{C'} < 0$ have also been proposed [67].

(iii) In the *singularity–free* (SF) scenario [68] it is hypothesized that the low-T anticorrelation between volume and entropy gives rise to response functions that increase upon cooling and display maxima at non–zero T, but do not display any singular behavior. Specifically, Sastry et al. [68] show that this is a direct consequence of the fact that water's line of temperatures of maximum density (TMD) has a negative slope in the (T, P) plane.

(iv) In the *critical–point free* (CPF) scenario [28] it is hypothesized that a first–order phase transition line separates two liquid phases and extends to $P < 0$ toward the superheated limit of stability of liquid water. This scenario effectively predicts a continuous locus of stability limit spanning the superheated, stretched and supercooled state, because the spinodal associated with the first–order transition will intersect the liquid–gas spinodal at negative pressure. No critical point is present in this scenario.

Since all these scenarios are consistent with the available experimental data, a natural question is if we can design an experiment that would discriminate among them. Unfortunately, many scientists have discovered that an answer to this question is a difficult challenge [28]. In fact, experiments on bulk water are hampered by freezing below T_H, and no measurements on bulk liquid water can be performed with our present technology below this temperature. Nevertheless, the different proposed theories have different implications on phenomena such as the cold denaturation (and stop of activity) of proteins at low T, an important issue in cryopreservation, cryonics, cryostasis and cryobiology.

3.0.2 Interfacial Water

One possible strategy to probe supercooled water at very low T is to consider water at an interface. Water adsorbed onto the surface of proteins or confined in nanopores freezes at much lower T than bulk water, giving access to a low-temperature region where interfacial water is still liquid, while bulk water would not be [69]. In many cases of interest for practical purposes in biology, geology or industrial applications, water is hydrating a surface or is confined. As a consequence, fundamental research in physics and chemistry has been performed in recent years with experiments [28, 41, 69–76], theories and simulations [77–80].

During the last years experiments on water in Vycor micropores [81], in nanopores of MCM-41 silica [82–84], of sol–gel silica glass [85], of NaA zeolites [86], or of double-wall carbon nanotubes [87] have contributed to the investigation of water dynamics in confinement. In particular, confinement in hydrophilic MCM-41 silica nanopores of 1.8 and 1.4 nm diameter allows to study water dynamics down to 200 K where quasielastic neutron scattering reveals a crossover at $T \approx 225$ K in the average translational relaxation time from a non-Arrhenius behavior at high T to an Arrhenius behavior at low T [88]. A similar crossover is also observed for the self-diffusion coefficient of water by nuclear magnetic resonance at $T \approx 223$ K [89]. By increasing from 400 bars to 1600 bars the external pressure applied on a sample of MCM-41 silica nanopores with 1.4 nm diameter at full hydration level of 0.5 g of H_2O per g of silica, it has been observed that the crossover occurs at lower T, reaching $T \approx 200$ K at $P = 1600 \pm 400$ bars and disappears at higher

P [90].

Quasielastic neutron scattering experiments show the same crossover for the average translational relaxation time of at least three different systems: (i) water hydrating lysozymes, at hydration level $h = 0.3$ g of H_2O per g of dry lysozyme, for $T \approx 220$ K, a temperature below which the protein has a glassy dynamics [76], (ii) DNA hydration water, at hydration level corresponding to about 15 water molecules per base pairs, for $T \approx 222$ K, at which DNA displays the onset of anharmonic molecular motion [91], and (iii) RNA hydration water, at a similar hydration level, for $T \approx 220$ K, where both RNA and its hydration water exhibit a sharp change in slope for the mean-square displacements of the hydrogen atoms [92],

All these results can be interpreted as a consequence of a structural rearrangement of water molecules associated with a LDL-HDL critical point [90]. In fact, along the Widom line in the supercritical region of the LDL-HDL critical point, the changes in the hydrogen bond network are consistent with the dynamic behavior observed in the experiments, as we will discuss in the following sections.

This interpretation has been criticized [93] on the base of similar crossover observed for water confined in molecular sieves [94] or for water mixtures [95] and water solutions [96]. It has also been proposed a possible interpretation as a consequence of the dynamics of (Bjerrum-type) defects due to orientationally disordered water molecules that are hydrogen bonded to less than four other water molecules [97, 98].

^{2}H-NMR studies on hydrated proteins, at a comparable hydration level as in [90], show no evidence for the crossover at 220 K and indicate that water performs thermally activated and distorted tetrahedral jumps at $T < 200$ K, which may be related to a universal defect diffusion [74]. Also, dielectric spectroscopy studies of hydrated protein show a smooth temperature variations of conductivity at 220 K and ascribe the crossover observed in neutron scattering to a secondary relaxation that splits from the main structural relaxation [75, 99].

On the other hand, numerical simulations for bulk water show that crossing the Widom line emanating from a LDL-HDL critical point, the structural change in water is maximum, as emphasized by the maximum in specific heat, and the diffusion constant has a crossover

[100]. This result is observed also in water hydrating lysozyme or DNA, where the dynamic transition of the macromolecules occurs at the temperature of dynamic crossover in the diffusivity of hydration water and also coincides with the maximum change in water structure [101].

A crossover from high-T non-Arrhenius to low-T Arrhenius behavior is observed also in simulation of water hydrating lysozyme powder in the translational correlation time and in the inverse of the self-diffusion constant, in agreement with the neutron scattering experiments, at about 223 K [102]. The activation energy for the Arrhenius regime is found to be of about 0.15 eV, as in the neutron scattering experiments [102]. Also, simulations of water hydrating elastin-like and collagen-like peptides show this crossover, but with a weaker change in the slope and an Arrhenius activation energy of about 0.43 eV, consistent with dielectric spectroscopy and nuclear magnetic resonance studies [74, 103].

It is therefore difficult not only in the experiments, but also in the models to get a clear answer about the relevant dynamic mechanisms and their relation with the thermodynamics in water at interfaces. Moreover, the relation between confined water and bulk water remains not fully understood. For this reason models that are tractable with a theoretical approach are particularly appealing in this context. With these models, in fact, simulations can be compared with analytic calculations to develop a consistent theory.

3.1 Cooperative Cell Model for a Monolayer of Water

We consider the case of water in two dimensions (2D). This case can be considered as an extreme confinement of one single layer of water between two repulsive (hydrophobic) walls when the distance between the walls is such to inhibit the crystal formation [104]. In fact, it has been shown that the relevant parameter to avoid the transition to a crystal phase is the distance between the confining wall and not the characteristics of the hydrophobic interaction with the wall [104].

Another case in which the study of a monolayer of water is relevant is when a substrate of protein powder is, on average, hydrated only by a single layer of water, and the proteins do not undergo any configurational transformation and/or large scale motion [46]. In these conditions, for a hydrophilic protein surface, we can assume that the effect of the water–protein interaction is to attract water on a surface that, by constraining the water molecule positions, inhibits its crystallization.

A very desirable feature of a model for a liquid is transferability. The parameters and effective interactions of a model are optimized to precisely reproduce static and dynamic properties of the liquid at one particular thermodynamic state point. The quality of the model is measured by the range of validity of its predictions in other state points. Unfortunately, there is no water model that is truly transferable, nor can reproduce all the properties of water [105]. Many routes have been explored to solve this issue. Molecular polarizability [106, 107] is one way to introduce effects not considered by standard pair-wise additive potentials. However, polarizable models are computationally very expensive and provide only a partial solution [108]. An alternative way is to include many–body effects into the potential. In the following we define a model with an effective many–body interaction introduced through a cooperative hydrogen bond term.

3.1.1 Definition of the Model with Cooperative Interaction

We consider N molecules in a volume V with periodic boundary conditions (p.b.c.) in two dimensions, and the size of about one single molecule (and no p.b.c.) in the third dimension. We initially consider the case in which the molecules are distributed in a homogeneous way, with each molecule $i \in [1, N]$ occupying the same volume V/N larger than a hard–core volume $v_0 \approx 102$ Å^3 due to short-range electron clouds repulsion. We consider the case in which each molecule has coordination number four, consistent with the tendency of a water molecule to minimize its energy by forming four hydrogen bonds.

The interaction Hamiltonian for water molecules is [34, 35, 37, 39]

$$\mathscr{H} = U_0(r) - J \sum_{\langle i,j \rangle} \delta_{\sigma_{ij},\sigma_{ji}} - J_\sigma \sum_{(k,l)_i} \delta_{\sigma_{ik},\sigma_{il}} \tag{3.1}$$

where $U_0(r)$ denotes the sum of all the isotropic interactions (e. g. van der Waals) between molecules at distance $r \equiv (V/N)^{1/d}$, represented by a Lennard–Jones potential with attractive energy ϵ plus a hard–core at distance $r_0 \equiv (v_0)^{1/d}$.

The second term (with $\delta_{a,b} = 1$ if $a = b$ and $\delta_{a,b} = 0$ otherwise, and $\langle i, j \rangle$ denoting that i and j are nearest–neighbors) accounts for the directional contribution to the hydrogen bond energy with strength J, where $\sigma_{ij} = 1, \dots, q$ is a (Potts) variable representing the orientational state of the hydrogen (or the lone e^-) of molecule i facing the lone e^- (or the hydrogen, respectively) of the molecules j. For the sake of simplicity we do not distinguish between hydrogen and lone e^-, associating to each molecule four equivalent bond indices σ_{ij}. We choose the parameter q by selecting 30^o as the maximum deviation from a linear bond, i. e. the O—H....O angle is less than 30^o, as estimated from Debye-Waller factors [109, 110]. Hence, $q \equiv 180^o/30^o = 6$ and every molecule has $q^4 = 6^4 \equiv 1296$ possible orientations. The effect of choosing a different value for q has been analyzed in [37].

The third term (with $(k, l)_i$ indicating each of the six different pairs of the four bond indices of molecule i) represents an interaction accounting for the hydrogen bond cooperativity and giving rise to the O–O–O correlation [41], locally driving the molecules toward an ordered (tetrahedral in the bulk) configuration with lower energy.

By defining the energy per hydrogen bond (between σ_{ij} and σ_{ji}) as the sum of the interactions in which two bonded molecules (i and j) are participating, we obtain $E_{\mathrm{HB}} = \epsilon + J + mJ_\sigma/2$, where $m = 0, \dots, 6$ is the number of cooperative interactions in which that bond variables (σ_{ij} and σ_{ji}) are partaking. If we choose as parameters $\epsilon = 5.8$ kJ/mol (consistent with the value 5.5 kJ/mol of the estimate of the van der Waals attraction based on isoelectronic molecules at optimal separation [111]), $J = 2.9$ kJ/mol and $J_\sigma = 0.29$ kJ/mol, the values of E_{HB} ranges between 8.70 and 9.6 kJ/mol depending on m. However, a definition of E_{HB} based on a cluster of 5 or 8 bonded molecules in d =3-dimensions increases this range up to 17 or 18 kJ/mol, respectively. Therefore, E_{HB} depends on the environment (the value of m and the number of molecules bonded in a cluster), as observed in computer simulation of the crystalline phases of ice [112], and has values within the range 6.3 [113]— 23.3 kJ/mol [114], proposed on the base of experiments.

Experiments show that formation of the hydrogen bonds leads to an open —locally tetrahedral— structure that induces an increase of volume per molecule [25, 64]. This effect is incorporated in the model by considering that a full bonded molecule, i. e. a molecule with four hydrogen bonds, has a molecular volume larger than a non-bonded molecule by an amount

$$\Delta v \equiv 4 v_{\rm HB}, \tag{3.2}$$

where $v_{\rm HB}$ is the volume increase per H bond. Hence, if

$$N_{\rm HB} \equiv \sum_{\langle i,j\rangle} n_i n_j \delta_{\sigma_{ij},\sigma_{ji}} \tag{3.3}$$

is the total number of hydrogen bonds in the system, the hydrogen bond contribution to the total volume is

$$\Delta V \equiv N_{\rm HB} v_{\rm HB}. \tag{3.4}$$

We adopt $r_0 = 2.9$ Å consistent with the expected value of the van der Waals radius [115], and $v_{\rm HB} = 0.5 v_0$, with $v_0 \equiv r_0^3$, corresponding to a maximum hydrogen bond distance of about 3.3 Å, consistent with the range of a water molecule's first coordination shell, 3.5 Å, as determined from the oxygen-oxygen radial distribution function [116].

3.2 The Phase Diagram

The model is studied using both mean–field (MF) analysis and Monte Carlo (MC) simulations. The MF approach has been describe in details in Ref.s [37, 117]. It consists of expressing the molar Gibbs free energy in terms of an exact partition function for a portion of the system made of a treatable number of degrees of freedom. We take into account the effect of all the rest of the system as a mean field acting on the border of this portion [27, 32, 34, 35, 37–39, 117–120].

MC simulations are performed at constant N, P, T, allowing the volume $V_{\rm MC}$ of the system to fluctuate as a stochastic variable. The average distance r between the molecules is then calculated as $r/r_0 \equiv (V_{\rm MC}/v_0 N)^{1/d}$, where $d = 2$ in two dimensions. The total volume of the system is by definition

$$V \equiv V_{\rm MC} + \Delta V, \tag{3.5}$$

where ΔV is the hydrogen bond volume contribution in Eq.(3.4). Note that ΔV is not included in the calculation of r to avoid MF–type long–range correlation in volume fluctuations in the MC simulations.

For the parameters choice $J/\epsilon = 0.5$, $J_\sigma/\epsilon = 0.05$ and $v_{\text{HB}}/v_0 = 0.5$, we find that the density ρ as a function of T at constant P displays a discontinuous change at high T and low P corresponding to the gas-liquid first order phase transition anding in a critical point where the discontinuity disappears (Fig. 7.1a). By decreasing T, the density reaches a maximum, that in real water at atmospheric pressure occurs at 4^oC. At lower T, in the supercooled state, and higher P we find another discontinuity in density, this time with a lower density at lower T (Fig. 7.1b). The system at these supercooled T displays a first order phase transition from HDL to LDL, as hypothesized in the LLCP scenario (Fig. 2).

3.2.1 Effect of Hydrogen Bond Cooperativity on the Behavior of Water

The experiments for confined water have boosted the debate over the supercooled phase diagram of water, motivating the proposal of the CPF scenario hypothesized by C. A. Angell [28], as described above. This new scenario leads to questions such as

(i) How to understand the new Angell hypothesis?

(ii) How to connect it to the other three existing hypotheses?

A recent work by Stokely et al. [36] succeeds in answering both questions (i) and (ii). Specifically, it is shown that all four existing hypotheses are cases of the cooperative water model. Thus no matter which hypothesis may be correct (if any is correct), it is possible that the underlying mechanism is basically the same—the thermodynamic properties of water can be accounted for by considering two main contributions to the hydrogen bond interaction: (a) the directional (or covalent) contribution (parametrized by J in the model) and (b) the three-body (or cooperative) contribution (parametrized by J_σ in the model).

By MF calculations and MC simulations, Stokely et al. [36] demonstrate that the balance between contributions (a) and (b) determines which of the four hypotheses presented in section 1.1. best describes experimental facts. Since the characteristic energy associated with these two contributions can be estimated, the work allows to begin to validate or contradict each hypothesis on an experimental basis.

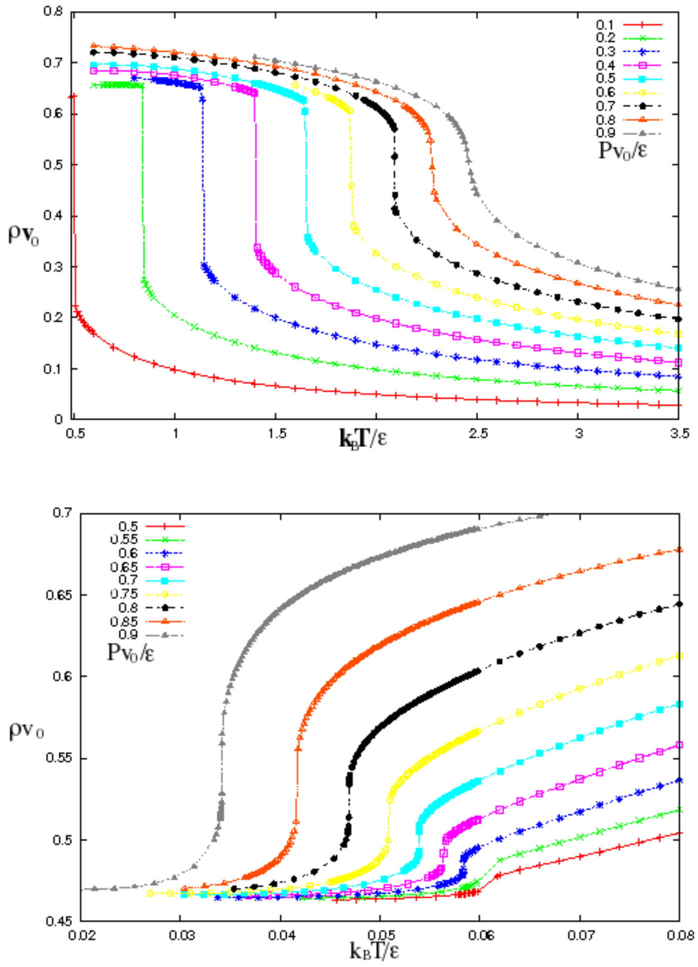

(a)

(b)

Figure 3.1: The density ρ (in units of $1/v_0$) as a function of the temperature T (in units of ϵ/k_B where k_B is the Boltzmann constant) for different values of pressure P (in units of ϵ/v_0) as calculated from MC simulation of a system with $N = 15625$ water molecules. The parameters of the model are $J/\epsilon = 0.5$, $J_\sigma/\epsilon = 0.05$ and $v_{\mathrm{HB}}/v_0 = 0.5$. (a) At high T and for (from bottom to top) values of Pv_0/ϵ from 0.1 to 0.9, we observe for $Pv_0/\epsilon < 0.8$ a discontinuity in the density corresponding to the first-order gas-liquid phase transition, with a critical P at about $(0.75 \pm 0.05)\epsilon/v_0$ and critical T at about $(2.2 \pm 0.1)\epsilon/k_B$. Note that if we choose as model parameters $\epsilon = 2.5$ kJ/mol and $r_0 = 3.2$ Å, we get an estimate $P_{C'} = 22.7 \pm 1.5$ MPa and $T_{C'} = 661 \pm 30$ K consistent with the real water critical point at about 22.064 MPa and 647 K. (b) At low T and for (from bottom to top) Pv_0/ϵ from 0.5 to 0.9, for $Pv_0/\epsilon > 0.55$ a discontinuity in ρ marks the first-order LDL-HDL phase transition.

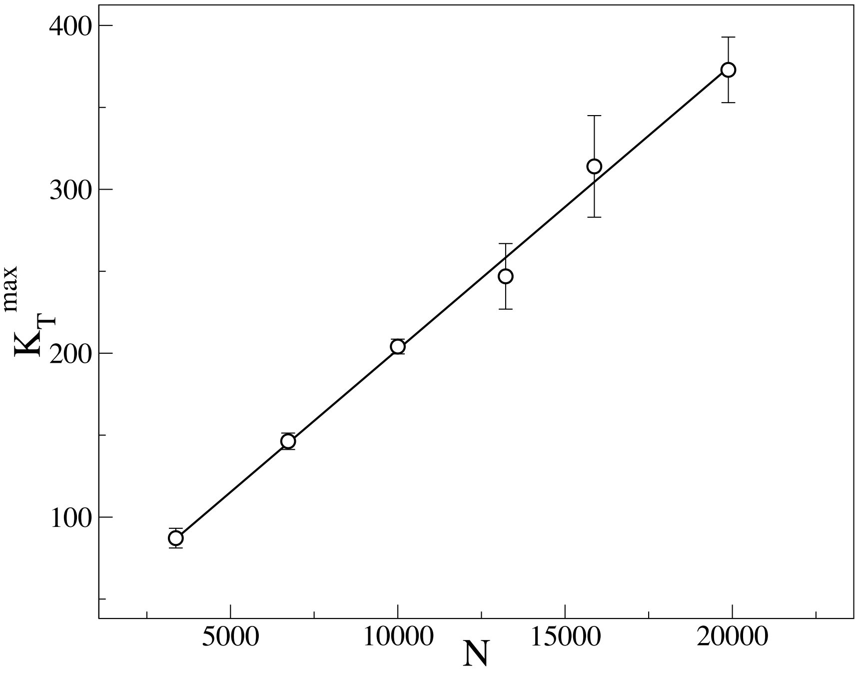

Figure 3.2: The finite size behavior of the maximum of compressibility $K_T^{\max}$ as a function of the number of water molecules N for pressure $P = 0.8\epsilon/v_0$ at low T shows a linear increase as expected at a first order phase transition.

Specifically, by fixing the parameters $J/\epsilon = 0.5$ and $v_{\mathrm{HB}}/v_0 = 0.5$, and varying the parameter J_σ/ϵ, it is possible to observe that the cooperative model reproduces all four scenarios of section 1.1. The overall picture that emerges is one in which the amount of cooperativity among H bonds (J_σ/ϵ), in relation to the H bond directional strength (J/ϵ), governs the location of a LLCP, hence which scenario is realized. For zero cooperativity, the temperature $T_{C'}$ where $K_T^{\max}$ and $\alpha_P^{\max}$ diverge is at zero temperature, and no liquid-liquid transition exists for $T > 0$–the SF scenario. For very large cooperativity, C' lies outside the region of stable liquid states, and a liquid-liquid transition extends to the entire (supercooled and superheated) liquid phase–the CPF/SL scenario. For intermediate values of H bond cooperativity, $T_{C'}$ varies in a smooth way between these two extremes–the LLCP scenario. Due to the anticorrelation between the volume and entropy associated to the H bonds, the larger $T_{C'}$, the smaller $P_{C'}$, eventually with $P_{C'} < 0$ for larger cooperativity. These cases are summarized in Fig. 6.3.

3.3 Water at Interfaces

To elucidate the relation between the protein dynamic crossover at about 220 K and the dynamic crossover observed for the average translational correlation time in the first layer of protein hydration water [76, 90–92], we perform MF calculations and MC simulations of the cooperative model of water of section 2.1. Since we are interested in cases at low humidity, we consider the case of a water monolayer hydrating an immobile surface of globular protein that, forcing the water molecules out of place with respect to crystal configurations, inhibits the crystallization. We focus on the hydrogen bonds dynamics, regardless if the hydrogen bonds are formed with the protein or among water molecules.

3.3.1 The Hydrogen Bond Dynamics for Hydrated Proteins

Following the work of Kumar et al. [32, 38, 120], Mazza et al. [46] study the orientational correlation time τ associated with the hydrogen bond dynamics of the model is in section 2.1. They confirm the occurrence of a dynamic crossover at a temperature of about $k_BT/\epsilon \approx 0.32$ corresponding to the T of maximum variation of the number of hydrogen

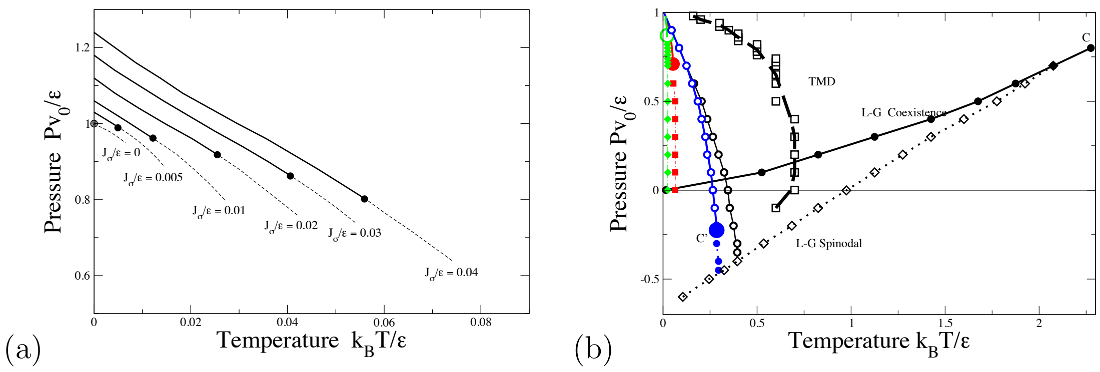

(a) (b)

Figure 3.3: The pressure P vs temperature T phase diagram of the cooperative water model for different values of J_σ/ϵ. (a) Mean field results showing the low T phase diagram with the LDL-HDL phase transition lines (solid lines, where K_T is discontinuous) and Widom lines (dashed lines, where K_T has a finite maximum) for varying J_σ/ϵ from (rightmost) 0.04, 0.03, 0.02, 0.01, 0.005 and 0 (leftmost). For each value of J_σ/ϵ solid circles indicate the LDL-HDL critical point C' where the response function (such as K_T) diverge. Hashed circle indicates the state point at $T = 0$ where K_T diverges when $J_\sigma/\epsilon = 0$. (b) The MC phase diagram for varying J_σ/ϵ for $N = 10^4$ water molecules. At high T the system displays a liquid–gas first–order phase transition line (continuous line with full circles) ending in a liquid–gas critical point C (full circle), from which departs the liquid-to-gas spinodal line (dashed line with open diamonds). At lower T, the retracing line with open squares marks the temperatures of maximum density (TMD) along isobars. All these loci do not change in an appreciable way with the value of J_σ/ϵ. The phase diagram at lower T, instead, show a strong dependence from J_σ/ϵ. For $J_\sigma/\epsilon = 0.5$, we find for any P above the spinodal line a first-order phase transition line between a HDL (at high P) and a LDL (at low P) phase (continuous line with open circles). This is the CPF scenario [28]. For $J_\sigma/\epsilon = 0.3$ we observe that the HDL-LDL phase transition ends to a critical point C' (continuous line with open circles ending in a full large circle) at negative P, as in the LLCP scenario suggested in Ref. [67]. From C' a Widom line (dashed line with full circles) departs. For $J_\sigma/\epsilon = 0.05$, C' occurs at positive P, has hypothesized in Ref. [66] and the Widom line (dashed line with full squares) extends to lower P. For $J_\sigma/\epsilon = 0.02$, C' approaches the $T = 0$ axis, as well as the Widom line (dashed line with full diamonds), going toward the limit of the SF scenario [68].

bonds, that in turn corresponds to the Widom line. They also confirm that the crossover is from a non–Arrhenius behavior at high T to another non–Arrhenius behavior [27], that closely resembles an Arrhenius behavior around the crossover.

These results are consistent with those from simulations of other models for hydrated proteins where a crossover in the translational dynamics is observed [101]. The difference here is that (i) the crossover is for the dynamics of the hydrogen bonds, (ii) in the cooperative water model the crossover can be calculated from MF and an exact relation can be found between the crossover and the Widom line, and (iii) the model can test different hypotheses. In particular, Kumar et al. have shown that the crossover at $k_BT/\epsilon \approx 0.32$ is independent of whether water at very low temperature is characterized by a LLCP or is SF. In fact, the crossover is a consequence of the sharp change in the average number of hydrogen bonds at the temperature of the specific heat maximum, that occurs in both scenarios. Kumar et al. were able also to make predictions about the P–dependence of quantities characterizing the crossover at $k_BT/\epsilon \approx 0.32$: (i) the time scale of the crossover, showing that it is independent of P (isochronic crossover); (ii) the activation energy of the apparent Arrhenius behavior at low T and (iii) the crossover temperature, showing that both (ii) and (iii) decrease linearly upon increasing P [32]. These predictions have been confirmed by Chu et al. [27, 121] in a study on the dynamics of a hydrated protein under moderately high pressures at low temperatures using the quasielastic neutron scattering method. They relate these predictions (i)–(iii) to the mechanical response of the protein to an external force, that is the average elastic constant calculated from the mean square displacement of the protein atoms. In particular, the degree of "softness" of the protein, related to the enzymatic activity, is preserved at lower T if the pressure is increased [121]. However, a criterion proposed in Ref. [32] for discriminating which scenario better describe water on the basis of the crossover at $k_BT/\epsilon \approx 0.32$, cannot be tested in the experiments since the predicted difference between the two scenarios (of the order of 1%) is within the error bars of the measurements [27].

The answer to the puzzle of which of the scenarios better describe water might be related to the very recent experimental discovery of another crossover for the hydrogen bond τ to an Arrhenius behavior at very low T, of the order of 180 K at hydration $h = 0.3$

g H_2O/g. This crossover has been observed by Mazza et al. at $k_BT/\epsilon \approx 0.07$ [46], in relation to an ordering process of the hydrogen bonds leading to the HDL-LDL critical point. The study has been possible thanks to the use of a highly efficient cluster MC dynamics [43, 122]. This very–low T crossover would reduce even more the T at which the proteins preserve their "softness", essential for their correct functionality.

3.3.2 Water Monolayer in Hydrophobic Confinement

By considering partially hydrated hydrophobic plates at a distance such to inhibit the crystallization of water at low T, Franzese and de los Santos [123] have show that water has a glassy behavior [31] for both the translational and rotational degrees of freedom when cooled down to a low P. This result is consistent with simulations of TIP4P water forming a quasi-2d amorphous when confined in a hydrophobic slit pore with wall-to-wall separation just enough to accommodate two molecular layers [124].

At higher P the hydrogen bond network builds up in a less gradual way, allowing the system to equilibrate the rotational degrees of freedom also at very low T, but not the translational degrees of freedom. This effect is emphasized by the appearance of many dehydrated regions [123], as also observed in water confined between two protein-like hydrophobic flattened surfaces at distances ranging from 0.4 to 1.6 nm [79].

When P is close to the LLCP value, the cooperativity of the hydrogen bond network induces a strong non-exponential behavior [125] for the hydrogen bond correlation function. However, both rotational and translational degrees of freedom equilibrate within the simulation time. At higher P the rotational correlation function recovers the exponential behavior and the diffusion of the system allows the formation a large dry cavity, while the rest of the surface is well hydrated. It is interesting to observe that the cooperative model allows to calculate, in the MF approximation, the diffusion constant at any T and P [126].

The hydrophobic confinement has effects also on water thermodynamics. It shifts the HDL-LDL phase transition to lower temperature and lower pressure compared to bulk water when the confinement is between plates [127, 128]. Moreover, it shifts both the line of maximum density and the liquid-to-gas spinodal toward higher pressures and lower temperatures with respect to bulk when the confinement is in a hydrophobic disordered matrix of soft spheres [80]. This result is confirmed also in the analysis performed by using the cooperative water model in confinement between hydrophobic hard spheres [129]. However, the effect of the matrix on the HDL-LDL critical point is less clear and is presently under investigation.

3.4 Conclusions

The effect of confinement is of great interest to biology, chemistry, and engineering, yet the recent experimental and simulations results are object of an intense debate. A better understanding of the physico–chemical properties of liquid water at interfaces is important to provide accurate predictions of the behavior of biological molecules [130], including the folding-unfolding transitions seen in proteins [131–133], and the dynamical behavior of DNA [91]. However, it is still unclear whether such behaviors are inherent in the structure of such molecules, or an effect of water in which they are always found, or due to the interactions between the two.

To get insight into this subject the formulation of a model that allows the development of a theory could be useful to find functional relations connecting different observables. The advantage of this approach is to have two independent ways of approaching the problem, one theoretical and the other numerical.

We have presented here several recent results obtained with a cooperative water model suitable for studies with mean field theories and with N, P, T simulations with thousands of molecules. The model has been studies in the context of water monolayers on hydrated proteins, between hydrophobic surfaces or in a hydrophobic matrix.

Some of the conclusions reached with this model are the following.

- The different scenarios proposed to interpret the low-T behavior of water are instances of the same mechanism, with different values of the directional (covalent) strength and the cooperative (many-body) interaction of the hydrogen bonds. The parameters that can be estimated from the experiments suggest that the scenario with the LLCP is the most plausible for water.

- Previous experiments showing one dynamic crossover in the water monolayer hydrating proteins, RNA and DNA are consistent with (at least) two scenarios.

- The possibility of a second dynamic crossovers detectable at lower T and lower hydration level would be consistent only with the LLCP scenario, because its origin would be related to the ordering of the hydrogen bond network.

- A consequence of the occurrence of a LLCP should be detectable when the translational and rotational dynamics of water are studied for a monolayer in a hydrophobic confinement. In particular, the rotational dynamics should appear with the strongest non-exponential behavior in the vicinity of the LLCP, as an effect of the cooperativity. Moreover, the slow increase of the number of hydrogen bonds at ow T and low P is the cause of the formation of an amorphous glassy state when the confinement is such that to inhibit the crystallization of water. Under this conditions, the dehydration of hydrophobic surfaces is characterized by the appearance of heterogeneities and cavitation.

- The hydrophobic confinement affects the thermodynamics of water by lowering the T and increasing the P of the liquid-gas phase transition and of the TMD line. It also affects the LDL-HDL phase transition in a way that is possibly more complex.

All these results are potentially relevant in problems such as the protein denaturation or the protein aggregation. Works are in progress to underpin and build up a theory of water at interfaces that could help us to acquire a better understanding of these subjects.

Chapter 4

Supercooled water in a matrix of hydrophobic nanoparticles

Many recent experiments investigate the behavior of water in confined geometries [28, 81, 84, 89, 134–137] for its relevance to nanotechnology, e.g., filtering water in carbon nanotubes [138, 139], and biophysics, e.g., intracellular water [70]. An interesting property of nanoconfined water is that it remains liquid at temperatures where bulk water freezes. The present technology allows us to observe bulk water in its liquid phase below 0°C if quenched very rapidly (supercooled), but ice formation cannot be avoided below $T_H = -41°\text{C}$ (at 1 atm). Interestingly, a number of theories and models predict a peculiar thermodynamic behavior for bulk water below T_H, with a liquid-liquid phase transition (LLPT) [32, 34, 36, 37, 39, 46, 66, 100, 140–142]. Although studying nanoconfined water could shed light on the phase diagram of deeply supercooled water, experiments and simulations [143, 144] show that fluid-fluid phase transitions in a confined space can differ from those in bulk water. Several studies using specific geometries, e.g., slits [79, 123, 124, 127, 128] or disordered matrices of disks or spheres [80, 145], have clarified some aspects but leave open questions about the thermodynamics of supercooled confined water [28, 41, 72, 81, 84, 89, 127, 134–137].

It has been proposed that supercooled water forms highly structured regions in the hydration shell of nonpolar solutes [146, 147], where the hydrogen bond (HB) network is weakened only when the size of the hydrophobic particles is above a characteristic value [148], calculated using free energy analysis to be ≈ 1 nm [77]. Muller explained experimental results by assuming enthalpic strengthening of the hydration HBs with a simultaneous entropy increase in the hydration shell [149].

4.1 Simulation details

Here, motivated by several experiments on water in a strong hydrophobic confinement [28, 70, 81, 84, 89, 134–139, 150], we consider a water monolayer of thickness $h \lesssim 1$ nm in a volume $\mathscr{V}$ partitioned into $\mathscr{N}$ cells of a square section of size $\sqrt{\mathscr{V}/\mathscr{N}h}$. Each cell is occupied by either a water molecule or a hydrophobic particle. Particles can occupy more than one cell, are spherical and approximated by the set of cells with more than 50% of their volume inaccessible to water. Particles are randomly distributed and form a fixed matrix that mimics a porous system or a rough atomic interface. $N \leq \mathscr{N}$ is the total number of cells occupied by water molecules and $V \leq \mathscr{V}$ is their total volume. The Hamiltonian for water-water interaction is [32, 34, 36, 37, 39, 46]

$$\mathscr{H} \equiv \sum_{ij} U(r_{ij}) - J N_{\mathrm{HB}} - J_\sigma \sum_i n_i \sum_{(k,\ell)_i} \delta_{\sigma_{ik},\sigma_{i\ell}}. \tag{4.1}$$

Here r_{ij} is the distance between water molecules i and j, $U(r) \equiv \infty$ for $r < r_0 \equiv 2.9$ Å, the water van der Waals diameter, $U(r) \equiv \epsilon_w[(r_0/r)^{12} - (r_0/r)^6]$ for $r \geq r_0$ with $\epsilon_w \equiv 5.8$ kJ/mol, the van der Waals attraction energy, and $U(r) = 0$ for $r > r_c = \sqrt{\mathscr{V}/h}/4$, the cut-off distance.

The second term in Eq. (9.1) describes the directional HB interaction, with $J \equiv 2.9$ kJ/mol, and the total number of HBs $N_{HB} \equiv \sum_{\langle i,j \rangle} n_i n_j \delta_{\sigma_{ij},\sigma_{ji}}$, where $n_i \equiv 1$ for a water molecule when $N v_0/V \geq 0.5$ (liquid density, with $v_0 \equiv h r_0^2$) and 0 otherwise, and $n_i \equiv 0$ for a hydrophobic particle. A HB breaks when the OH—O distance exceeds $r_{\max} - r_{\mathrm{OH}} = 3.14$Å, because $n_i n_j = 0$ when the O–O distance $r \geq r_{\max} \equiv r_0\sqrt{2} = 4.10$Å ($r_{\mathrm{OH}} = 0.96$Å). It also breaks if $\widehat{\mathrm{OOH}} > 30^o$. Therefore, only 1/6 of the orientation range $[0, 360°]$ in the OH–O plane is associated with a bonded state. By allowing $q = 6$ possible states for each index σ_{ij}, we account for the entropy loss associated with the formation of a HB because, by definition, $\delta_{\sigma_{ij},\sigma_{ji}} \equiv 1$ if $\sigma_{ij} = \sigma_{ji}$, $\delta_{\sigma_{ij},\sigma_{ji}} \equiv 0$ otherwise.

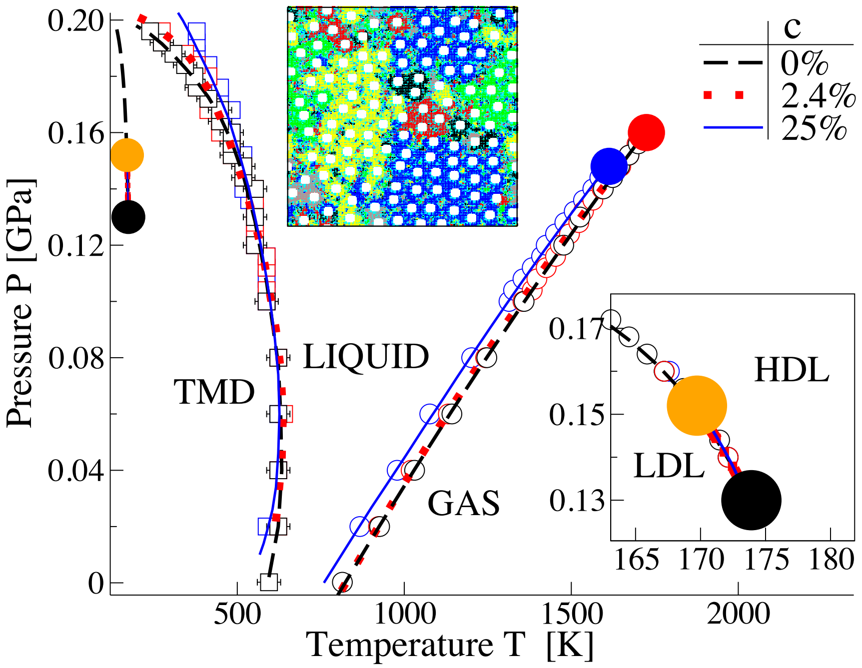

Figure 4.1: P–T phase diagram for different nanoparticle concentrations c. Open circles estimate liquid-to-gas spinodal line, squares estimate TMD line. In this and all other figures, where not shown, errors are smaller than the symbol size. Lines are guides for the eyes (dashed for $c = 0$, dotted for 2.4%, full for 25%). Critical points are shown as large full circles. The liquid–gas critical point is the same for $c = 0$ and 2.4%, while occurs at lower P and T for $c = 25\%$. Lower inset: enlarged view of the low-T region. The first-order LLPT ends in a critical point at $T \simeq 174$ K and $P \simeq 0.13$ GPa for all c. At $c = 2.4\%$ and 25% at $P > 0.15$ GPa the first-order LLPT is no longer detected, indicating a new high-P critical point. Upper inset: configuration at $T \simeq 160$ K and $P = 0.18$ GPa for $c = 25\%$. Hydrophobic nanoparticles are in white; HBs are in different colors for different ordered domains.

The notation $\langle i,j \rangle$ denotes that the sum is performed over nearest–neighbors (n.n.) water molecules i and j, so that each water molecule can form up to four HBs.

HB formation increases the volume per molecule, because it leads to an open network of molecules with reduced nearest neighbors with respect to close molecular packing. We incorporate this effect by an enthalpy increase Pv_{HB} for each HB, where $v_{\mathrm{HB}}/v_0 = 0.5$ is the average density increase from low density ice Ih to high density ices VI and VIII.

The third term in Eq. (9.1) accounts for the HB cooperativity, with $J_\sigma \equiv 0.29$ kJ/mol, where $(k,\ell)_i$ indicates each of the six different pairs of the four bond-indices σ_{ij} of a molecule i. It gives rise to the O–O–O correlation, locally driving the molecules toward an ordered configuration [41].

The water-nanoparticle interaction is purely repulsive, $U_{\mathrm{wn}}(r) \equiv \epsilon_h[(r_0/r)^{12}]$, with $\epsilon_h \equiv \epsilon_w\sqrt{0.1} = 1.8$ kJ/mol [80], where $r < r_c$ is the distance between the water cell and each of the cells occupied by the nanoparticle. The restructuring effect of hydrophobic particles on water is incorporated by replacing J and J_σ in the hydration shell with $J^{\mathrm{h}} = 1.3J$ and $J^{\mathrm{h}}_\sigma = 1.3J_\sigma$, following [151]. Because bonding indices facing the nanoparticle cannot form HBs, at intermediate T they have a number of accessible states larger than those facing water molecules, inducing an increase of hydration entropy [149].

We perform Monte Carlo (MC) simulations for constant pressure P, temperature T, and N, with variable water volume $V \equiv V_0 + N_{HB}v_{HB}$, where $V_0 \geq Nv_0$ is a stochastic continuous variable that fluctuates following the MC acceptance rule [122]. We simulate systems with $\mathscr{N} \leq 1.6 \times 10^5$ within a fixed matrix of spherical nanoparticles of radius $R = 1.6$ nm, with nanoparticle concentration $c \equiv (\mathscr{N} - N)/\mathscr{N} = 2.4\%$ and 25%. We repeat the analysis for $R = 0.4$ nm. For $c = 0$, the model has a phase diagram with a first-order LLPT, between a low density liquid and a high density liquid, starting at $P \simeq 0.2$ GPa for $T \to 0$ and ending in a critical point at $T \simeq 174$ K and $P \simeq 0.13$ GPa [32, 34, 36, 37, 39, 46].

4.2 Results

We find that for $c > 0$ the liquid-gas spinodal is shifted to lower T and the line of temperature of maximum density (TMD) is shifted to lower T at low P and to higher T at high P, with respect to the $c = 0$ case, reminiscent of results for other models of confined water [80, 128]. We find stronger changes for increasing c (Fig. 4.1).

Further, we find that confinement drastically reduces volume and entropy fluctuations at low T. To quantify this reduction, we calculate volume fluctuations, entropy fluctuations, and cross-fluctuations of volume and entropy, and analyze the associated measurable response function, respectively, isothermal compressibility K_T, isobaric specific heat C_P and isobaric thermal expansion coefficient α_P, e.g., see Figs. (5.7) and (5.5). For a water monolayer with $\mathscr{N} = 1.6 \times 10^5$ cells confined within nanoparticles with $R = 1.6$ nm at $c = 25\%$, we find a maximum $K_T^{\max}$ along the isobar at $P \simeq 0.16$ GPa that is 99.7% smaller than the $c = 0$ case. If we decrease c to 2.4%, the reduction of $K_T^{\max}$ is still remarkable: 92.3% (Fig. 5.5). We find similar reductions for $C_P^{\max}$ and $\alpha_P^{\max}$.

Such a dramatic $K_T^{\max}$ reduction at low T and high P suggests a possible change in the region of the phase diagram where water at $c = 0$ has the LLPT. The general theory of finite size scaling tells us that at a first-order phase transition, $K_T^{\max}$, $C_P^{\max}$ and $\alpha_P^{\max}$ increase linearly with the number of degrees of freedom, here equal to $4N$. We find a linear increase for 0.14 GPa$\leq P \leq 0.20$ GPa for $c = 0$, and only for 0.14 GPa$\leq P < 0.16$ GPa for $c = 25\%$ and 2.4%, consistent with the absence of a first-order LLPT outside these ranges.

To better understand this new feature, i.e., the effect of confinement on the LLPT at high P, we study the finite size scaling of the Binder cumulant [152, 153] $U_{\mathscr{N}} \equiv 1 - [\langle V^4\rangle_{\mathscr{N}}/3\langle V^2\rangle^2_{\mathscr{N}}]$, where $\langle\cdot\rangle_{\mathscr{N}}$ stands for the thermodynamic average for a system with $\mathscr{N}$ cells. For $\mathscr{N} \to \infty$, at fixed c and P, $U_{\mathscr{N}} = 2/3$ for any T away from a first-order phase transition, while $U_{\mathscr{N}}^{\min} < 2/3$ at a first-order phase transition [152, 153].

For $c = 0$, we find that $U_{\mathscr{N}}^{\min} < 2/3$ for $\mathscr{N} \to \infty$ at 0.14 GPa$\leq P \leq 0.20$ GPa, while $U_{\mathscr{N}}^{\min} = 2/3$, within the error bar, at $P = 0.12$ GPa (Fig. 5.9a). Hence, this analysis confirms that for $c = 0$ there is a first-order LLPT in the range 0.14 GPa$\leq P \leq 0.2$ GPa.

For $c = 2.4\%$ and 25%, we find that, for large $\mathscr{N}$, $U_{\mathscr{N}}^{\min} < 2/3$ at 0.14 GPa, but not at 0.12 GPa or at

$P \geq 0.16$ GPa (Fig. 5.9b,c). Hence, for $c = 2.4\%$ and 25% the first-order LLPT occurs only in a limited range of pressures around 0.14 GPa, consistent with our results for $\langle(\delta V)^2\rangle$ (Fig. 5.7) or $K_T^{\max}$ (Fig. 5.5), with two end-points: one at ≈ 0.15 GPa, another at ≈ 0.13 GPa (Fig. 4.1).

4.3 Discussion

We interpret our findings as follows. As a consequence of the stronger HB in the solutes hydration shell, at low T the hydration water is more ordered than the $c = 0$ case. However, shells around different nanoparticles have a different local orientational order. This generates competing domains, reminiscent of the locally structured regions proposed in Ref. [146, 147], and exhibits no macroscopic order (Fig. 4.1 upper inset). The large decrease in fluctuations and response functions, e.g. K_T, is due to the many domain boundaries. Our results for c as low as 2.4% suggest that that the decrease is due to the introduction of a characteristic length scale, inversely proportional to c, that limits the growth of the ordered structured regions. This is consistent also with the results for $K_T^{\max}$ (Fig. 5.5), where the lower is c, the larger is N beyond which the confined behavior deviates from the $c = 0$ case.

In previous theoretical analysis, with water confined by a fixed matrix of randomly distributed Lennard-Jones disks, the reduction of compressibility was observed only for large hydrophobic obstacle concentrations [145]. Here, instead, we find that K_T is reduced for very low c, possibly because of the different water-nanoparticle interaction.

Our results are qualitatively consistent with recent experiments on H_2O confined in the hydrophobic mesoporous material CMK-1-14 consisting of micrometer-sized grains, each with a 3-dimensional interconnected bicontinuous pore structure, with an average pore diameter 14 Å, at a hydration level of 99% at ambient pressure [150]. Zhang et al. find that the TMD is shifted down by 17 K with respect to the hydrophilic confinement in silica mesopores and that α_P shows a much broader peak, spanning from 240 to 180 K, in

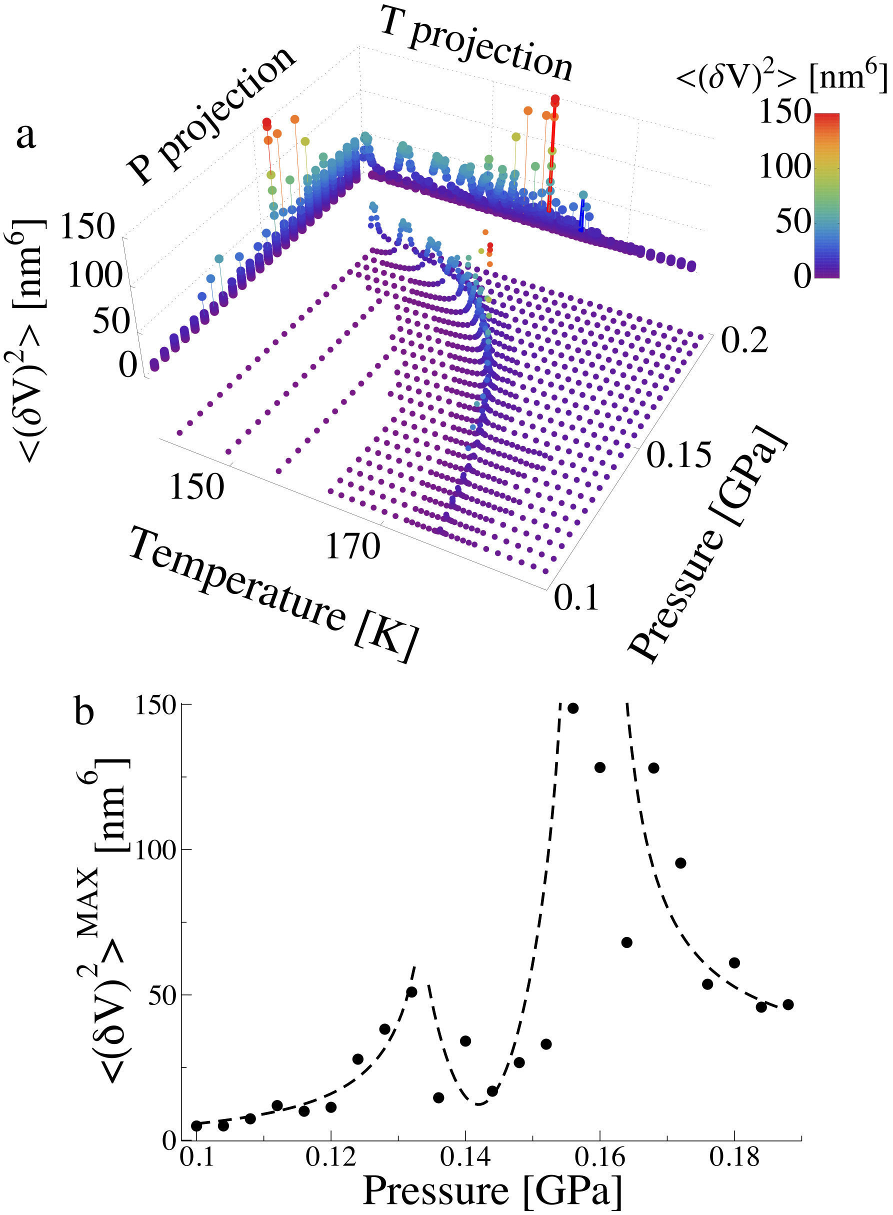

Figure 4.2: (a) Volume fluctuations $\langle(\delta V)^2\rangle$ for $c = 25\%$ and $\mathcal{N} = 10^4$ have maxima that follow a locus in the $P - T$ plane that does not change, within the error bars, with c or $\mathcal{N}$. The projections $\langle(\delta V)^2\rangle$ vs P or vs T clarify that the maxima do not change monotonically with P or T. (b) The projection of maxima of $\langle(\delta V)^2\rangle$ increases approaching $P = 0.132$ GPa and 0.156 GPa, consistent with our estimate of two critical points at ≈ 0.13 GPa and ≈ 0.15 GPa. Dashed lines are guides for the eyes.

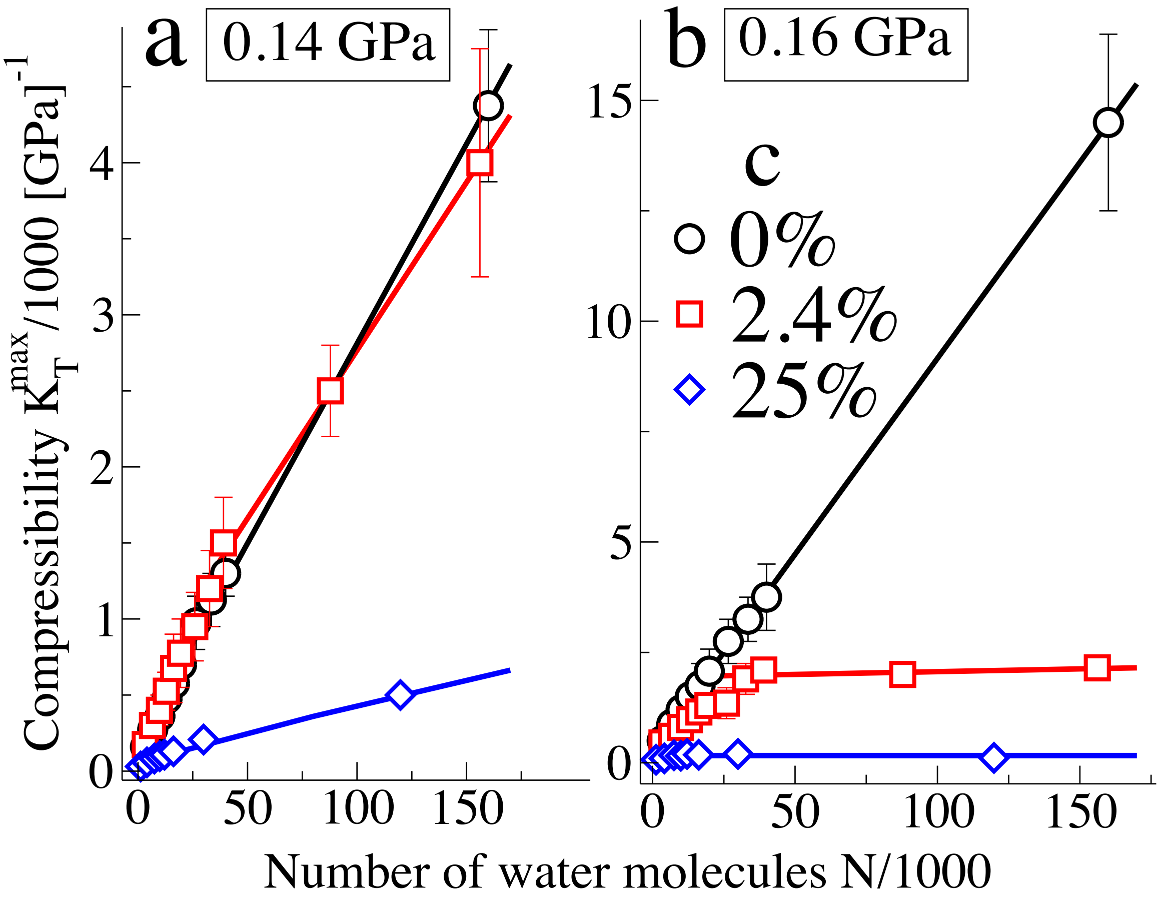

Figure 4.3: Maxima $K_T^{\max}$ of the isothermal compressibility $K_T \equiv \langle(\delta V)^2\rangle/(k_B T\langle V\rangle)$ vs number of water molecules N for $c = 0$, 2.4% and 25%. (a) Linear increase in $K_T^{\max}$ with N for $P = 0.14$ GPa, consistent with a first-order LLPT for all c. (b) At $P = 0.16$ GPa, $K_T^{\max}$ increases linearly for $c = 0$ indicating a first-order LLPT, but saturates for $c = 2.4\%$ and 25%, consistent with the absence of a first-order LLPT [2].

---

[2] At $c = 0$, $K_T^{\max}$ increases for higher P because $\langle(\delta V)^2\rangle$ depends weakly on P, and $K_T^{\max}$ occurs at lower $T\langle V\rangle$.

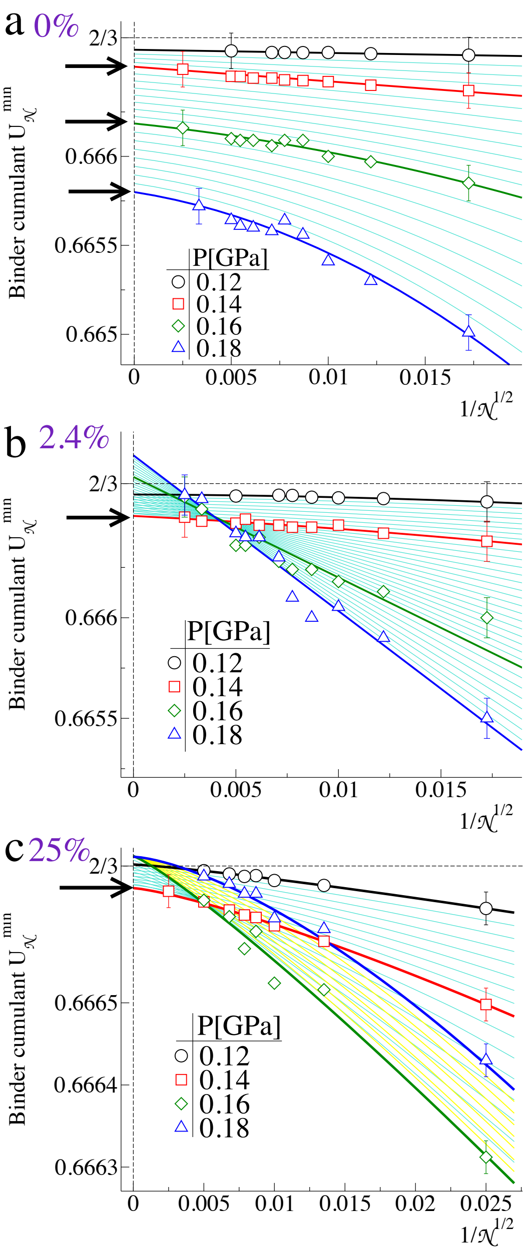

Figure 4.4: (a) At $c = 0$, for $\mathscr{N} \to \infty$ is $U_{\mathscr{N}}^{\min} = 2/3$, within the error bar, for $P = 0.12$ GPa and tends to a value $\leq 2/3$ for $P \geq 0.14$ GPa, indicating a first-order LLPT for $P \geq 0.14$ GPa. At nanoparticle concentrations $c = 2.4\%$ (b) and 25% (c), for $\mathscr{N} \to \infty$ we find $U_{\mathscr{N}}^{\min} < 2/3$ only for $P = 0.14$ GPa, indicating that the first-order LLPT is washed out by the hydrophobic confinement at high P. For sake of clarity, typical error bars are indicated only for a few points. Lines through the points are fits, while other lines are linear interpolations between fits at intermediate P. Black arrows mark isobars crossing the first-order LLPT line.

contrast to the sharp peak at 230 K in hydrophilic confinement [150], reminiscent of our results on the shift of TMD and the reduction of the response functions with respect to the $c = 0$ case.

Recent results for small angle x-ray scattering for aqueous solutions of amphiphilic tetraalkyl-ammonium cations at ambient conditions suggest that the strengthening of the structure of hydration water is present only for solutes with radius smaller than ≈ 0.44 nm [215]. We therefore repeat our analysis for small nanoparticles with $R = 0.4$ nm, and find that our results are robust if the amount of hydrophobic interface in contact with water is kept constant with respect to the case of $R = 1.6$ nm.

4.4 Conclusion

In conclusion, we predict that a water monolayer confined in a fixed matrix of hydrophobic nanoparticles at concentration c displays changes in the thermodynamics and a drastic reduction, $> 90\%$, in K_T, C_P, and α_P with respect to the $c = 0$ case. At c as small as 2.4% the first-order LLPT at high P is no longer detected.

Chapter 5

Hydrophobic nanoconfinement suppresses fluctuations in supercooled water

Water is frequently found in nature in its supercooled state. This fact has stimulated intense experimental and theoretical research [28, 81, 84, 89, 134–136, 155–157]. In the deeply supercooled region, however, the direct observation of bulk water is extremely difficult due to the inevitable crystallization that occurs. One way to overcome this experimental difficulty is to confine water to nanometric distances. Nanoconfined water remains liquid down to very low temperatures [157] opening the possibility of exploring the properties of confined water in a temperature range that is inaccessible when the subject is bulk liquid water. A number of important technological and biological applications depend on understanding the phase diagram of water [28, 81, 84, 89, 134–137, 158–161]. For example, hydrophobic and hydrophilic interactions are important driving forces for the self-assembling of micelles or membranes and are fundamental for protein folding. Water is enclosed in cell membranes and is a typical solvent for proteins [130]. The study of water confined in carbon nanotubes is opening new technological perspectives [70], and thus there has been an increasing interest in studying confined water in various geometries, such as nanopores or nanotubes, protein hydration water, and intracellular water [138, 139, 162–168].

One very peculiar property of supercooled water is the phenomenon of polyamorphism, i.e., the presence of two or more liquid or glassy states which was first observed in glassy water [58, 62, 169]. There are two different forms of amorphous glassy water: a low density amorphous (LDA) and a high density amorphous (HDA) that are separated by a first order phase transition line. Consequently, polyamorphism for liquid water with low density liquid (LDL) and a high density liquid (HDL) was proposed [66, 170, 171] triggering experimental investigations [172, 173]. A number of current theories and models predict a first-order liquid-liquid phase transition (LLPT) for bulk water between LDL and HDL below the homogeneous nucleation temperature T_H^{bulk}, where bulk water freezes spontaneously [27, 32, 34, 36, 37, 39, 46, 66, 100, 101, 140, 141, 156, 174–177]. Recently, Limmer and Chandler performed free-energy calculations for the ST2 water model concluding that there is no evidence for the LLPT [178]. However, more recent calculations reach a different conclusion supporting the existence of the LLPT [179, 181, 182, 305].

Recent studies on water in various confined geometries—in which water crystallization is suppressed down to very low temperatures—have investigated the region in the pressure-temperature (P–T) phase diagram where a first order LLPT is predicted. However, no definitive answer has been given regarding the thermodynamic implications of confinement and its relevance to the phase diagram of bulk water. Water differs from most liquids in that there is an important thermodynamic locus in the P–T phase diagram—the line where, at a given P, the T dependence of the density exhibits a maximum, commonly referred to as the temperature of maximum density (TMD). A shift to lower T of the TMD line, and its curvature modification, have been reported for confined water, suggesting important changes in the phase diagram deep in the supercooled region [80, 183]. In general, experiments and simulations [143, 144, 184] show that LLPTs in a confined space can differ from those in bulk. Therefore, there are aspects of the thermodynamics of confined water that remain open to debate [41, 72].

In computer simulations, one possible approach to these studies is to develop atomistic models of water utilizing a geometry such as slits [79, 123, 124, 127, 128, 185] or a disordered matrix of disks or spheres [80, 183]. The main difficulty in this approach is that these simulations are time-consuming, and are usually limited to only a few hundred water molecules.

Another possible approach is to consider coarse-grained models of water. Coarse graining can be done at different levels, i.e., at the level of a single water molecule [34, 35, 37, 68, 186] or a few molecules [187], depending on the properties being studied. Here we present results for a water model that is coarse-grained at the single molecule level. Molecular details are sacrificed for the benefit of computational speed, which allows more extensive studies, and theoretical simplicity, which allows analytic calculations. Here we ask whether the confinement in a fixed matrix of hydrophobic nanoparticles changes the thermodynamics of a water monolayer at temperatures below T_H^{bulk}.

Using Monte Carlo simulations, our results for a coarse-grained model of a water monolayer [129] show that even a small presence of hydrophobic nanoparticles can drastically suppress thermodynamic fluctuations, and wash out the coexistence of the two types of liquid supercooled water at high pressures.

The paper is organized as following. Sections 2, 3, and 4 outline details of the model and Monte Carlo simulations. Section 5 presents the results. Discussion and Conclusions are given in Section 6.

5.1 Coarse-Grained Model of water monolayer

We consider a coarse-grained model for water in two dimensions confined between two smooth hydrophobic plates, whose interaction with water is purely repulsive and represented by a steric hard-core exclusion. It has been previously shown that when the distance between the plates is approximately 0.5 nm the monolayer of water remains in its liquid phase, while the properties of the confined water are only weakly dependent on the details of the confining potential between smooth walls [104, 188]. We partition a water monolayer of thickness $h \simeq 0.5$ nm and volume $\mathscr{V}$ into $\mathscr{N}$ square cells of equal length $\sqrt{\mathscr{V}/\mathscr{N}h}$. We coarse-grain over the position orthogonal to the walls and consider only the projection of water molecules in a plane parallel to the wall. We further coarse-grain the detailed position of each molecule, discretizing it to the resolution given by our square partition of the parallel plane, assigning to each cell an occupancy variable

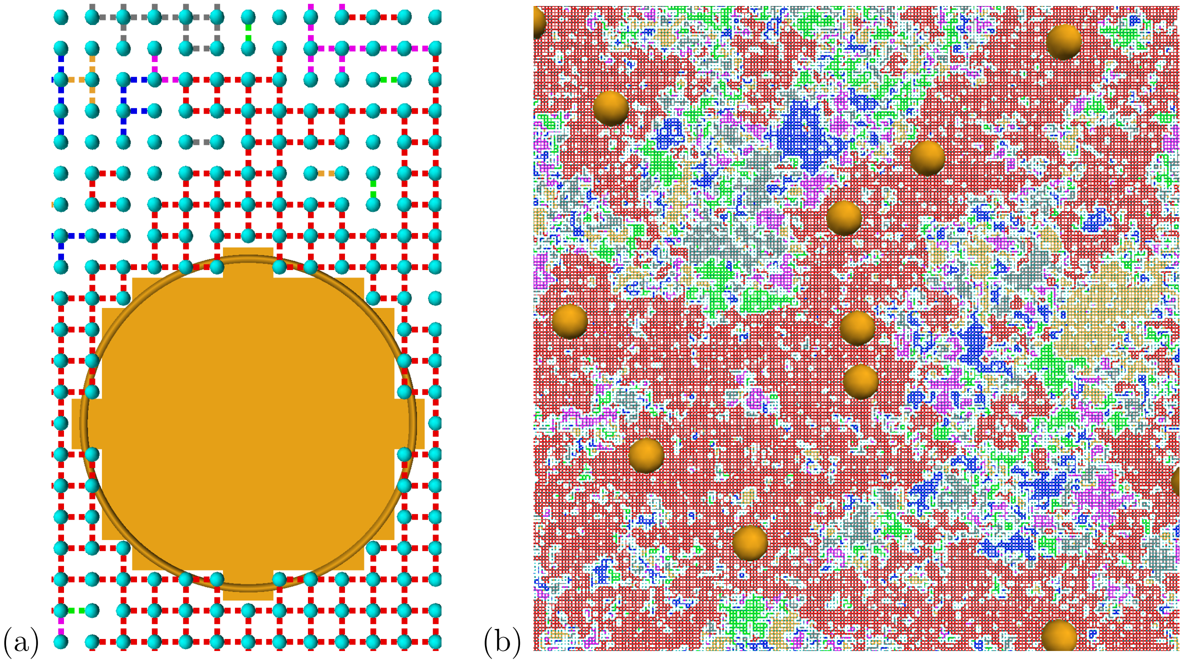

Figure 5.1: (a) Snapshot magnified around the region occupied by the hydrophobic nanoparticle (golden irregular polygon). The size of the hydrophobic nanoparticle is controlled by the number of cells it can occupy, and its shape is approximated by a disk composed of cells that fall within radius R. Here the radius of the hydrophobic nanoparticle is $R = 1.6$ nm. Small cyan spheres are water cells with four bond indices (small squares) with six possible colors corresponding to the $q = 6$ possible values of the bonding variables. Only the bond indices that participate in the formation of the hydrogen bond are shown here.(b) Snapshot of the monolayer with 2.4% of its volume occupied by hydrophobic nanoparticles (big golden spheres) with $R = 1.6$ nm. Hydrophobic nanoparticles are randomly placed and form a fixed matrix. Hydrogen bonds are visualized by different color lines between water cells (cyan small spheres), depending on their relative state.

$n_i = 1$ if the cell is occupied by a water molecule, or $n_i = 0$ if it is occupied by a hydrophobic nanoparticle. We consider the case in which there are no empty cells in the system and hydrophobic nanoparticles can occupy more than one cell, depending on their size. Hydrophobic nanoparticles are disks of radius R and are approximated by a set of cells that fall within the πR^2 area centered on each hydrophobic nanoparticle [Fig. 5.1(a)]. Hydrophobic nanoparticles are randomly distributed and form a fixed matrix that mimics a porous system or a rough atomic interface [Fig5.1(b)]. $N \leq \mathscr{N}$ denotes the total number of cells occupied by water molecules and $V \leq \mathscr{V}$ denotes their total volume.

In order to implement a constant P ensemble we include volume V fluctuations in the model by allowing a global rescaling of the cell length $\sqrt{\mathscr{V}/\mathscr{N}h}$. The cell length coincides with the distance among nearest neighbor molecules. Therefore, the volume fluctuations induce fluctuations of r_{ij} (i) the distance between any two water molecules i and j and (ii) the distance between any water molecule i and any cell j occupied by the nanoparticle. Since a continuous range of possible volume fluctuations is allowed, the distances change as continuous variables, despite the discrete lattice partition of the space. As the result, the fluctuations of the cell size and therefore the fluctuations of the volume occupied by a nanoparticle are a consequence of the change of the coarse-graining scale. Therefore, it does not imply that the nanoparticle volume is increasing or decreasing, but that the coarse-graining length-scale undergoes (small) fluctuations.

The system is described by the Hamiltonian [27, 32, 34, 36, 37, 39, 46, 101, 174, 175]

$$\mathscr{H} \equiv \sum_{ij} U(r_{ij}) - JN_{\mathrm{HB}} - J_\sigma \sum_i n_i \sum_{(k,\ell)_i} \delta_{\sigma_{ik},\sigma_{i\ell}}. \tag{5.1}$$

The first term, $U(r_{ij}) \equiv U_w(r_{ij}) + U_h(r_{ij})$, is given by the sum of the isotropic part of the water-water interaction $U_w(r_{ij})$ and the water-nanoparticle interaction $U_h(r_{ij})$. The two pair interactions are defined as

$$U_w(r) \equiv \begin{cases} \infty & \text{for} \quad r < r_0, \\ \epsilon_w[(\frac{r_0}{r})^{12} - (\frac{r_0}{r})^6] & \text{for} \quad r \geq r_0, \\ 0 & \text{for} \quad r > r_c \end{cases}$$

$$U_h(r) \equiv \begin{cases} \infty & \text{for} \quad r < r_0, \\ \epsilon_h[(\frac{r_0}{r})^{12}] & \text{for} \quad r \geq r_0, \\ 0 & \text{for} \quad r > r_c \end{cases} \tag{5.2}$$

where $r_0 \equiv 2.9$ Å is the water van der Waals diameter, $\epsilon_w \equiv 5.8$ kJ/mol is the water-water attraction energy, $r_c = \sqrt{\mathscr{V}/h}/4$ is the cut-off distance. For the water-water case this term includes the short–range repulsion of the electron clouds and all the isotropic long–range attractive interactions, such as the weak instantaneous induced dipole-dipole (London) interactions between the electron clouds of different molecules and the stronger isotropic part of the hydrogen bond [189].

For the water-hydrophobic nanoparticle case we assume that the interaction is purely repulsive, with $\epsilon_h \equiv \epsilon_w\sqrt{0.1} = 1.8$ kJ/mol to soften the repulsive ramp. We observe here that a hydrophobic nanoparticle could also have a small attractive term in the water-hydrophobic nanoparticle interaction, since dispersive van der Waals forces are always present. However, the repulsive interaction is typically one order of magnitude stronger than the attractive term [190]. Our neglect of the attractive water-nanoparticle interaction is, therefore, reasonable at first approximation and has been adopted by other authors [80].

The second term of Eq. (9.1) describes the strong directional component of the hydrogen bond (HB) due to the dipole-dipole interaction between the highly concentrated positive charge on each H and each of the two excess negative charges concentrated on the O of another water molecule. To account for the different bonding configurations of each water molecule, we assign to each cell i four bond variables $\sigma_{ij} = 1, ..., q$ (one for each nearest neighbor cell j), representing the orientation of molecule i with respect to molecule j. A common assumption is that a HB breaks when $\widehat{\mathrm{OOH}} > 30^o$. Therefore, only 1/6 of the orientation range $[0, 360°]$ in the OH–O plane is associated with a bonded state. Hence, every molecule has $q^4 = 6^4 \equiv 1296$ possible orientations and by considering the index σ_{ij} we account for the entropy loss associated with the formation of a HB. We say that two molecules in nearest neighbor (n.n.) cells form a HB only if they are correctly oriented, by definition, $\delta_{\sigma_{ij},\sigma_{ji}} \equiv 1$ if $\sigma_{ij} = \sigma_{ji}$, $\delta_{\sigma_{ij},\sigma_{ji}} \equiv 0$ otherwise. The total number of HBs is

$$N_{\rm HB} \equiv \sum_{\langle i,j \rangle} n_i n_j \delta_{\sigma_{ij},\sigma_{ji}}, \tag{5.3}$$

where $n_i \equiv 0$ for a nanoparticle and 1 for a water molecule. The notation $\langle i, j\rangle$ denotes that the sum is performed over n.n. water molecules i and j, so that each water molecule can form up to four HBs. We consider a bond energy $J \equiv 2.9$ kJ/mol, as adopted in Ref. [46, 101, 174]. Since $\epsilon_w = 2J$, the HBs are formed in large numbers only in the condensed liquid phase.

Hydrophobic nanoparticles are treated as a fixed random confining matrix and the bonding variable facing the nanoparticles cannot participate to any hydrogen bond, but contribute to the entropy of the system and are correlated to the other three bonding variables of the same water molecule.

Experiments have demonstrated that the formation of a HB leads to an open, locally tetrahedral, structure that induces an increase of volume per molecule within the second shell [25, 64]. We incorporate this effect by an enthalpy increase $Pv_{\rm HB}$ for each HB, where P is pressure and $v_{\rm HB}/v_0 = 0.5$ is the average volume increase from high density ices VI and VIII to low density ice Ih, and $v_0 \equiv hr_0^2$. Then the total water volume of the system is defined as

$$V \equiv V_0 + N_{\rm HB} v_{\rm HB}, \tag{5.4}$$

where $V_0 \geq N v_0$ is a continuous variable that changes with pressure in such a way that V follows the water equation of state [122]. Note that only the term V_0 of the fluctuating volume is considered for the calculation of distances r appearing in the Eq. (9.2) for the isotropic interaction $U(r)$, because the HB formation does not imply an increase of molecular distances, but only an increase of the local tetrahedral structure with the exclusion of interstitial water molecules between the first and the second shell. This exclusion induces the increase of volume per water molecule mimicked by the Eq. (9.4).

The third term accounts for the experimental fact that at low T the O–O–O angle distribution in water becomes sharper around the tetrahedral value [41], consistent with a cooperative behavior among bonds [36] as a consequence of many-body interaction of water molecules. We model this interaction by including a coupling $J_\sigma \equiv 0.29$ kJ/mol among the four bonding indices of the same water molecule in the third term of Eq. (9.1), where $(k, \ell)_i$ denotes each of the six different pairs of the four bond-indices σ_{ij} of a molecule i. Since is $J_\sigma < J$, this term locally drives the HBs formed by a water molecule toward an ordered configuration, mimicking the many-body interaction that induces the locally ordered structure of the HBs.

5.2 Hydrophobic Interaction

Confinement along one dimension inhibits the formation of 3D ice at $T < T_H^{\rm bulk}$ [128, 185], and forces the water molecules to freeze into a lattice characterized by orientational disorder [128, 185]. The characteristics of the lattice are closely related to those of the hydrophobic surface. For example, strong template effects are present for the graphene surface [191] while the absence of atomic characterization of the surface leads to a generic square arrangement [128, 185]. In any case, the limited space left open to water induces the formation of an almost 2D structure where the translational dynamics at low T is very limited, while the HB breaking-and-formation dynamics is present also at low T [128, 185]. All of these features are reproduced in the coarse-grained model considered here [123]. Moreover, the possibility of exploring very low temperatures and very high pressures by means of this coarse-grained water model allows us to predict a phase diagram with a first-order LLPT, between a LDL and a HDL, starting at $P \simeq 0.2$ GPa for $T \to 0$ and ending in a critical point at $T \simeq 174$ K and $P \simeq 0.13$ GPa [27, 32, 34, 36, 37, 39, 46, 101, 174, 175] [Fig. 5.6(a)]. Furthermore, in the vicinity of the liquid-liquid critical point, the HB dynamics displays the largest heterogeneity, consistent with the presence of cooperative dynamics [123], and with experiments for a water monolayer hydrating hemoglobin [192].

In the case considered here, water is also confined by hydrophobic nanoparticles to the two directions parallel to the infinite flat surfaces. As shown in (9.2), the water-hydrophobic nanoparticle interaction is repulsive and leads to interesting physics at low T. In particular, it has been proposed that supercooled water forms highly structured regions in the hydration shell of nonpolar solutes [146], where the hydrogen bond network is weakened only when the size of the hydrophobic nanoparticles is above a characteristic value [148], calculated using free energy analysis to be ≈ 1 nm [77]. Moreover Muller showed that experimental results can be explained only by assuming enthalpic strengthening of the hydration HBs with a simultaneous entropy increase in the hydration shell [149].

In our model the restructuring effect of hydrophobic nanoparticles on water is incorporated by replacing the parameter J and J_σ in the hydration shell with $J^{\mathrm{h}} = 1.30J$ and $J^{\mathrm{h}}_\sigma = 1.30J_\sigma$, following Patel *et al.* [151]. Because bonding indices facing the hydrophobic nanoparticle cannot form HBs, at intermediate T they have a number of accessible states larger than those facing water molecules, inducing an increase of hydration entropy consistent with the description of the hydrophobic effect given by Muller [149] and subsequently modified by Lee and Graziano [193].

5.3 Monte Carlo Simulations

We perform Monte Carlo (MC) simulations in two dimensions for constant P, T, and N. We use the protocol of heating the system starting from a completely ordered configuration. We simulate systems with $\mathscr{N} \leq 1.6 \times 10^5$ within a fixed matrix of hydrophobic nanoparticles of radius $R = 1.6$ nm, with hydrophobic nanoparticle concentration $c \equiv (\mathscr{N} - N)/\mathscr{N} = 2.4\%$ and 25%. We repeat the analysis for $R = 0.4$ nm for a range of concentrations between 0.5% and 22.5% for a fixed system size of $\mathscr{N} = 10^4$. We observe that for the two hydrophobic nanoparticle radii the effect is the same as long as the amount of hydrophobic interface in contact with water is the same. Hence, the concentration c necessary to observe the same effect is larger for the smaller hydrophobic nanoparticles, being the relevant factor the amount of hydrophobic interface. We discuss our results in terms of c and R.

In our simulations we update the variables σ_{ij} using the Wolff cluster algorithm [122]. The algorithm is based on an exact mapping of the model studied here to a percolation problem, following the mapping rules described in [43, 45]. The mapping is exact in this case because the system has no frustration. Bond indices within a water molecule belong to the same cluster with probability $p_{same} \equiv 1 - \exp[-\beta J_\sigma]$, where $\beta \equiv (k_B T)^{-1}$, k_B is the Boltzmann constant. Bond indices of nearest neighbors (n.n.) water molecules belong to the same cluster with probability $p_{facing} \equiv 1 - \exp[-\beta J']$, where $J' \equiv J - Pv_{\mathrm{HB}}$ is the HB enthalpy due to the interaction energy and the HB volume increase. For the interfacial water molecules, we consider J^h and J^h_σ instead of J and J_σ respectively. We study pressures in the interval 0.02 GPa $\leqslant P \leqslant$ 0.2 GPa and we present a detailed scaling analysis for pressures 0.12 GPa, 0.14 GPa, 0.16 GPa, and 0.18 GPa.

5.4 Results

We first considered how the confinement in fixed hydrophobic matrix affects the thermodynamics of liquid water above the melting point. In (Fig. 5.2) the $P-T$ phase diagram for different concentrations c of hydrophobic nanoparticles demonstrates a shift to lower T of the liquid-gas spinodal for $c > 0$. For $c = 25\%$ the T change from the $c = 0$ case is about 55 K at $P = 0.02$ GPa and about 35 K at $P = 0.14$ GPa. The shifts in the TMD for $c > 0$ with respect to the $c = 0$ case is reminiscent of results for other models of confined water [80, 128, 185]. We find stronger changes for increasing c. The changes are not monotonic with pressure. For instance, for $c = 25\%$ the TMD exhibits a shift to lower T of about 35 K at $P = 0.02$ GPa and 0.14 GPa, whereas, at $P = 0.19$ GPa the TMD increases of about 100 K with respect to the $c = 0$ case (Fig. 5.2).

Relevant properties are associated with the fluctuations of thermodynamic quantities. For example, the fluctuations of an order parameter associated with a phase transition exhibit characteristic behavior when the phase transition occurs. Hence, their calculation allows us to locate the phase boundaries. Moreover, from the fluctuations it is possible to calculate the measurable quantities such as the isothermal compressibility, the isobaric specific heat, or the isobaric expansion coefficient that characterize the macroscopic behavior of the system and are relevant in many technological applications. For example, from the calculations of the volume fluctuations $\langle(\delta V)^2\rangle \equiv \langle(V - \langle V\rangle)^2\rangle$ using the fluctuation-dissipation relation it is possible to calculate the isothermal compressibility, $K_T \equiv \langle(\delta V)^2\rangle/(k_B T\langle V\rangle)$ (Figure 5.3). From each data set at constant P, using separate

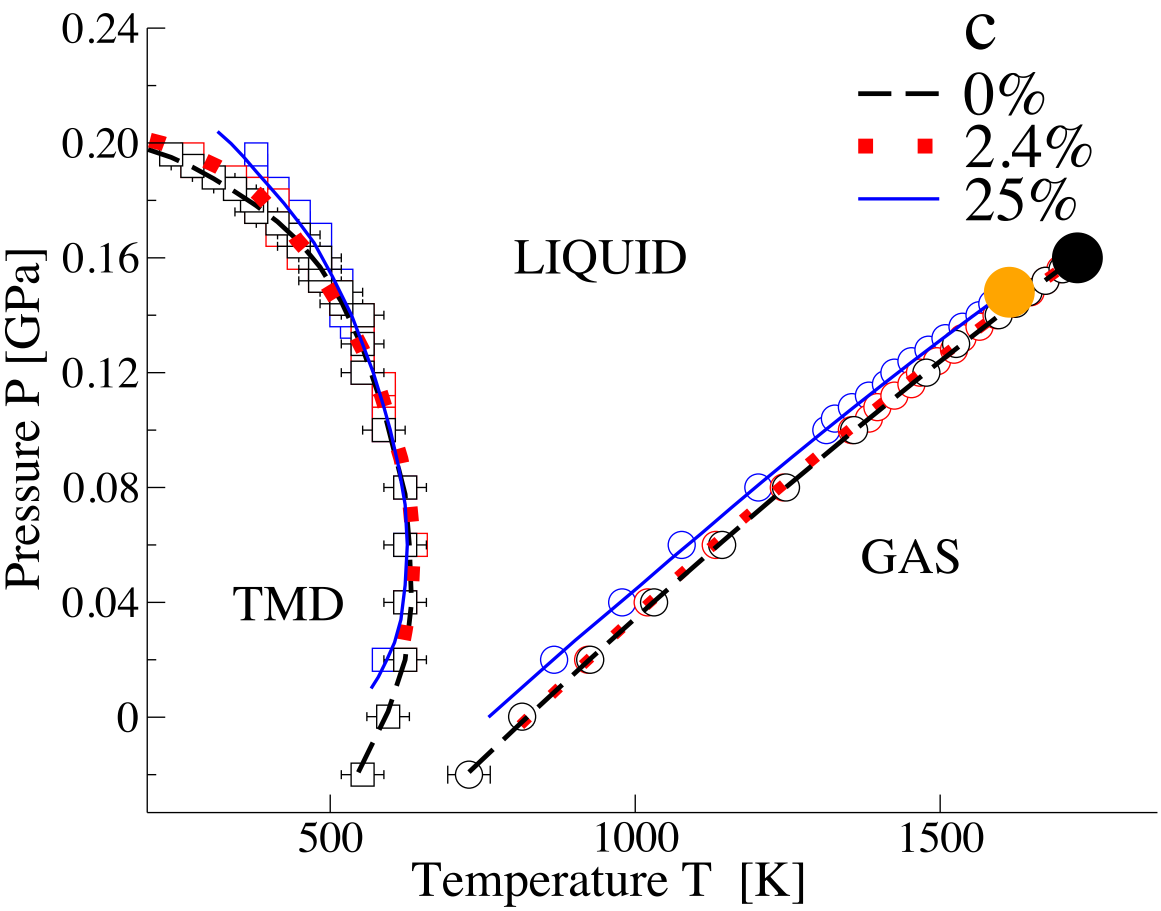

Figure 5.2: P–T phase diagram for different hydrophobic nanoparticle concentrations c. Open circles mark liquid-to-gas spinodal line, squares mark TMD line. In this and all other figures, where not shown, errors are smaller than the symbol size. Lines are guides for the eyes (dashed for $c = 0$, dotted for 2.4%, full for 25%). The liquid–gas critical point (large full circle) is the same, within the error bar, for $c = 0$ and 2.4%, while occurs at lower P and lower T for $c = 25\%$.

fits on each side of the set maxima, we extrapolate the maxima of compressibility $K_T^{\max}$, and the maxima in $\langle(\delta V)^2\rangle$.

By calculating the value of K_T for state points sampled in the $P-T$ plane for $T < 190$ K [Fig. 5.4(a)] we identify the location and shape of the locus of maxima of K_T. When a critical point occurs, the locus of $K_T^{\max}$ calculated in the supercritical region converges towards the locus of maxima of correlation length ξ (Widom line), as well as any other locus of maxima of response functions. This is because in the vicinity of a critical point all the response functions can be expressed as a power law of ξ. On the other hand, at a critical point, ξ diverges in the thermodynamic limit. Therefore, $K_T^{\max}$ and all the other response functions diverge at the critical point. Hence, by following the locus $K_T^{\max}(P)$ in the $P-T$ plane, when a critical point occurs we observe a diverging $K_T^{\max}$ in the thermodynamic limit. Moreover, because the critical point is at the end of a first-order phase transition in $P-T$ plane, maxima occur along this line and increase linearly with system size. Therefore, by locating the locus of $K_T^{\max}$ and calculating the finite size scaling of $K_T^{\max}$ at different pressures we are able to locate the critical point and the line of first-order phase transition.

We first extract the locus of maxima of K_T at different values of c and observe that its position does not depend on $\mathscr{N}$ [Fig. 5.4(a)] nor c [Fig. 5.4(b)]. We therefore conclude that the line of $K_T^{\max}$ is a robust feature of water upon confinement in a fixed disordered hydrophobic matrix of hydrophobic nanoparticles.

We find, however, that confinement drastically reduces volume fluctuations at low T. For a water monolayer with $\mathscr{N} = 1.6\times10^5$ cells confined within hydrophobic nanoparticles with $R = 1.6$ nm at $c = 25\%$, we find a maximum $K_T^{\max}$ along the isobar at $P \simeq 0.16$ GPa that is 99.7% smaller than the $c = 0$ case. If we decrease c to 2.4%, the reduction of $K_T^{\max}$ is still remarkable: 92.3% (Fig. 5.5).

For $c = 0$, previous investigations have located a liquid-liquid critical point at $T \simeq 174$ K and $P \simeq 0.13$ GPa by calculating the fluctuations of volume and entropy [Fig. 5.6(a)] [27, 32, 34, 36, 37, 39, 46, 101, 174, 175].

Note that for $c > 0$ the maxima of $\langle(\delta V)^2\rangle$ do not change monotonically with P or T (Fig. 5.7). Instead, the maxima of $\langle(\delta V)^2\rangle$ appear to diverge at two different values of T

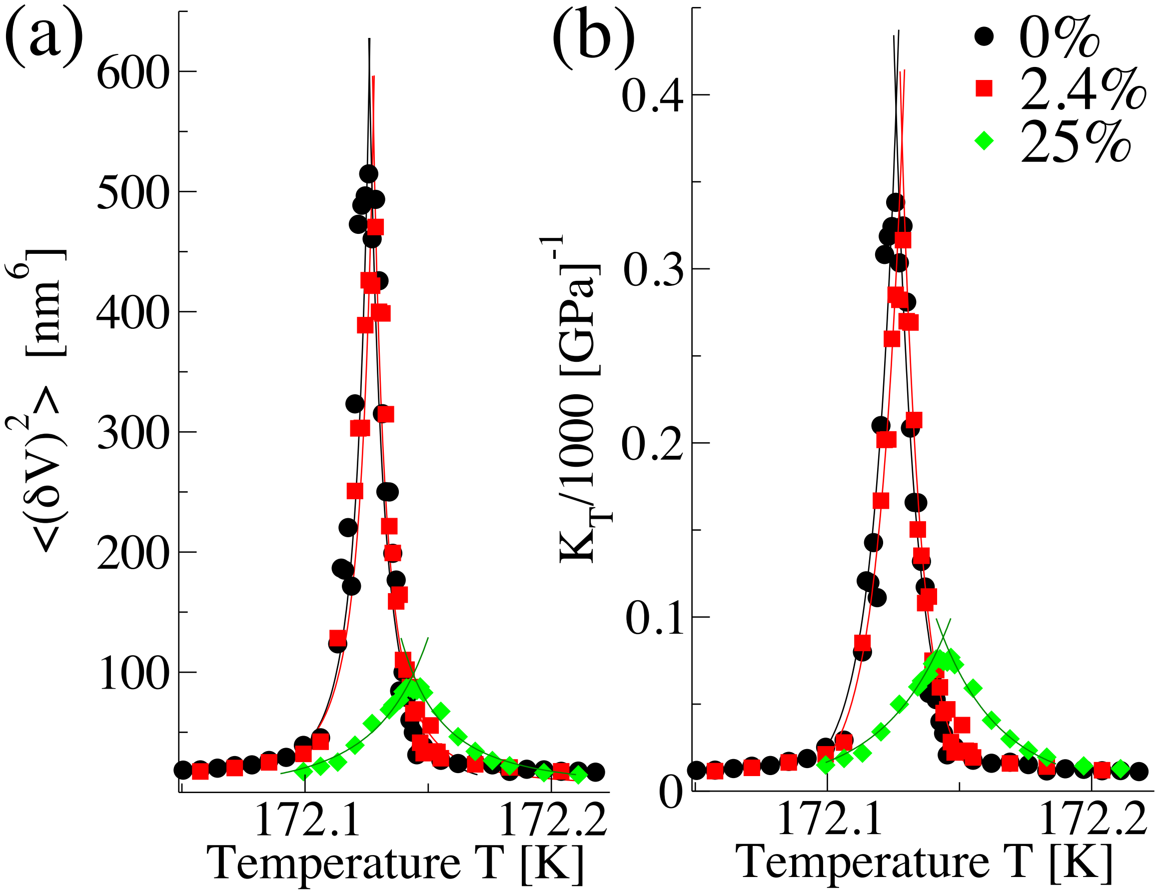

Figure 5.3: Decrease of volume fluctuations $\langle(\delta V)^2\rangle$ and isothermal compressibility K_T at $P = 0.14$ GPa for increasing hydrophobic nanoparticle concentrations c. Calculations based on a system with $\mathscr{N} = 4 \times 10^4$. Lines are fits of simulation data for $\langle(\delta V)^2\rangle$ (a) and K_T (b) with exponential function $y = a_0 e^{a_1/(a_2-x)}$ separately on each side of the maximum, excluding the points near the maximum. (We estimate the maximum of each dataset as the crossing of the fits on each side of the maximum, plus or minus the distance of the crossing point from the curve maximum.)

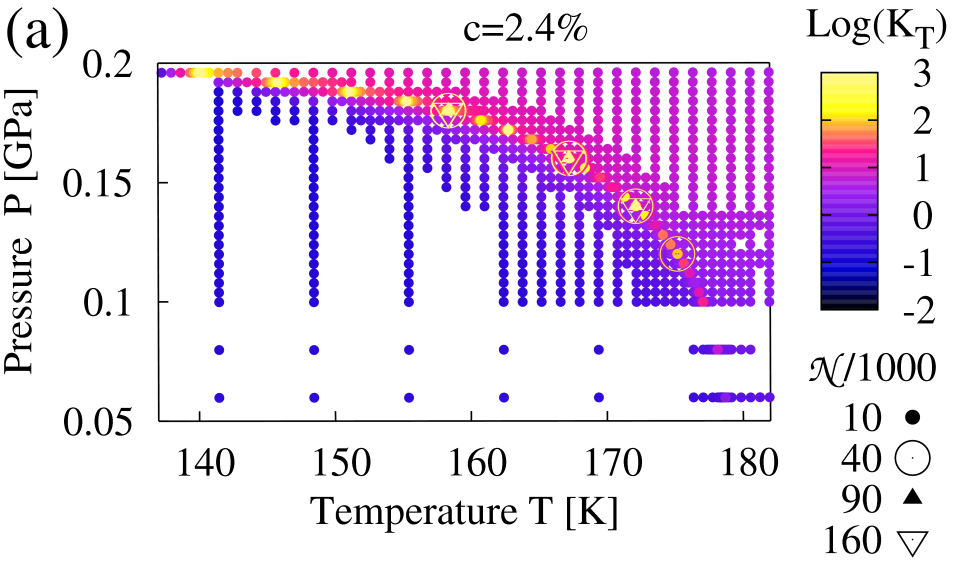

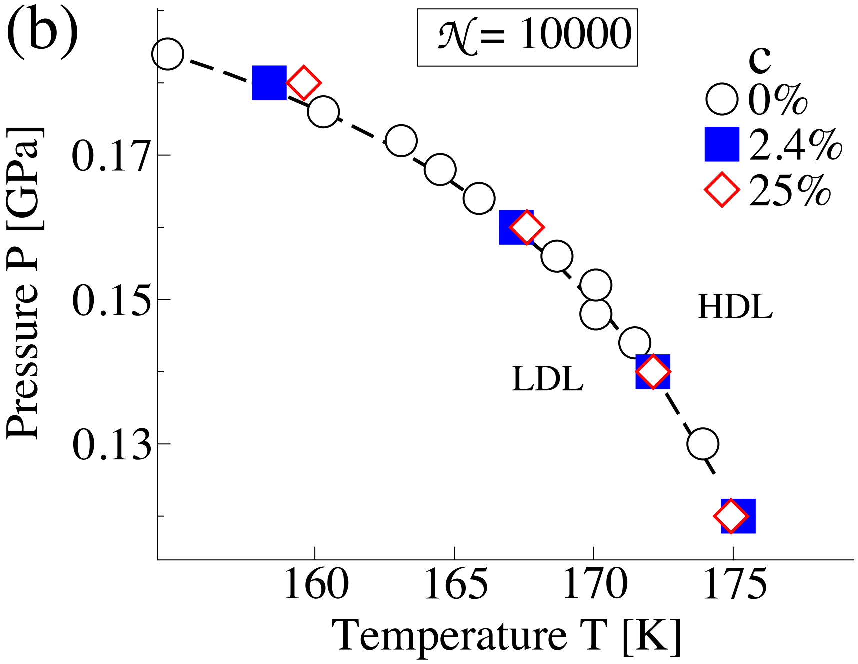

Figure 5.4: (a) The locus of maxima of $K_T(P,T)$ does not depend on $\mathscr{N}$, as shown by symbols for $\mathscr{N}$ going from 10^4 to 1.6×10^5, for hydrophobic nanoparticles with radius $R = 1.6$ nm and $c = 2.4\%$. Values of $\log K_T(P,T)$ are color-coded as shown in the panel. (b) The locus of maxima of $K_T(P,T)$ does not depend either on concentrations c, as shown for $\mathscr{N} = 10^4$ and $c = 0$, 2.4% and 25%.

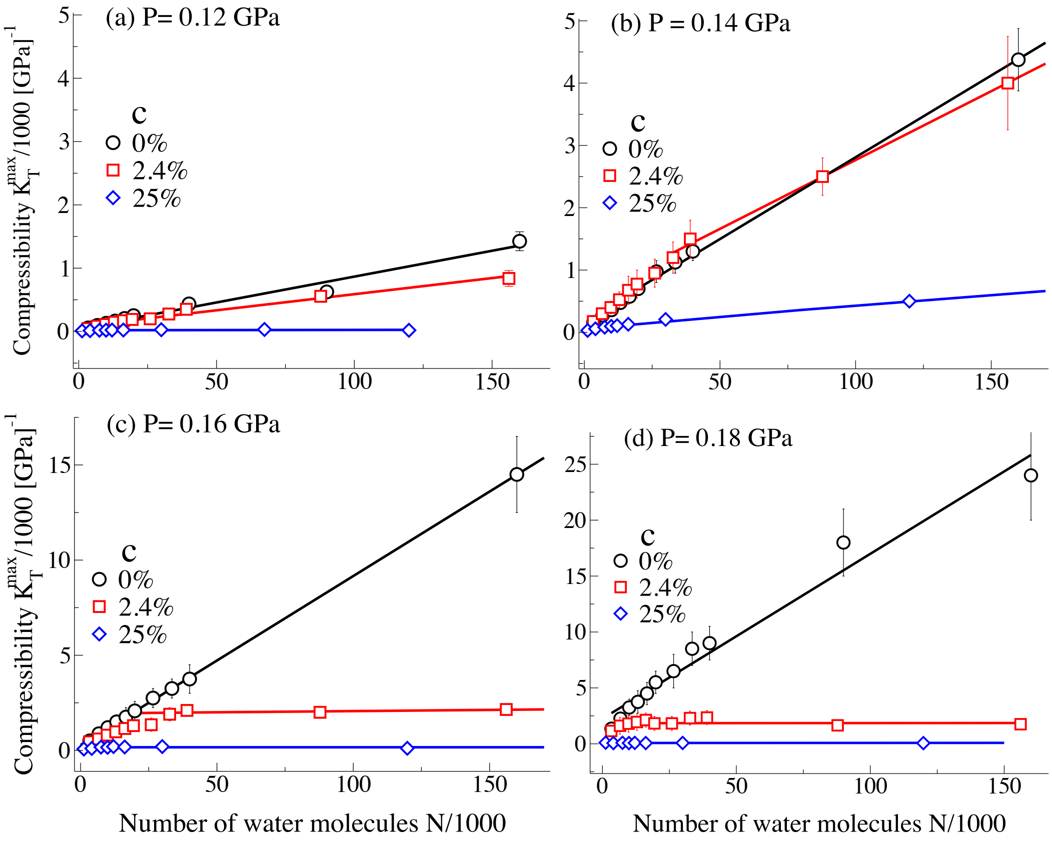

Figure 5.5: Dependence of the maxima $K_T^{\max}$ of the isothermal compressibility $K_T \equiv \langle(\delta V)^2\rangle/(k_B T\langle V\rangle)$ for $c = 0$, 2.4% and 25% on the number of water molecules N. (a) For $P = 0.12$ GPa, $K_T^{\max}$ slowly increases and possibly saturates. (b) For $P = 0.14$ GPa, the linear increase of $K_T^{\max}$ with N is consistent with a first-order LLPT for all c. For $P = 0.16$ GPa (c) and $P = 0.18$ GPa (d), $K_T^{\max}$ increases linearly only for $c = 0$ indicating a first-order LLPT, but saturates for $c = 2.4\%$ and 25%, consistent with the absence of a first-order LLPT [3].

---

[3] At $c = 0$, $K_T^{\max}$ increases for higher P because $\langle(\delta V)^2\rangle$ depends weakly on P, and $K_T^{\max}$ occurs at lower $T\langle V\rangle$.

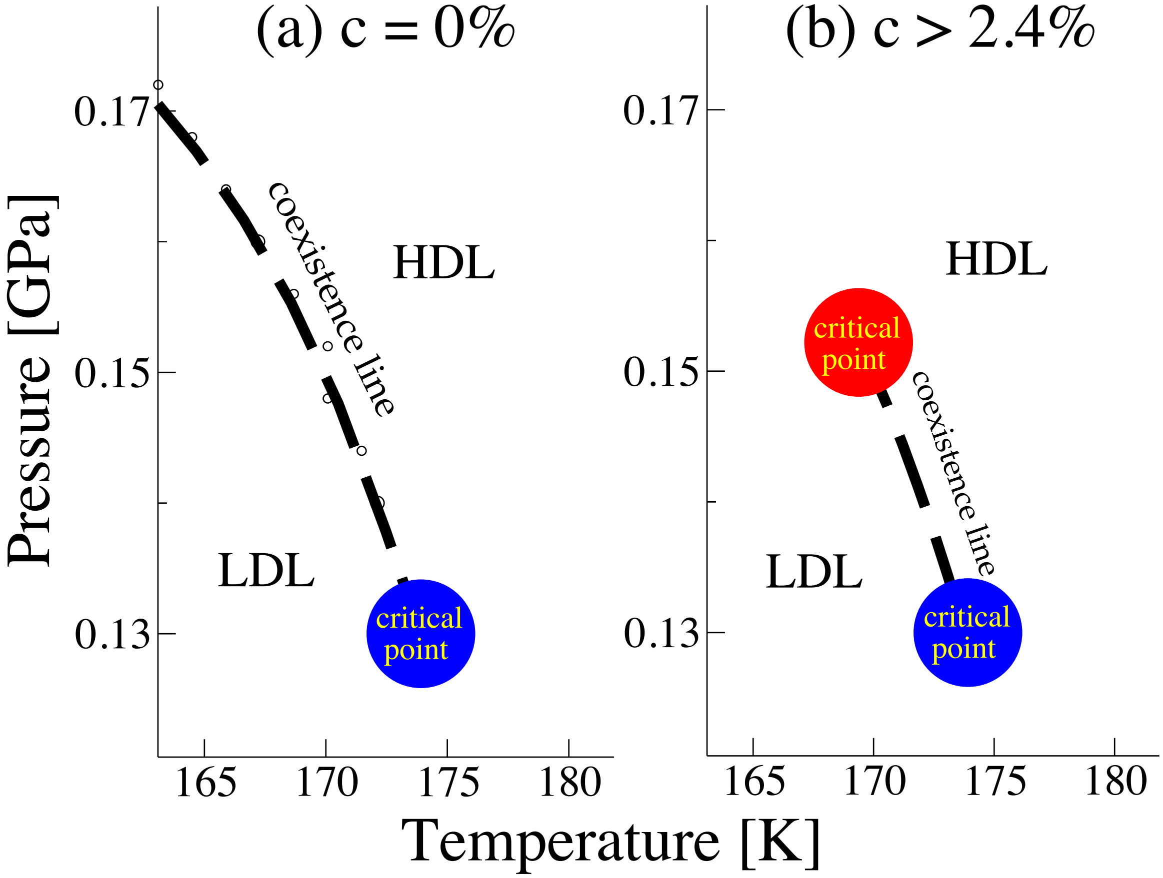

Figure 5.6: Enlarged view of the low-T region of the phase diagram. The first-order LLPT ends in a critical point at $T \simeq 174$ K and $P \simeq 0.13$ GPa for all c. In (a) for $c = 0$ the first-order LLPT is terminated by one critical point. For $c = 2.4\%$ and 25% (b) at $P > 0.15$ GPa the first-order LLPT is no longer detected, indicating a new high-P end point, whose behavior is consistent with a critical point (see text).

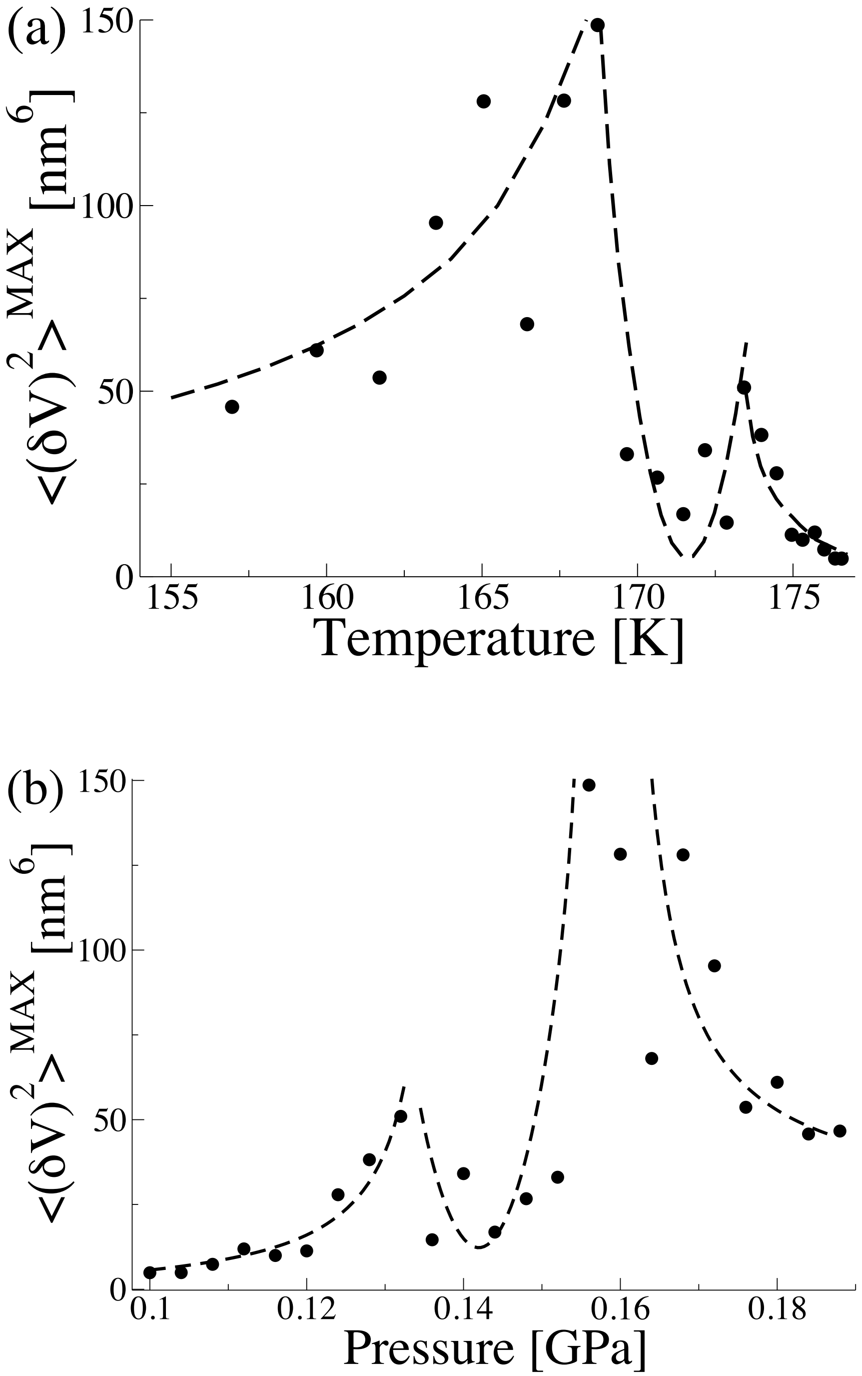

Figure 5.7: The maxima of $\langle(\delta V)^2\rangle$ for $c = 25\%$ and $\mathscr{N} = 10^4$. (a)$\langle(\delta V)^2\rangle^{\max}$ increase approaching $T = 168$ K and 174 K and (b) approaching $P = 0.132$ GPa and 0.156 GPa. Dashed lines are guides for the eyes.

and P. This behavior for $c > 0$ is consistent with the occurrence of another critical point at high P [Fig. 5.6(b)].

The general theory of finite size scaling tells us that, at a first-order phase transition, $K_T^{\max}$ increases linearly with the number of degrees of freedom, here equal to $4N$. We find a clear linear increase for 0.14 GPa$\leq P \leq 0.20$ GPa for $c = 0$, and only for 0.14 GPa$\leq P < 0.16$ GPa for $c = 25\%$ and 2.4%, consistent with the absence of a first-order LLPT outside these ranges (Fig. 5.5).

To emphasize that, at low P, $K_T^{\max}$ does not grow linearly with N, we consider the $\chi \equiv \log(K_T^{\max} \times 1\ \mathrm{GPa}/N)$ as a function of $1/N$, where $K_T^{\max} \times 1\ \mathrm{GPa}/N$ is dimensionless (Fig. 5.8).

For a first-order LLPT χ tends to a constant as $1/N \to 0$, otherwise it vanishes. Our calculations confirm that a first-order LLPT is absent for any c at sufficiently low P. For $c = 2.4\%$ and $c = 25\%$ the first-order LLPT is absent also at sufficiently high P. Hence there is an upper critical point at the end of the LLPT line for $c = 2.4\%$ and $c = 25\%$.

To more precisely locate the end points of the first order LLPT, we study the finite size scaling of the Binder cumulant for volume [152, 194]

$$U_{\mathscr{N}} \equiv 1 - \frac{\langle V^4 \rangle_{\mathscr{N}}}{3\langle V^2 \rangle_{\mathscr{N}}^2}, \tag{5.5}$$

where $\langle \cdot \rangle_{\mathscr{N}}$ is the thermodynamic average for a system with $\mathscr{N}$ cells. For $\mathscr{N} \to \infty$, at fixed c and P, $U_{\mathscr{N}} = 2/3$ for any T away from a first-order phase transition, while $U_{\mathscr{N}}^{\min} < 2/3$ at a first-order phase transition [152, 194].

The T dependence of $U_{\mathscr{N}}^{\min}$ is shown in Figs. 5.9(a) and 5.9(b) for $c = 0$ at two representative values of P and for different system sizes. We find that there is a temperature at which $U_{\mathscr{N}}^{\min} < 2/3$ with increasing $\mathscr{N}$ for $P \geqslant 0.14$ GPa indicating the presence of a first order LLPT in this region. The Binder cumulant analysis therefore confirms what we concluded from the behavior of $K_T^{\max}$, i.e., the existence of a first-order LLPT in the range 0.14 GPa $\leqslant P \leqslant 0.2$ GPa for $c = 0$. However, for $c = 2.4\%$ and 25%, we find that with increasing $\mathscr{N}$ there is a T at which $U_{\mathscr{N}}^{\min} < 2/3$ for $P = 0.14$ GPa, but not for $P \geqslant 0.18$ GPa [Fig. 5.9(c)–(f)], which implies that in the thermodynamic limit at $P = 0.18$ GPa the system is in the one phase region at all the temperatures considered

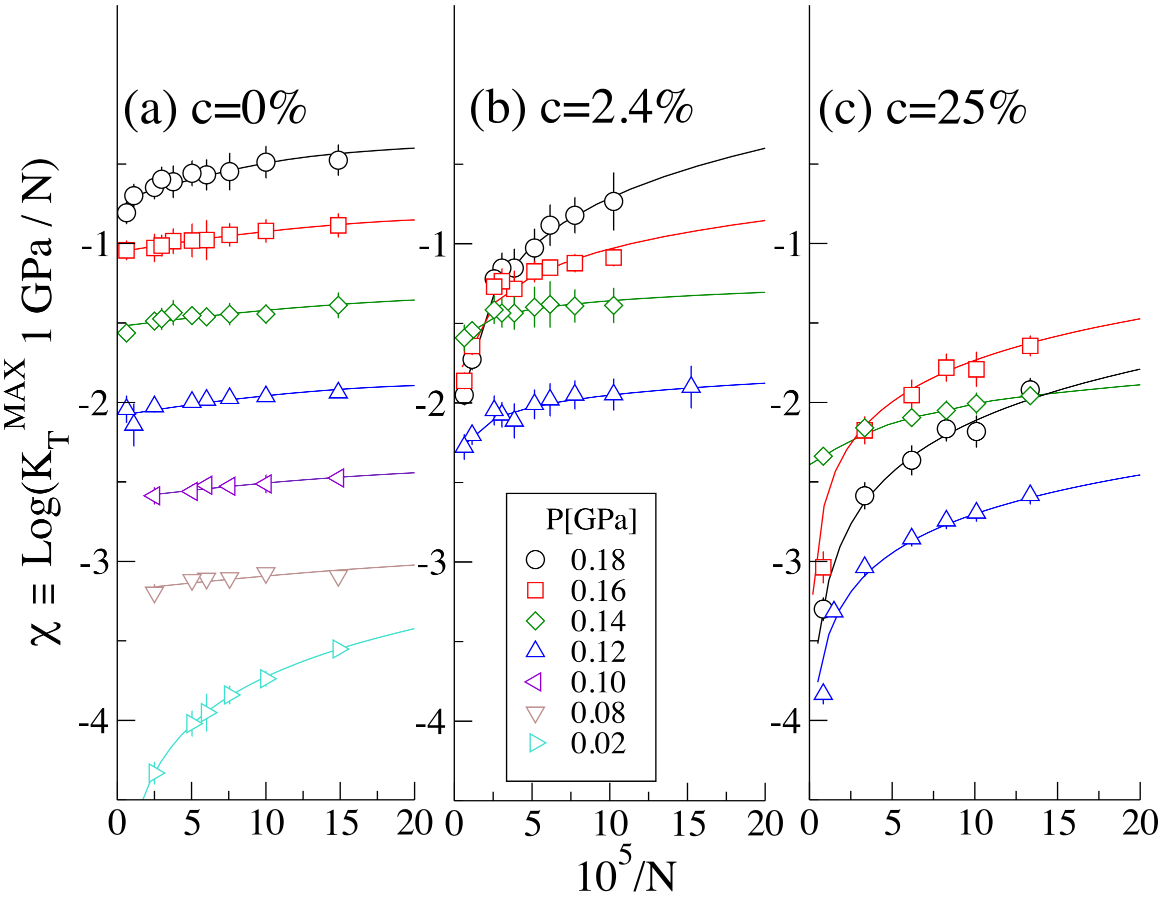

Figure 5.8: Size dependence of compressibility maxima $K_T^{\max}$ for several pressures and (a) $c = 0$, (b) $c = 2.4\%$, (c) $c = 25\%$. The dimensionless quantity $\chi \equiv Log(K_T^{\max} \times 1\ \mathrm{GPa}/N)$ has a clear decrease for $c = 0$ only for very low P, indicating the absence of a first-order LLPT. At fixed P, by increasing c, the value of $K_T^{\max}/N$ decreases of orders of magnitude. For $c = 25\%$ the values of χ are not monotonic with P, with maxima at $P = 0.16$ GPa, showing that the upper end-point for $c = 25\%$ is between $P = 0.16$ GPa and $P = 0.14$ GPa.

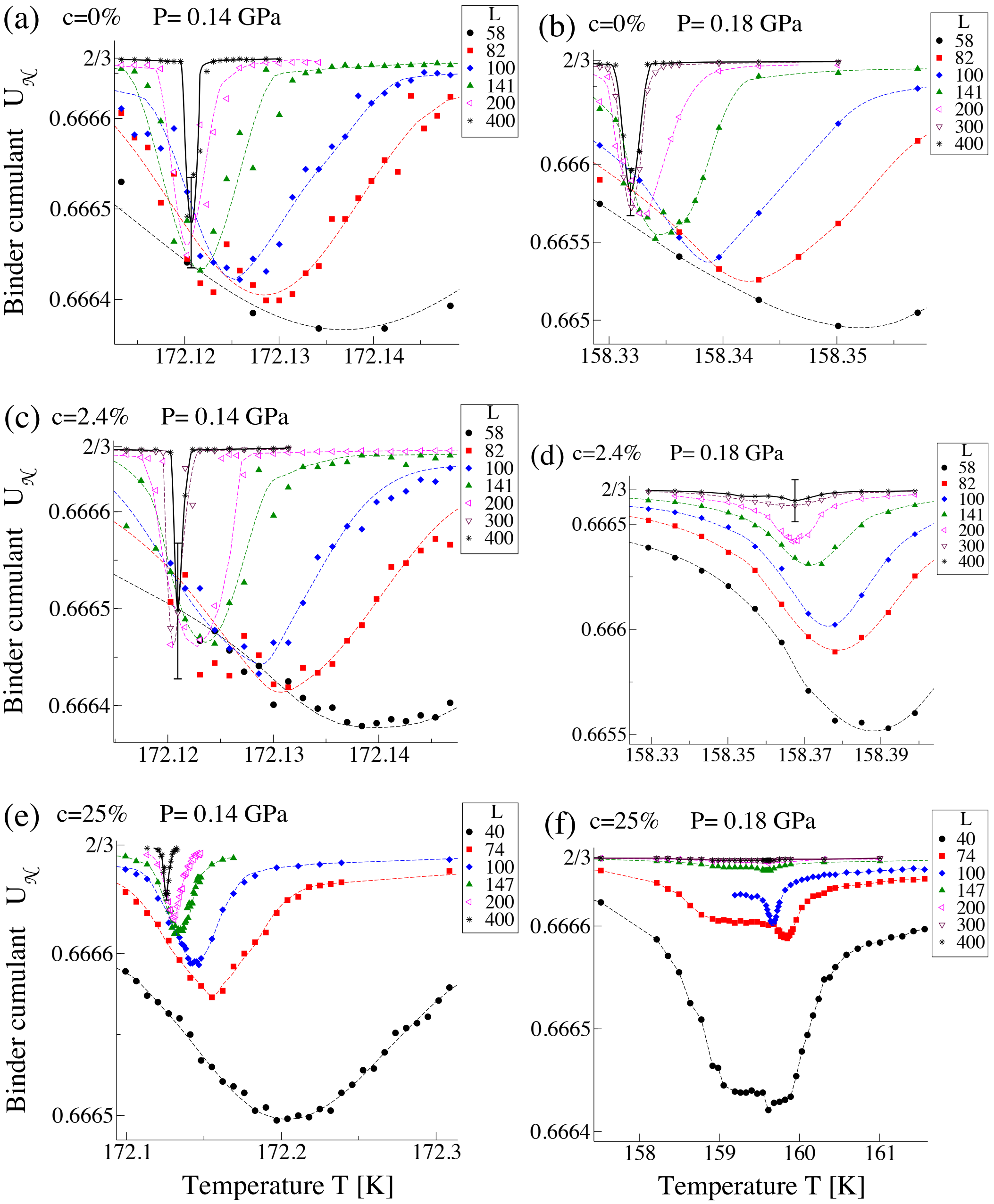

Figure 5.9: Finite size scaling of the isobaric Binder cumulant $U_{\mathcal{N}}$ as a function of temperature, for different values of hydrophobic nanoparticle concentrations c. Sizes range from $\mathcal{N} = L^2 = 1600$ to 1.6×10^5. (a) For $c = 0$ at pressure $P = 0.14$ GPa and (b) 0.18 GPa; (c) for $c = 2.4\%$ at $P = 0.14$ GPa and (d) 0.18 GPa; (e) for $c = 25\%$ at $P = 0.14$ GPa and (f) 0.18 GPa. The error bars are estimated using the Jackknife method for all the points, but only the largest error bars—at the minima of the largest system sizes—are shown for clarity reasons.

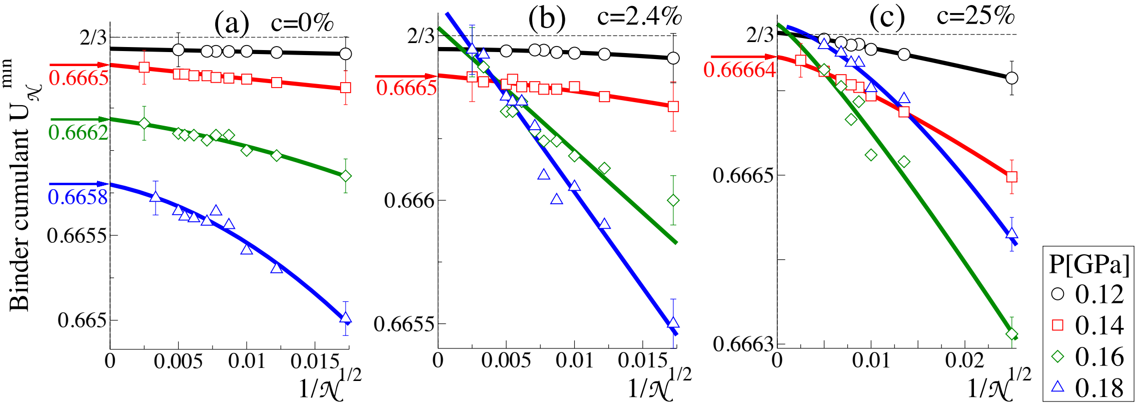

Figure 5.10: Extrapolation of the minima of Binder cumulants $U_{\mathcal{N}}^{\min}$ to the thermodynamic limit $\mathcal{N} \to \infty$. For $P = 0.12$ GPa, $U_{\mathcal{N}}^{\min} \to 2/3$ as $\mathcal{N} \to \infty$ within the error bars. For $c = 0\%$ in (a) $U_{\mathcal{N}}^{\min} \leqslant 2/3$ for $P \geqslant 0.14$ GPa, indicating a first-order LLPT for these pressures. For hydrophobic nanoparticle concentrations of $c = 2.4\%$ (b), and $c = 25\%$ (c), $U_{\mathcal{N}}^{\min} \leqslant 2/3$ for $\mathcal{N} \to \infty$ only for $P = 0.14$ GPa marked by the arrow Therefore, the LLPT is washed out by the hydrophobic confinement at high P. For sake of clarity, typical error bars are shown only for a few points. Lines through the points are polynomial fits.

here. These results are summarized for several pressures in Figure 5.10, where we show the size dependence of the minima of the Binder cumulant at different P for the three concentrations studied. For $c = 2.4\%$ and 25% we find that $U_{\mathcal{N}}^{\min}$ tends to a value less than 2/3, consistent with a first-order LLPT only for P at about 0.14 GPa. Therefore, consistent with what already has been indicated by the analysis of $K_T^{\max}$ and $\langle(\delta V)^2\rangle$ (Fig. 5.5 and Fig. 5.7) for $c = 2.4\%$ and 25%, the first-order LLPT occurs only in a limited range of pressures around 0.14 GPa, with two end-points: one at ≈ 0.15 GPa, and the other at ≈ 0.13 GPa [Fig. 5.6(b)].

5.5 Discussion

We adopt density as the relevant order parameter for the liquid-liquid phase transition. In the model the density depends on the number of accessible configurations (entropy) and energy of the system via the number of HBs N_{HB}, and their specific volume v_{HB}. Therfore, our order parameter includes by definition contributions coming from entropy and energy, as is in general the case for fluid-fluid phase transitions [195].

It is interesting to compare our results with other cases in which the effect of quenched disorder on phase transitions in 2D has been considered, including membranes [196–198] or quenched filler particles [199]. In particular, we are interested in the comparison with the case of random-field (RF) quenched disorder. In the RF case, phase transitions are always destroyed in two dimensions [200–202]. To clarify what type of quenched disorder do the hydrophobic nanoparticles represent in the case considered here, we observe the following. For RF quenched disorder two conditions must hold: (i) the RF couples with the order parameter and (ii) the RF destroys the ground state by frustrating it. While in our model the first condition (i) holds, the second one (ii) does not, as we discuss in the following. Hence, our system cannot be modeled as a RF.

The RF destroys the ground state, because it forces locally the degrees of freedom to assume states that are not consistent with the ground state. In other words, the RF forces the creation of interfaces. This is not true in our model, where the ground state is not modified by the presence of the hydrophobic nanoparticles. By starting from a completely ordered configuration (one of the q ground states), we heat up the sample and observe that the stronger water-water hydrogen bond (HB) interactions near the hydrophobic nanoparticles make the ground state as stable as the case without the hydrophobic nanoparticles, as shown in Fig.5.4, where the locus of maxima of $K_T(P,T)$ does not depend on concentration c.

We understand our results in terms of dilution quenched disorder, for which the disorder effects are mild and do not destroy phase transitions in 2D. In particular, by including hydrophobic nanoparticles, we delete water-water interactions in the region occupied by the hydrophobic nanoparticles and make the water-water interaction stronger for the first shell of water molecules hydrating the hydrophobic nanoparticles. The procedure reminds us of the one performed in the Kasteleyn-Fortuin dilution that, as can be analytically demonstrated [45], does not change the thermodynamics of the Ising model or any Potts model. Thus we believe that our model cannot be described as a RF model and the results for RF models do not apply to our case.

However, in our case, at high P the phase diagram changes. We believe that this effect could be a consequence of the fact that we do not follow the rules of Kasteleyn-Fortuin dilution, the only that does not change the thermodynamics [43]. This consideration is supported by mean field results for the model with no hydrophobic nanoparticles [36]. It has been shown [36] that the low-T state is disordered around the locus $P_{LL} \simeq ((J + 3J_\sigma)/v_{\rm HB}) + \gamma T_{LL}$, where T_{LL} and P_{LL} are the T and P along the liquid–liquid transition line and $\gamma \simeq -7.4k_B/v_0$. The disordering is continuous at low P and discontinuous at high P with a critical point (P_C, T_C), separating the low-P and high-P region, given by

$$T_C \simeq (4/3)J_\sigma/\epsilon \tag{5.6}$$

and

$$P_C \simeq ((J + 3J_\sigma)/v_{\rm HB}) + \gamma T_C. \tag{5.7}$$

With the hydrophobic nanoparticles, we introduce new energy scales $J^h = 1.3J$ and $J^h_\sigma = 1.3J_\sigma$ with stronger HBs. We now expect that at high enough $P'_{LL} \simeq ((J^h + 3J^h_\sigma)/v_{\rm HB}) + \gamma T'_{LL} = P_{LL} + 0.3(J + J_\sigma)/v_{\rm HB} > P_C + 0.3(J + J_\sigma)/v_{\rm HB} > P_C$, with $T'_{LL} \simeq (J^h + 3J^h_\sigma - P'_{LL}v_{\rm HB})/(-\gamma) = T_{LL} - 0.3(J + J_\sigma)/(-\gamma) < T_C - 0.3(J + J_\sigma)/(-\gamma) < T_C$, both stronger HBs and normal HBs are weakened enough by the effect of P. The random distribution of distances between hydrophobic nanoparticles makes the disordering process continuous at $P > P'_{LL}$ and $T < T'_{LL}$. This interpretation seems to be qualitatively consistent with our numerical results.

It is also important to note that we choose not to perform averages over the randomness because our results show that the system is self-averaging for increasing size. Indeed, we change the random configuration of hydrophobic nanoparticles for each size that we consider and we find that the results converge to a limit for increasing size, as shown in Fig. 5.8, 5.9, 5.10. Therefore, since the system is self-averaging, averages over randomness are not going to change our results.

The relation of this model in 2D with bulk 3D water is established by the mean-field results for the model [36]. Mean-field applies to systems embedded in a space with large or infinite dimensions. It was shown that, apart from quantitative differences with simulations in 2D, mean-field results and 2D results agree qualitatively. This agreement is strong evidence that embedding dimension does not play a role in the qualitative predictions of the model. Furthermore, comparison of the phase diagram of the 2D model simulations with the results from 3D models do not show qualitative differences and, for several properties not even quantitative differences, as discussed in [175].

We finally discuss here the effect of the increased HB strength for water-water interactions at the surface of the hydrophobic nanoparticles. The value $J^h = 1.3J$ is chosen to facilitate the comparison with previous results from other models [151]. However, our preliminary results for $J^h = 1.05J$ and $c = 25\%$ do not show qualitative differences with the case with $J^h = 1.3J$ and the same concentration of hydrophobic nanoparticles (Fig.5.11).

5.6 Conclusion

As a consequence of the restructuring effect of hydrophobic nanoparticles on the hydration shell water, stronger HBs are formed in the hydration shell of each solute. At low T the hydration water is more ordered with respect to the $c = 0$ case. However, hydration shells around different hydrophobic nanoparticles have a high probability ($5/6 \simeq 83\%$) of being in a different local bonding order. Consequently, different ordered domains are generated in the vicinity of hydrophobic nanoparticles, reminiscent of the locally structured regions proposed in Ref. [146]. These competing domains disrupt the macroscopic order (Fig. 5.12). Due to the presence of many domain boundaries there is a large decrease in the fluctuations and response functions, such as K_T. In contrast, when no hydrophobic nanoparticles are introduced into the system ($c = 0$), a small temperature increase leads to a rapid change from the ordered to a disordered configuration as expected for a first order phase transition (Fig.5.13). This drastic change is the origin of the large fluctuations in K_T observed when approaching the discontinuous transition (Fig.5.5).

Our results for $c = 25\%$ and 2.4% (Fig. 5.14) show that the smaller the c, the larger the N at which the behavior deviates from the case $c = 0\%$. This observation suggests that the decrease of the fluctuations is due to the introduction of a characteristic length scale, inversely proportional to c, that limits the growth of the ordered structured regions. This is consistent also with a visual inspection of the typical configuration at different values of c (Figs. 5.12, 5.13, and 5.14).

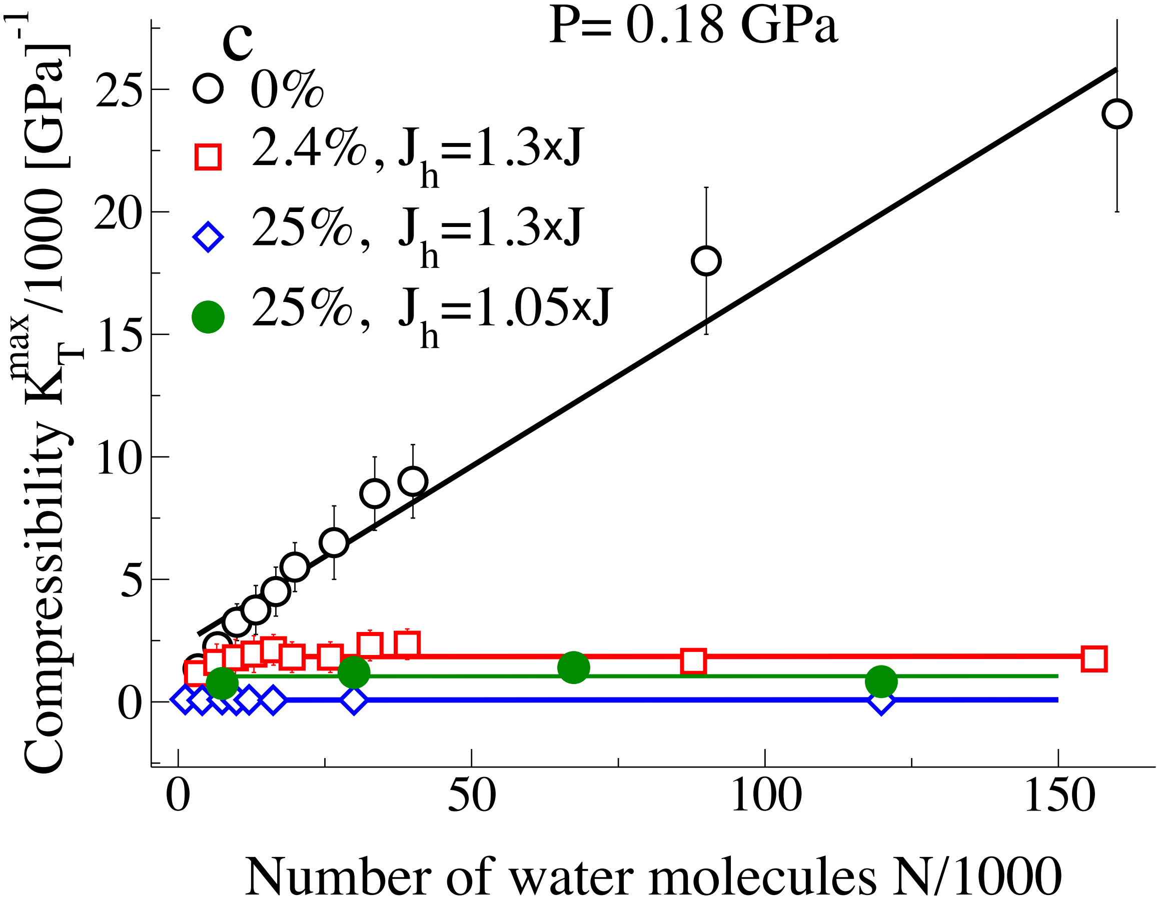

Figure 5.11: Dependence of the isothermal compressibility maxima $K_T^{\max}$ on the number of water molecules N at pressure $P = 0.18$ GPa for simulations of the model with $J^h = 1.3J$ for $c = 0$, 2.4% and 25% (open symbols), as in Fig.5.5, and for the model with $J^h = 1.05J$ for $c = 25\%$ (filled circles). We observe quantitative, but not qualitative, differences between the two cases with same $c = 25\%$ and different J^h.

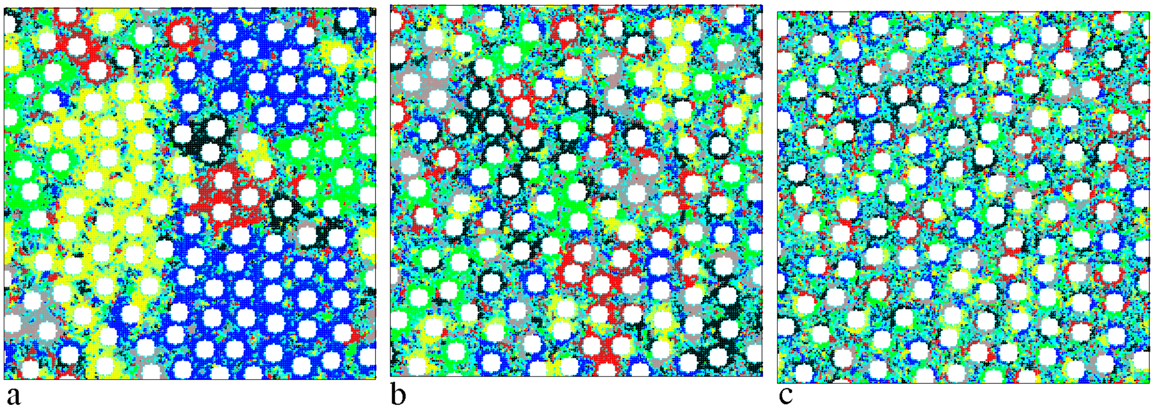

Figure 5.12: Typical configurations for $c = 25\%$ and $P = 0.18$ GPa for (a) $T = 159.58$ K, (b) 160.31 K and 162.40 K. Different colors represent different ordered domains of HBs. Water molecules with fewer than four HBs are represented in turquoise and hydrophobic nanoparticles in white. HB ordering is favored around hydrophobic nanoparticles, but the system is macroscopically disordered. Note that domain boundaries can cross the hydrophobic nanoparticles.

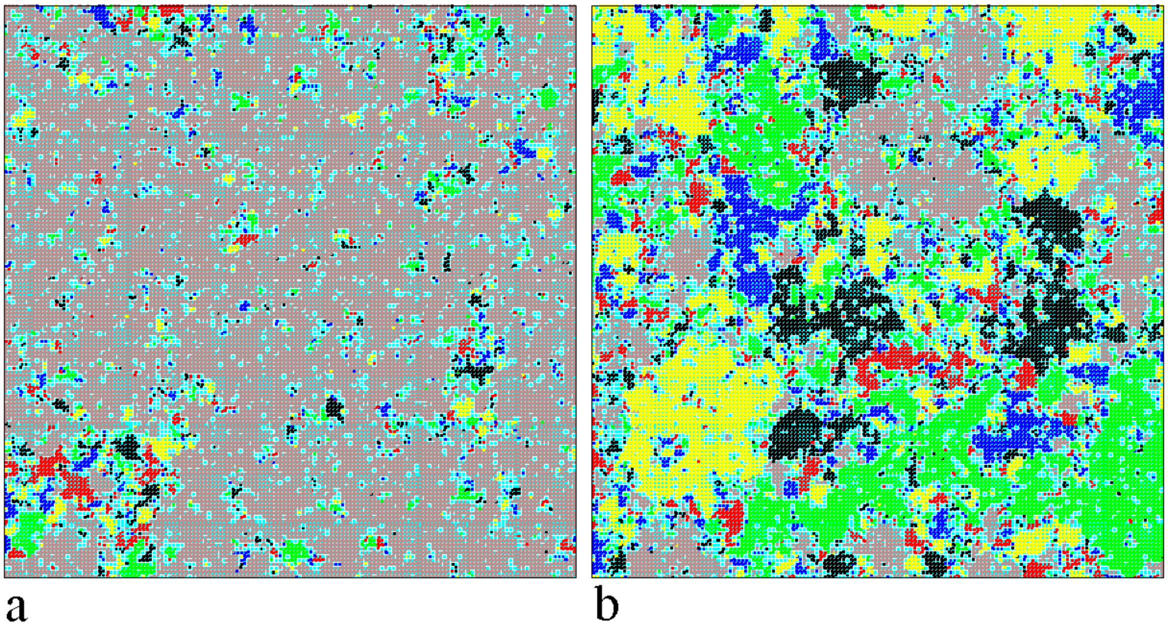

Figure 5.13: For $c = 0$ a small temperature increase from (a) $T = 158.332$ K to (b) 158.333 K leads to a sudden change from the ordered (a) to a disordered configuration (b). Such behavior is consistent with a first order phase transition.

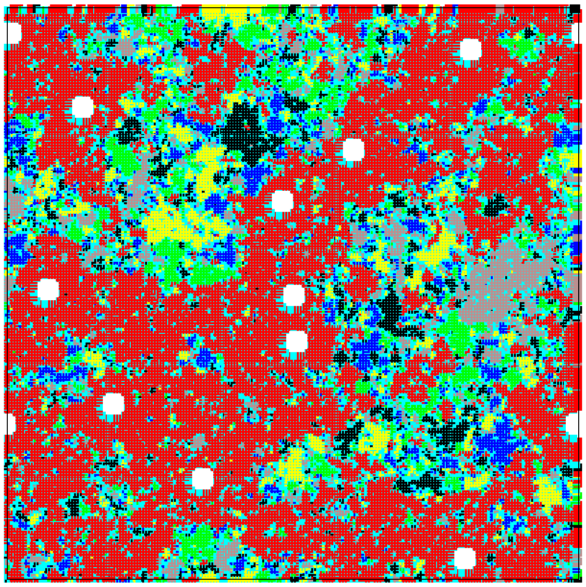

Figure 5.14: Configuration for $c = 2.4\%$ for $T = 158.36$ K. The hydrophobic nanoparticles contribute to the continuous growth of the ordered domains, here the largest ordered domain is visualized in red.

Note that the reduction of compressibility was previously observed in the theoretical analysis of water confined by a fixed matrix of randomly distributed Lennard-Jones disks. However this reduction only occurred when the hydrophobic obstacle concentrations were high [145]. We instead find here that K_T is reduced for c as low as 2.4%. More systematic studies are needed to understand how this difference among theoretical predictions depends on the details of the hydrophobic nanoparticle-water interaction energy. For example, we have shown here that a 30% increase in the HB strength in the water first hydration shell is enough to decrease the compressibility by 90% even for small c.

Our results are qualitatively consistent with recent experiments on H_2O confined in the hydrophobic mesoporous material CMK-1-14 consisting of micrometer-sized grains, each with a 3-dimensional interconnected bicontinuous pore structure, with an average pore diameter 14 Å, at a hydration level of 99% at ambient pressure [150, 153]. Zhang et al. find a broadening of the α_P peak, spanning from 240 K to 180 K in mesoporous CMK in contrast to the sharp peak at 230 K in hydrophilic confinement in silica mesopores MCM [150, 153], reminiscent of our results on the reduction of the response functions with respect to the $c = 0$ case. In addition, Zhang et al. demonstrate the TMD downshift by 17 K in hydrophobic CMK with respect to the hydrophilic MCM, which is similar to our observed temperature downshift of TMD for low pressures.

Recent results for small angle x-ray scattering for aqueous solutions of amphiphilic tetraalkyl-ammonium at ambient conditions suggest that the strengthening of the structure of hydration water is present only for solutes with radius smaller than ≈ 0.44 nm [215]. We therefore repeat our analysis for small hydrophobic nanoparticles with $R = 0.4$ nm, and find that our results are robust if the amount of hydrophobic interface in contact with water is kept constant with respect to the case of $R = 1.6$ nm. We conclude that the observed thermodynamic shifts and reductions of the response functions are due to the water-hydrophobic nanoparticle interactions. In particular, they are directly related to the strength of the HBs in the hydration shell. As a consequence, by keeping a constant amount of the water molecules in a direct contact with the hydrophobic nanoparticles, we reproduce consistent shifts in spinodal, TMD, and high-P, and the disappearance of the LLPT for both $R = 1.6$ nm and 0.4 nm hydrophobic nanoparticles.

It was previously shown for $c = 0$ that the dynamics of the Wolff cluster algorithm are very efficient and allow the system to fully equilibrate even in a low temperature region [122]. The dynamics of the $c > 0$ systems are still under detailed investigation. However, our preliminary results demonstrate that introducing a hydrophobic confinement with restructuring effect does not slow down the equilibration process. At the present time more detailed study of the correlation times is needed.

In conclusion, we predict that a water monolayer confined in a hydrophobic fixed matrix of hydrophobic nanoparticles at concentration c displays significant changes in the thermodynamics and important reductions in the response functions with respect to the $c = 0$ case. Moreover, at c as small as 2.4% a first-order LLPT at high P is no longer detected. As a consequence, even a small number of hydrophobic nanoparticles can make the detection of the LLPT difficult. These findings may have important applications in fields related to conservation at cryogenic temperatures (around -100^o C), for example, in the preservation of stem cells, blood, or food products.

Chapter 6

Effect of hydrophobic environments on the hypothesized liquid-liquid critical point of water

We often think of water as a typical liquid because of its ubiquity in our lives. However, the thermodynamic behavior of water is very complex and anomalous when compared to simple liquids [25, 203]. Its isothermal compressibility, isobaric specific heat, and coefficient of thermal expansion, in fact, show a non-monotonic behavior, displaying an apparent divergence in the supercooled region [186, 204]. Moreover, water presents a density anomaly, i.e., a decrease in density upon isobaric cooling [205]. The border of the region of density anomaly is marked by the temperature of maximum density (TMD) line.

To explain the anomalous behavior of water, in 1992 the *liquid–liquid critical point scenario* was hypothesized for supercooled water [66]. Since then, several computer simulations have modeled a singular behavior for supercooled water, i.e, the appearance of a liquid–liquid critical point (LLCP) at the end of a liquid–liquid phase transition (LLPT) line between two types of liquid water, high-density liquid (HDL) and low-density liquid (LDL) [39, 141, 142, 171, 176, 206–208].

The experimental study of water in the supercooled region, where its anomalies are more pronounced, is extremely difficult due the homogeneous nucleation of the crystal phase, occurring at $T = 235$ K at ambient pressure [25]. One way to explore this experimentally unaccessible region is to nanoconfine water, which forces it to remain in the liquid phase at temperatures where bulk water freezes, and a number of recent studies of the behavior of supercooled water have utilized various confining geometries, such as slits, pores or porous media [80, 101, 128, 129, 138, 139, 157, 162–168, 185].

The study of confined water at low temperatures is relevant to a wide range of fields, including food refrigeration and the cryopreservation of, e.g., stem cells, umbilical cord blood, and embryos. In both refrigeration and cryopreservation, extracellular or intracellular ice formation, dehydration, and solute concentration due to ice crystal growth can permanently damage cells but, under the proper conditions, this destructive phenomenon can be inhibited through the use of confinement techniques [28, 81, 89, 134, 209].

Another way to extend the accessible region in supercooled water is to investigate aqueous solutions, because the homogeneous nucleation temperature of water often decreases in temperature when solutes are added [210]. Several recent studies have explored supercooled water in aqueous solutions of hydrophilic [183, 211–217] and hydrophobic solutes [218, 219]. The properties of supercooled aqueous solutions are relevant to many biological and geophysical systems and, in particular, are of great interest when cryopreserving biological tissues [220].

Of particular interest is the behavior of water in contact with apolar surfaces or with apolar solutes. The study of water in these hydrophobic environments helps us understand such diverse phenomena as biological membrane formation, surfactant micellization, the folding of globular proteins, and the stability of mesoscopic assemblies [70, 130, 221]. Thus, understanding how hydrophobic interfaces and solutes affect the thermodynamics of supercooled liquid water also helps us understand the biology and biophysics of life under subfreezing conditions. In such studies, the crucial question to ask is how water in the hydrophobic environment differs from bulk water. One way to approach this fundamental question is to perform computer simulations. Recent simplified models, such as 2D square lattice models or 3D spherically symmetric potentials with two length scales, have captured the anomalous behavior of water, including the appearance of a LLPT ending in a LLCP [36, 100, 222, 223].

In this paper, we review how hydrophobic particles affect the thermodynamic behavior of supercooled liquid water. In particular, we discuss and compare the results obtained for hydrophobic objects in a 2D square lattice model for water, studied using Monte Carlo (MC) simulations [129] and the results obtained for mixtures of hard spheres (HS) and Jagla ramp potential particles studied using discrete molecular dynamics (DMD) simulations [218]. These results are then compared to previous observations for water in hydrophobic environments at subfreezing temperatures [80, 101, 128, 145, 150, 219].

The paper is organized as follows. Section 2 outlines the details of the models used in our computer simulations [129, 218]. Section 3 reviews the recent findings reported in these computational studies. The results are compared to previous reports for supercooled water in hydrophobic environments in Section 4. Conclusions are discussed in Section 5.

6.1 Models and Simulation Details

6.1.1 MC simulations of a coarse-grained model of water confined in a matrix of hydrophobic particles

The MC method is a computational tool that allows us to simulate the random thermal fluctuations of a system by sampling its different states at equilibrium. Different algorithms have been developed to optimize the MC simulation of spin models and cell models [43, 153]. The Wolff cluster algorithm [33] has become a particularly useful tool for the simulation of water when coarse-grained or cell models are utilized [36, 46, 122, 224].

Here we review MC simulations performed in the NPT ensemble on a water monolayer between two hydrophobic extended flat surfaces separated by about 0.7 nm, partitioned into $\mathscr{N}$ cells, each with four nearest neighbors (n.n.). Each cell is occupied either by a water molecule or a hydrophobic nanoparticle whose size is controlled by the number of cells it occupies. The nanoparticles have an approximately spherical shape and are randomly distributed to form a fixed matrix that mimics a porous system or a rough atomic interface. Each water cell has four bond indices with q orientations that determine whether a hydrogen bond (HB) can be formed between the n.n. We choose q possible orientational states based on the assumption that the HB breaks when its angle deviation exceeds ±30°, therefore $q = 360/60 = 6$. The model incorporates isotropic interactions, the HB directional two-body interaction, and the HB many-body interaction. In addition, the model takes into account the restructuring effect of water in the first hydration shell by explicitly increasing the strength of the HB by 30%. The coarse-grained model employed in this simulation in the absence of hydrophobic interfaces has been extensively explored and has reproduced the thermodynamic anomalies of water and has predicted a first-order LLPT and the LLCP [27, 32, 34, 35, 37–39, 46, 122, 123, 156]. Furthermore, the model allows to explain the observed phase transition in terms of the proliferation of regions with tetrahedrally ordered molecules.

Using MC simulations, we investigated system sizes up to $\mathscr{N} = 1.6 \times 10^5$ with nanoparticles of radius $R = 1.6$ nm for different concentrations $c \equiv (\mathscr{N} - N)/\mathscr{N}$ ranging from 2.4% to 25%, where N is the total number of water cells. The analysis was repeated for nanoparticles with $R = 0.4$ nm. A snapshot of this coarse-grained model of a water monolayer with hydrophobic nanoparticles of $R = 0.4$ nm and $c = 2.4\%$ is shown in Fig. 7.1 (a).

6.1.2 DMD simulations on mixtures of Jagla ramp potential particles and hard spheres

DMD is a computer simulation method in which particles interact with discontinuous stepwise potentials. In DMD, particles move along straight lines with constant velocities until a collision, signaled by a discontinuity in the interaction potential, is encountered. After this event, the coordinates and velocities of the particles are updated. DMD is an efficient molecular dynamics (MD) technique, and unlike the standard MD method, it allows us to easily simulate potentials containing hard cores. In a sense, DMD is equivalent to a Metropolis MC in which the set of moves is equivalent to the ballistic motion of the particles. As a result, DMD simulations are very efficient when studying polymers, colloids, and lipid membranes [225]

Over the last decade, several papers have shown that the presence of tetrahedrality or even of orientation-dependent interactions in computer models of water are not necessary

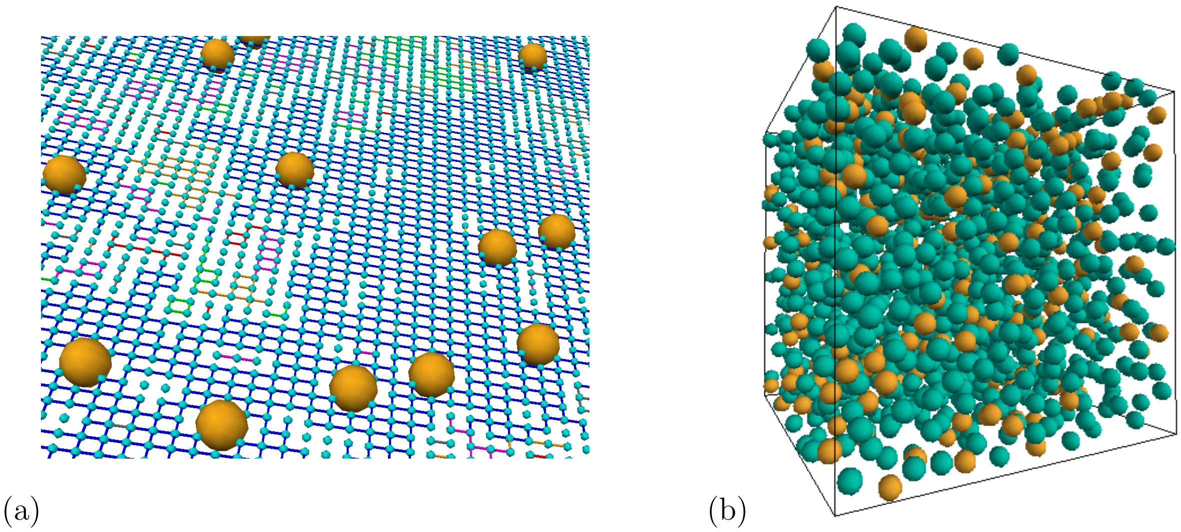

Figure 6.1: (a) Snapshot of an equilibrated configuration for the water monolayer with randomly positioned fixed hydrophobic nanoparticles (yellow spheres) of radius $R = 0.4$ nm. Each water cell is represented by a small cyan sphere. Colored lines represent hydrogen bonds between molecules in nearest neighbor cells, with six possible colors corresponding to different possible bonding states. (b) Snapshot of an equilibrated configuration for the mixture of Jagla ramp particles (green spheres) and HS (yellow spheres) with HS mole fraction $x_{\mathrm{HS}} = 0.20$. The total number of particles is 1728.

conditions for the appearance of water anomalies or of a LLPT [100, 223, 226–243]. In fact, the Jagla potentials, a family of spherically symmetric potentials composed of a hard core and a linear repulsive ramp, can reproduce both water-like anomalies and the LLPT by tuning the ratio between the two characteristic lengths [244–248]. It has been suggested that the hard core length corresponds to the first coordination shell of water molecules while the repulsive ramp length corresponds to the second coordination shell [246–248]. It is important to mention that Jagla potentials differ from water. In particular, the slope of the LLPT in the $P-T$ plane, related to the difference in entropy of HDL and LDL, in the Jagla potentials has an opposite sign with respect to water. It is therefore important to understand the consequences of the differing entropy behavior by comparing the results of the Jagla potentials with those of water-like models.

The investigated systems are mixtures of Jagla ramp particles and HS with identical diameters and the same mass m. The mole fractions studied spanned from $x_{\mathrm{HS}} = 0.10$ to 0.50. A snapshot of the $x_{\mathrm{HS}} = 0.20$ mixture is presented in Fig. 7.1(b).

In Fig. 6.2, the shape of the spherically symmetric Jagla ramp potential is shown. For the results we review, the Jagla potential was built considering a hard-core diameter a and a soft-core diameter, at the end of a linear repulsive ramp, b, where $b/a = 1.72$. The potential was supplemented with an attractive linear tail that extends to the the cutoff $c = 3a$. The potential has been discretized, with the step $\Delta U = U_0/8$, where U_0 is the minimum of the energy that corresponds to the soft-core distance. The repulsive ramp was partitioned in 36 steps of width $0.02a$ and the attractive ramp into eight steps of width $0.16a$. The energy at the hard-core distance is defined as $U_R = 3.56\,U_0$, the value of the least-squares linear fit of the discretized ramp at $r = a$. The systems were simulated at a constant number of particles, volume, and temperature. The temperature was controlled by a modified Berendsen algorithm [225]. For the DMD simulations, all quantities are expressed in reduced units: distances in units of a, energies in units of U_0, times in units $a\sqrt{m/U_0}$, pressures in units of U_0/a^3 and temperatures in units of U_0/k_B. The density is defined as $\rho \equiv N/L^3$, with L the edge of the cubic simulation box, and is measured in units of a^{-3}. The total number of particles is $N = 1728$.

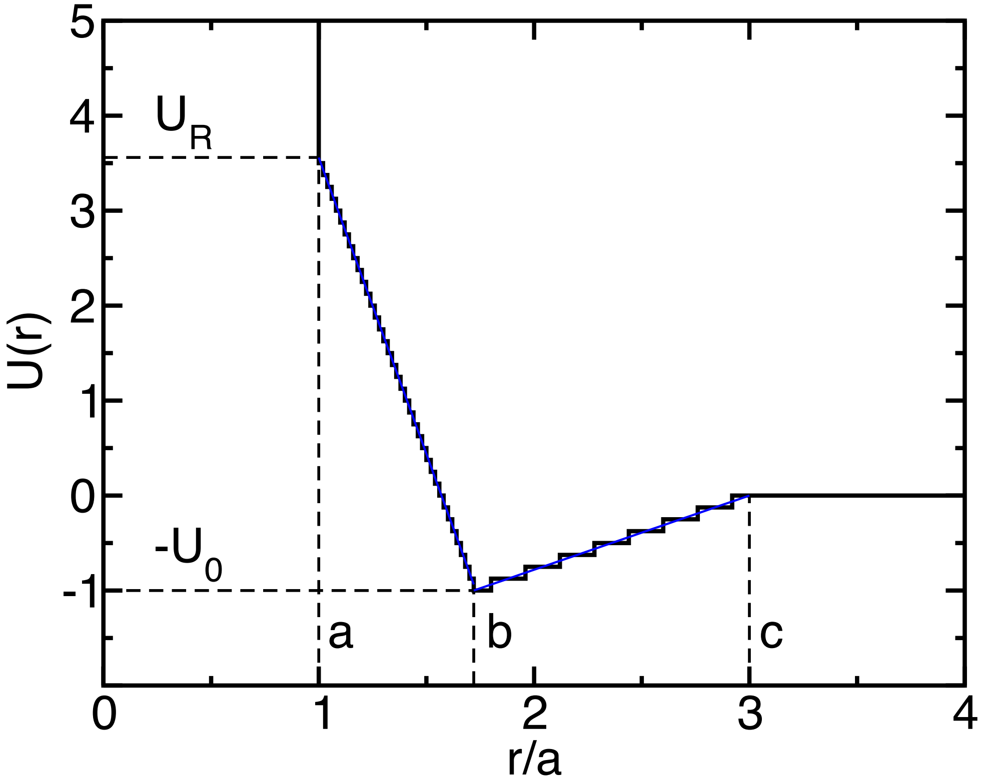

Figure 6.2: Spherically symmetric Jagla ramp potential. Its two length scales correspond to the hard-core distance a and the soft-core distance b. The parameters of the potential studied were set to $b/a = 1.72$ and $U_R/U_0 = 3.56$. The potential was supplemented by an attractive tail and a long range cutoff was imposed at $c/a = 3$. The discretized version of the potential (see text) is shown (black solid line) along with the original continuous version (blue line).

6.2 The LLCP of water in hydrophobic environments

In this section, we present the results obtained in the MC simulations of the coarse-grained model of water confined in a hydrophobic matrix of particles and in the DMD simulations on mixtures of Jagla ramp potential particles and HS. There have been extensive computational studies of both approaches considered here without the addition of the hydrophobic particles [32, 34, 36, 37, 39, 100, 223, 249] that showed the presence of water anomalies, such as the density anomaly and peaks of the thermodynamic response functions. These studies were also consistent with the theoretical predictions of the existence of two types of liquids, i.e., LDL and HDL, in the subfreezing region of the $P-T$ phase diagram of liquid water, separated by a first-order LLPT and terminating with a LLCP. Here we show how the presence of hydrophobic particles affects the liquid–liquid phase diagram of water.

6.2.1 MC simulations on 2D water confined in a matrix of hydrophobic particles

Franzese *et al.* [27, 32, 34, 36–39, 46, 122, 123, 156] previously showed that for $c = 0\%$ the coarse-grained model of a water monolayer employed here for the MC simulations captures the major thermodynamic phenomena of liquid water such as the liquid-gas spinodal, the locus of density maxima, the diffusion anomaly, and a first-order LLPT line that terminates in a LLCP at about 174 K and 0.13 GPa (Fig. 6.3). When we added a fixed matrix of hydrophobic nanoparticles to the water monolayer we observed a decrease in temperature of the liquid-gas spinodal, and a deformation of the TMD line. The TMD line shifts to lower T for P below 0.14 GPa, and to higher T for P above 0.16 GPa [129]. In addition, we noticed a weakening in the first-order LLPT. In particular, at temperatures below 168 K and pressures above 0.15 GPa, there is only one liquid phase and there is no LLPT between the LDL and HDL.

In Fig. 6.4, we compare the isobars for water with the MC simulations of the coarse-grained model in the presence of and in the absence of hydrophobic nanoparticles (concentration $c = 25\%$). For the case of $c = 0\%$ we observe sharp discontinuities in density

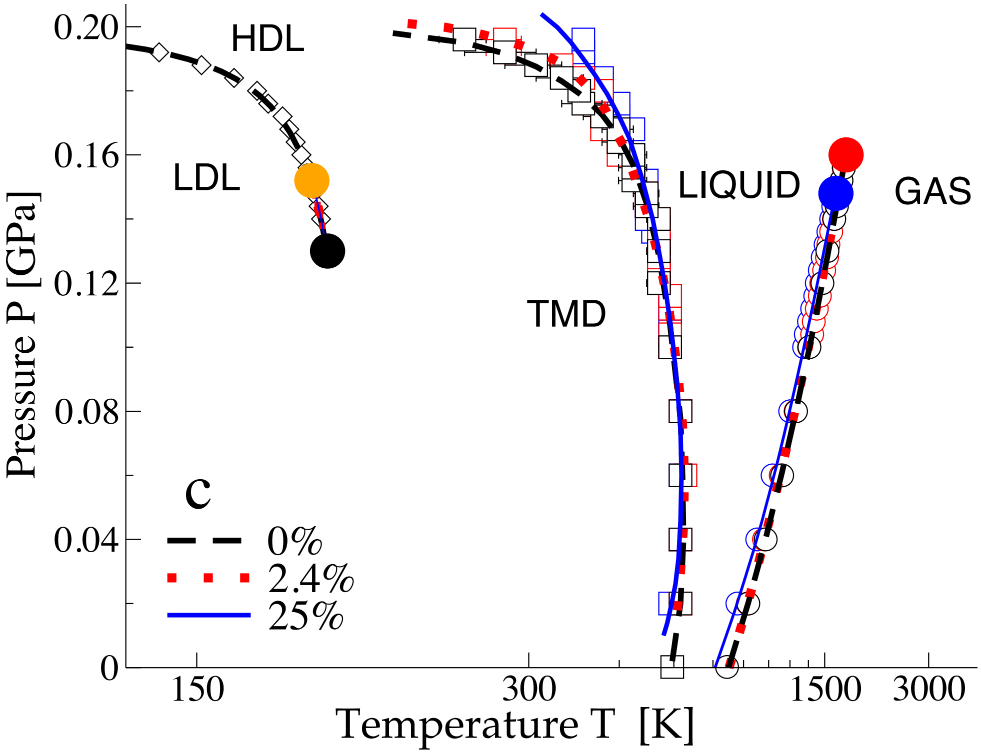

Figure 6.3: $P-T$ phase diagram for the water coarse-grained model at different nanoparticle concentrations c, obtained by MC simulations. The T axis is shown in logarithmic scale. The liquid-gas spinodal is denoted by open circles, the TMD line by open squares and the liquid-liquid spinodal by open diamonds. Lines are guides for the eyes (dashed for $c = 0\%$, dotted for 2.4% and solid for 25%). Critical points are presented as large filled circles. The first-order LLPT between LDL and HDL ends in a LLCP (black circle) at $T \simeq 174$ K and $P \simeq 0.13$ GPa for all c. For $c = 2.4\%$ and 25% a new critical point emerges at approximately $T \simeq 168$ K and $P \simeq 0.15$ GPa, above which the first-order LLPT can no longer be detected. Figure adapted from Fig. 1 of Ref. [129].

ρ for P above 0.13 GPa, which is consistent with a strong LLPT line that terminates at about 0.13 GPa. On the other hand, water confined in the nanoscopic hydrophobic particle matrix displays smaller discontinuities in density than that of $c = 0\%$ in a pressure region between 0.13 GPa and 0.16 GPa. This observation indicates a weakening in the LLPT. Moreover, the maximum slope of ρ vs. T largely decreases above 0.16 GPa, suggesting that there is no first-order phase transition above 0.16 GPa. This result, together with the fluctuation analysis [129], suggests that in this case, the LLPT is delimited by two critical points: one at $P \simeq 0.13$ GPa and another at $P \simeq 0.15$ GPa (Fig. 6.3).

A detailed finite-size scaling study of response functions such as compressibility, thermal expansion coefficient, and specific heat [129] confirms the absence of the LLPT at high P above 0.16 GPa. It also shows that even a small number of nanoparticles, $c = 2.4\%$, is sufficient to reproduce the effect of the reduction of the first-order LLPT to a narrow region in both P and ρ with two critical points at high and low pressures (Fig.6.3).

6.2.2 DMD simulations on mixtures of Jagla ramp potential particles and hard spheres

Several thermodynamic studies employing DMD simulations for bulk Jagla ramp particles have shown a LLPT line that terminates with a LLCP at $T_c = 0.375$, $P_c = 0.243$, and $\rho_c = 0.37$ [100, 223, 249] (see Sec. 6.1.2 for the definition of the quantities). The analysis of the isotherms and isochores of the mixtures of Jagla ramp particles and hydrophobic HS solutes with the same size and mass revealed the existence of a LLPT and a LLCP for all mole fractions investigated. [218].

Figure 6.5 shows that when the mole fraction of the HS in the aqueous solution is increased the position of the LLCP shifts to a lower temperature and higher pressure. This shift can occur because the solvation tendency of the HS in the LDL is stronger than that in the HDL [250–253]. We also notice a narrowing of the region in the $P-T$ plane between the LDL and HDL limit of mechanical stability (LMS) as x_{HS} increases, suggesting a weakening of the LLPT line as solute content increases.

The presence of HS narrows the LDL-HDL coexistence envelope in both the $P-T$

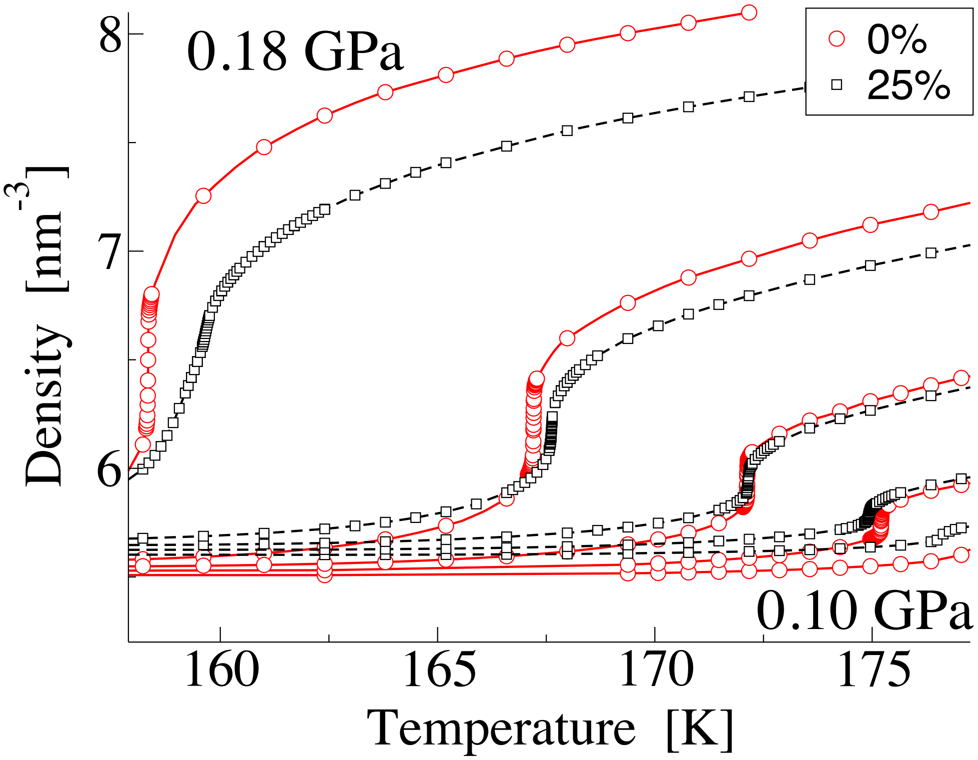

Figure 6.4: MC isobars of the coarse-grained model of water with hydrophobic nanoparticles at concentration c, for a system with size $\mathscr{N} = 1.6\times10^5$. Isobars are for $P = 0.10$ GPa, 0.12 GPa, 0.14 GPa, 0.16 GPa, and 0.18 GPa (from bottom to top) at $c = 0\%$ (red empty circles with solid connecting lines) and at $c = 25\%$ (black empty squares with dashed connecting lines). At high pressures, isobars for $c = 0\%$ display an infinite slope, which is consistent with a strong LLPT. For the case $c = 25\%$, the maximum slope decreases, which is consistent with the absence of the first-order phase transition.

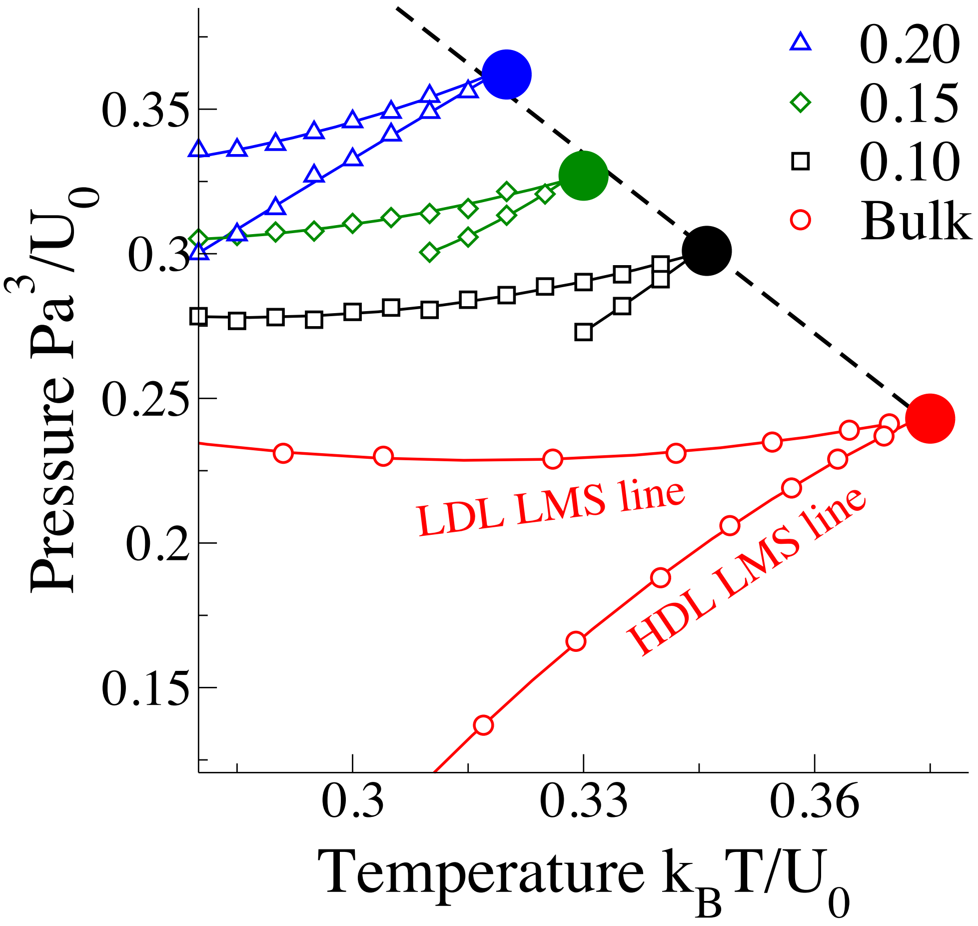

Figure 6.5: DMD simulations on the Jagla ramp potential: comparison of the positions of the LLCP (filled circles) upon the increase of the solute mole fractions from 0, or bulk, (red) to $x_{\mathrm{HS}} = 0.10$, 0.15, and 0.20 (in black, green, and blue respectively). The data points presented with open symbols show the positions of the two branches of the liquid-liquid LMS lines for LDL and HDL (labeled only for bulk, for clarity). Lines connecting the data points are guides for the eyes. Here we observe that upon increasing the solute mole fraction the position of the critical point shifts to lower temperatures and higher pressures and the region enclosed by the LMS lines shrinks. The critical line (dashed) joining the LLPCs of the mixtures is drawn as a guide for the eye. Figure adapted from Fig. 4 of Ref. [218].

and the $P - \rho$ planes. In Fig. 6.6, the isotherms of bulk Jagla particles are compared to the $x_{\mathrm{HS}} = 0.20$ mixtures. Together with the isochores, the liquid–liquid LMS and the liquid–liquid coexistence line are shown. The LMS line is built by joining the extrema of the isotherms, and the coexistence line is obtained by the Maxwell construction. When going from the bulk case to the $x_{\mathrm{HS}} = 0.20$ case, the width of the regions enclosed by both the coexistence line and the LMS line is reduced, indicating a weaker LLPT. The density anomaly, indicated by the crossing of the isotherms in the $P - \rho$ plane, is well defined in the bulk case, but significantly weaker in the $x_{\mathrm{HS}} = 0.20$ case. The phase diagram of the mixtures changes gradually with concentration (not shown), and while a LLCP with a narrower coexistence envelope is apparent up to $x_{\mathrm{HS}} = 0.50$, the density anomaly disappears at the highest mole fraction, $x_{\mathrm{HS}} = 0.50$.

6.3 Comparison to other computational and experimental studies

As we have shown in the previous section, the presence of hydrophobic nanoparticles, either as a confining medium or as a solute, can significantly affect the phase diagram of supercooled liquid water. In particular it affects the behavior of the LLPT and the position of the LLCP. Several studies in the past have addressed the thermodynamic behavior of supercooled water in presence of a hydrophobic environment. Here, we summarize some relevant findings in the literature and compare them to our own results.

Kumar *et al.* [101, 128] performed MD simulations on a system composed of 512 TIP5P water molecules confined between two smooth walls, mimicking solid paraffin. They observed a 40 K decrease in T in the overall phase diagram of confined water with respect to bulk water. The temperature shift was qualitatively explained as being caused by the absence of HBs between the hydrophobic walls and water molecules, which on average reduced the number of HBs per molecule in the confined water, analogous to the case of bulk water at high temperatures. Due to the shift to lower T it was not possible to reach the LLPT found in bulk water. However, inflections in $P - \rho$ isotherms were ob-

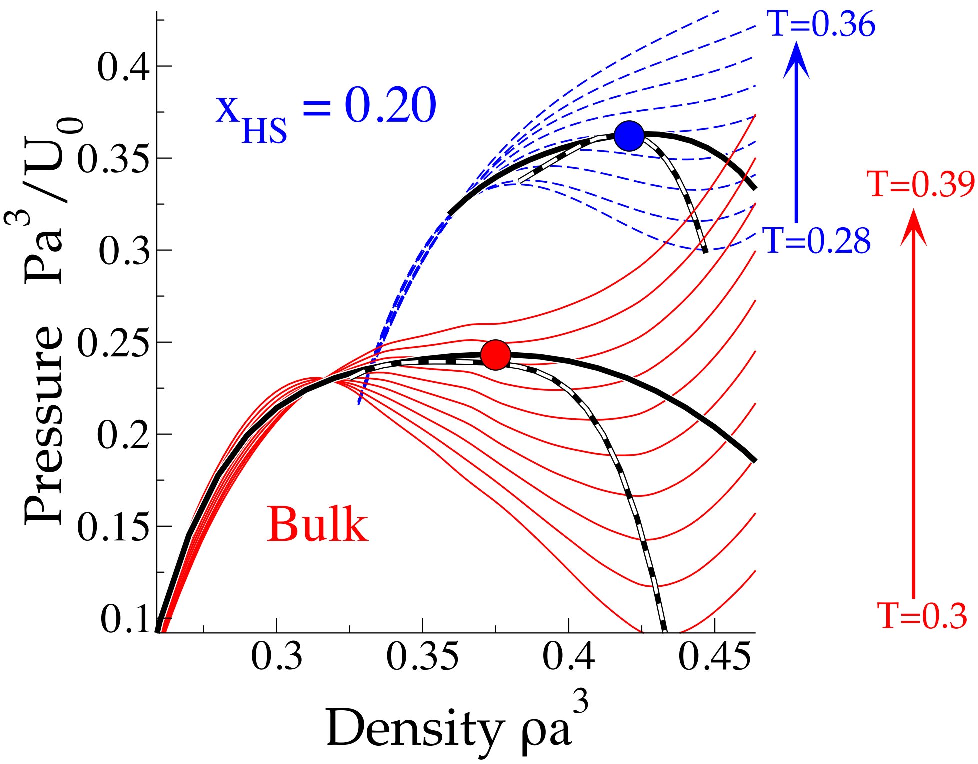

Figure 6.6: DMD isotherms for the Jagla potential. Isotherms are shown as fourth-degree polynomial fits to simulated state points in the $P - \rho$ plane for bulk (red solid lines from $T = 0.3$ to 0.39 with a step of $\Delta T = 0.01$) and $x_{\mathrm{HS}} = 0.20$ solution of HS (blue dashed lines from $T = 0.28$ to 0.36 with a step of $\Delta T = 0.01$). The liquid–liquid LMS lines are outlined by striped curves, and the coexistence regions by thick black curves. In the case of the mixture, the LMS density range is reduced in ρ with respect to the bulk case. The LLCPs are shown as large filled circles. Density anomaly manifests by crossing of the isotherms in the low-density region. This isothermal crossing is very well pronounced in the bulk case and is significantly weaker in the case of the $x_{\mathrm{HS}} = 0.20$ solution. Figure adapted from Fig. 3 of Ref. [218]

served implying the proximity of the system to the LLCP. This result shows that the presence of a LLCP in water in a hydrophobic confinement is plausible also when using 3D, orientational-dependent water models, in agreement with the results found for the 2D coarse grained model studied with MC simulations [129] (see Sec. 6.2.1).

Gallo and Rovere [80] used MD simulation to study the thermodynamic properties of TIP4P water confined in a rigid disordered matrix of hydrophobic soft spheres upon supercooling. Although they also observed a reduction in the average number of HBs, the HB network appeared preserved, in contrast to the case of water confined between hydrophobic plates. Despite the substantial integrity of the network and the small changes found in the structural properties of confined water, significant shifts to higher P and lower T of both the TMD line and the liquid–gas spinodal were found with respect to bulk TIP4P water. The magnitude of the temperature shift is consistent with water confined between hydrophobic plates. The authors suggested a weak dependence of the properties of water on the hydrophobic confining medium. The existence of a TMD line and liquid–gas spinodal in TIP4P water confined in a rigid disordered matrix of hydrophobic objects compares well with the results shown for the MC simulations (see Sec. 6.2.1).

Chatterjee and Debenedetti [219] conducted theoretical investigations of the effect of apolar solutes with different strengths of dispersive interactions (solute-solute interactions) on the mixture phase behavior. They compared this to the bulk phase behavior for a model that incorporates the presence of the LLPT line and the LLCP and found a critical line originating at water's second critical point for aqueous mixtures. This line extended towards low P and high T as the solute mole fraction was increased, suggesting a possible accessible experimental manifestation of the LLCP in the deeply supercooled water. The existence of a critical line originating at the LLCP of water in solution of hydrophobic objects is in agreement with the results found in the DMD simulations on mixtures of Jagla ramp particles and HS [218] (see Sec. 6.2.2). The difference in the direction of the shift of the LLCP in solutions could be due to the presence of dispersive interactions between apolar particles in the Chatterjee and Debenedetti model and/or to the different slope of the liquid–liquid coexistence line, negative in their case, positive in the Jagla model.

Urbic *et al.* [145] modeled two-dimensional *Mercedes-Benz* water, freely mobile in a rigid disordered matrix of Lennard-Jones disks. They found that the presence of the obstacles induced perturbations in the water structure. They also demonstrated that high disk densities greatly affect the HB network, and cause a reduction in such response functions as compressibility, in agreement with what was observed in the MC 2D coarse grained model [129].

Finally, Zhang *et al.* [150] reported experimental results of a 17 K shift towards lower T of the TMD line in water confined in the hydrophobic mesoporous material CMK-1-14, which consists of micrometer-sized grains, each with a three-dimensional interconnected bicontinuous pore structure, with an average pore diameter 14Å, at a hydration level of 99% at ambient pressure. They measured the broadening of the thermal expansion coefficient peak in hydrophobic CMK confinement, contrasting with the sharp peak in the hydrophilic confinement in silica MCM mesopores. The reduction of the anomalous properties of water in hydrophobic environments agrees with what was observed both in the MC simulations on the 2D coarse-grained model [129] (see Sec. 6.2.1) and in DMD simulations on the Jagla model [218] (see Sec. 6.2.2).

In all of these studies, the effect of the hydrophobic confinement is revealed by a shift in $P-T$ of the thermodynamic loci. Furthermore, experiments [150] and simulations [129, 145] reveal a reduction of the fluctuations with respect to the less hydrophobic cases. In particular, this decrease of fluctuations could be relevant even when the hydrophobic nanoparticle concentration is small [129].

We finally remark that the difference in entropy behavior between the Jagla potential and water, and in particular the coarse-grained model of water presented here, should be taken into account when comparing the results, as this is possibly the origin of the different effect of the hydrophobic confinement on the LLPT. In the isotropic Jagla potential, the LDL phase has a *larger* entropy than the HDL phase and consequently, through the Clausius-Clapeyron equation $(dP/dT) = (\Delta S/\Delta V)$, the HDL-LDL coexistence line has a positive slope. In water and in the coarse-grained model presented here, the LDL phase has a *smaller* entropy than the HDL phase, thus the slope of the HDL-LDL coexistence line is negative. In the Jagla potential with hydrophobic solute [218] the entire LLPT shifts to lower T and higher P as the solute molar fraction is increased. On the other hand, for the coarse-grained model of water confined by hydrophobic nanoparticles between hydrophobic walls [129], the LLCP is almost not affected by the increase of the nanoparticle concentration, but the LLPT is weakened, and eventually disappears, at high P.

6.4 Conclusions

We have reviewed and compared two recent computational works describing the changes in the thermodynamic behavior in the supercooled region of water and in the LLCP phenomenon for water in hydrophobic environments. We have compared these works with previous reports for water in hydrophobic environments in order to give an overview of the modifications in the phase diagram of water at subfreezing temperatures. We have seen that the presence of a hydrophobic environment can significantly alter the thermodynamic properties of water. The reported temperature shifts in water anomalies and critical points, and the weakening of the LLPT as well as its disappearance at high pressures observed in the MC simulation case, are relevant to current biological research. In biological systems, water is often found in contact with hydrophobic objects, and the results shown can play a crucial role in studies of cryopreservation, in which the reduction of volume fluctuations and the inhibition of ice formation can minimize cell damage.

Part III

Simulations of anomalous liquids

Chapter 7

Discrete Molecular Dynamics

Recently, the study of complex liquids has been significantly advanced by the development of simplified models that capture the essential features of the systems and at the same time, allow very fast simulations. One such approach is the discrete molecular dynamics (DMD). DMD is a qualitatively different kind of molecular dynamics (MD) that is useful in dealing with potentials that are discontinuous functions of the distance. This kind of MD is *collision driven*, where a so called collision takes place each time the distance between two particles in the system becomes equal to a point of discontinuity in the interaction potential. In DMD, the atoms or group of atoms are replaced by hard spheres interacting via discontinuous stepwise potentials. DMD is frequently used in studies of simple liquids [223, 227, 230, 233, 238, 246, 275, 277], polymers, [278–280] colloids [281, 282], and lipid membranes [283].

The molecular dynamics of molecules interacting via hard sphere discontinuous potentials must be solved in a different way that is qualitatively different from the molecular dynamics of soft bodies, such as Lennard-Jones type systems. Thus, in DMD, particles move along straight lines with constant velocities until a moment of collision. At the collision, velocities of particles change instantaneously, and can be determined using the conservation laws of energy, momentum and angular momentum.

In Fig. 7.1 a schematic diagram of a collision between two particles is visualized. For two particles i and j with mass m_i and m_j respectively, traveling at constant velocities $\overrightarrow{v}_i$

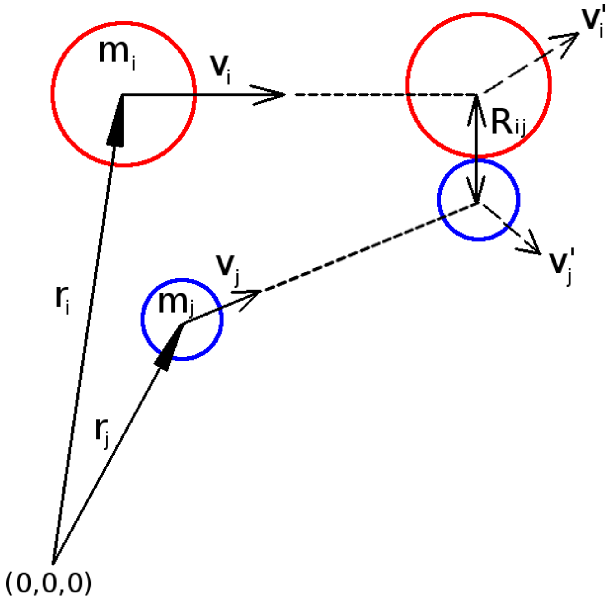

Figure 7.1: Diagram of a collision between two particles. The initial positions of the particles of mass m_i and m_j are $\overrightarrow{r}_i$ and $\overrightarrow{r}_j$ respectively. They travel at constant velocities $\overrightarrow{v}_i$ and $\overrightarrow{v}_j$, collide at distance R_{ij} and their velocities are modified to $\overrightarrow{v}'_i$ and $\overrightarrow{v}'_j$. Courtesy of S. V. Buldyrev.

and $\overrightarrow{v}_j$ from the initial positions $\overrightarrow{r}_i$ and $\overrightarrow{r}_j$, the collision distance is R_{ij}, corresponding to a point of discontinuity in the interaction potential. If we define $\overrightarrow{r}_{ij} = \overrightarrow{r}_i - \overrightarrow{r}_j$ and $\overrightarrow{v}_{ij} = \overrightarrow{v}_i - \overrightarrow{v}_j$, the collision time is determined by the equation

$$(\overrightarrow{r}_{ij} + \overrightarrow{v}_{ij} t_{ij})^2 = R_{ij}^2. \tag{7.1}$$

The DMD algorithm calculates the shortest collision time in the system

$$\delta t = \min_{\mathrm{i<j}} t_{ij} \tag{7.2}$$

and allows the motion of all particles in the system until the next collision time, so that

$$\overrightarrow{r}'_i = \overrightarrow{r}_i + \delta t \overrightarrow{v}_i. \tag{7.3}$$

The minimization of the t_{ij} is optimized by dividing the system into small subsystems, so that collision times are computed only between particles in the neighboring subsystems.

Then we find new velocities $\overrightarrow{v}'_i$ and $\overrightarrow{v}'_j$ for particles i and j from the conservation laws of momentum:

$$m_i \overrightarrow{v}_i + m_j \overrightarrow{v}_j = m_i \overrightarrow{v}'_i + m_j \overrightarrow{v}'_j, \tag{7.4}$$

angular momentum:

$$m_i[\overrightarrow{r}'_i \times \overrightarrow{v}_i] + m_j[\overrightarrow{r}'_j \times \overrightarrow{v}_j] = m_i[\overrightarrow{r}'_i \times \overrightarrow{v}'_i] + m_j[\overrightarrow{r}'_j \times \overrightarrow{v}'_j], \tag{7.5}$$

and total energy

$$\frac{m_i v_i^2}{2} + \frac{m_j v_j^2}{2} + U_{ij} = \frac{m_i v_i'^2}{2} + \frac{m_j v_j'^2}{2} + U'_{ij}, \tag{7.6}$$

where U_{ij} and U'_{ij} are the values of the pair potential before and after the collision. The DMD algorithm is more efficient than standard MD for low density systems [230]. The positions and velocities of the particles are updated only when they collide. As in regular MD, it is possible to work in different ensembles in DMD.

The temperature of the system is calculated according to the equipartition theorem. For a three dimensional system with N particles, the instantaneous temperature T is

$$T = \frac{1}{3Nk_B} \sum_{i=1}^{N} m_i v_i^2. \tag{7.7}$$

For the constant temperature simulations, a modified Berendsen algorithm [223, 275] can be applied to rescale the velocities of the particles by multiplying all the velocities at each time step Δt by a factor $\sqrt{T'/T}$

$$T' = T(1 - \kappa_T \Delta t) + T_0 \kappa_T \Delta t \tag{7.8}$$

where T' is the new instantaneous temperature, T_0 is the temperature of the heat bath, and κ_T is the heat exchange coefficient.

The average pressure P of the system is computed using the virial theorem, which relates the time average of the total kinetic energy to the time average of the virial. Thus P is calculated at the moment of collision t_ℓ during the time interval Δt over particles $i(\ell)$ and $j(\ell)$ that are involved in the collision ℓ with the change in momentum $\overrightarrow{p}_{i(\ell)}$:

$$P = \frac{Nk_B}{V}\langle T \rangle_\Delta t - \frac{1}{3V\Delta t} \sum_\ell \Delta \overrightarrow{p}_{i(\ell)}(t_\ell) \cdot [\overrightarrow{r}_i(t_\ell) - \overrightarrow{r}_j(t_\ell)] \tag{7.9}$$

Constant pressure simulations are performed using the Berendsen algorithm [276] that rescales the positions of the particles of the system and the box vector each Δt_P time steps:

$$\overrightarrow{r}'_i = \overrightarrow{r}_i + \overrightarrow{r}_i \kappa_P (\bar{P} - P_0) \tag{7.10}$$

$$\overrightarrow{L} = \overrightarrow{L} + \overrightarrow{L}\kappa_P(\bar{P} - P_0) \tag{7.11}$$

where $\overrightarrow{L} = (L_x, L_y, L_z)$ is a vector containing the lengths of the edges of the simulation box, P_0 is the barostat pressure, $\bar{P}$ is the average pressure during Δt_P and κ_P is the pressure rescaling coefficient.

Chapter 8

Nanoparticle Confinement in Anomalous Liquids

Many experiments in recent years have shown that there is a number of liquids whose properties are highly anomalous [243]. For example, data for liquid metals, metalloids, nonmetals, oxides and alloys, including Ga, Bi Te, S, Be, Mg, Ca, Sr, Ba, SiO_2, P, Se, Ce, Cs, Rb, Co, Ge, $Ge_{15}Te_{85}$ [243], reveal the presence of a temperature of maximum density (TMD) below which the density decreases under isobaric cooling. The most famous example of anomalous liquid is water, whose TMD at 1 atm is at approximately 4^oC. Another anomaly that is attracting considerable attention is the possible existence of a liquid–liquid phase transition (LLPT) for single-component systems. Based on simulations for water [66], it has been proposed that the two coexisting liquids, the high density liquid (HDL) and the low density liquid (LDL), would differ in density and local structure. Liquid polymorphism is observed in experiments on P, [254–256], $P(OC_6H_5)_3$ [257–259] and yttrium oxide-aluminum melts [260]. Data consistent with a LLPT arise from experiments for single-component systems, such as water [173], silica [261, 262], C [263], Se [264], Co [265], among others [266–268]. Here we ask the question how nanoconfinement of an anomalous liquid may change its behavior. The question is relevant for the vast arena of nanotechnological applications and for the lively debate about the properties of confined water in nanoscopic and biological systems [129, 138, 139, 157, 162–164, 218].

8.1 Simulation details

To approach the problem we focus on the effects of the structure of a fixed confining matrix of nanoscopic particles (NPs) on the phase diagram of a liquid with anomalous behavior and with a LLPT ending in a liquid-liquid critical point (LLCP). As model liquid we consider (i) a ramp potential [100, 223, 269], and for comparison (ii) a shoulder potential [240–242].

Potential (i) has a hard-core at distance $r = a$, and a linear ramp for $a < r \leq b$ decreasing from interaction energy $U_R > 0$ to $U_0 < 0$, plus a linear ramp for $b < r \leq c$ increasing from U_R to 0. We adopt $b/a = 1.72$, $c/a = 3$ and $U_R = 3.56U_0$. For this set of parameters the LLCP lies well above the melting line [228]. The interaction with the NPs is modeled by the hard sphere repulsion.

Potential (ii) has a repulsive shoulder and an attractive well with energy minimum U_0, [240–242] with parameters chosen to fit a potential proposed for water [270]. The interaction with NPs is given by a $1/r^{100}$ power law that crosses the zero of the interaction energy at the unit distance a. Results presented in the following, if not otherwise indicated, are for the potential (i), with consistent results for potential (ii).

Both potentials (i) and (ii) display water-like anomalies and a LLPT [100, 223, 240–242, 269]. For both we perform simulations at constant number N of particles, constant volume V and constant temperature T, with periodic boundary conditions. For (i) we employ a discrete molecular dynamics algorithm by discretizing the linear ramp potential into steps, with $\Delta U = U_0/8 = 0.125$ [225]. For (ii) we integrate the equations of motion using velocity Verlet integrator and we adopt the Allen thermostat [240–242].

We confine the liquid particles in a fixed matrix of $N_{\mathrm{NP}} = 64$ nanoparticles of diameter $D_{\mathrm{NP}} = 3a$. The liquid particles interact with NPs via hard core repulsion at distance $r_0 = (a + D_{\mathrm{NP}})/2$. We consider three different structures for the matrix: a perfect cubic lattice (CUBE); a cubic lattice with Gaussian distortions (DIST) with a standard deviation of 1/4 of the separation between centers of NPs, which still preserves an approximately periodic and ordered structure of the confinement (Fig.8.1a); and a completely random (RND) configuration of NPs obtained by simulating a gas of hard spheres (Fig.8.1b). The volume fraction of NPs is $x_{\rm NP} = V_{\rm NP}/V = 24.5\%$ in a cubic simulation box with fixed volume $V/a^3 = (20.6)^3$, and $V_{\rm NP}/a^3 = N_{\rm NP} 4\pi(r_0/a)^3/3$ volume of NP. We repeat the analysis for a random configuration of NPs with diameter $5a$, keeping constant $x_{\rm NP}$ and the size of the simulation box. We control $\rho = N/(V - V_{\rm NP})$ of liquid particles by adjusting N. We account for the excluded volume by rescaling the pressure P by $V/(V - V_{\rm NP})$.

8.2 Results

For potential (i), the bulk liquid displays a LLCP at $k_B T_C^{\rm bulk}/U_0 = 0.375$, $P_C^{\rm bulk} a^3/U_0 = 0.243$, and $\rho_C^{\rm bulk} a^3 = 0.37$ [100, 223, 269]. Figures 8.1(c) and 8.1(d) show simulated isochores for DIST and RND confinement, respectively, with the HDL-LDL spinodal lines calculated from $(\partial P/\partial \rho)_T = 0$ and $(\partial^2 P/\partial \rho^2)_T \neq 0$, and the LLCP obtained from the merging of the spinodal lines where $(\partial P/\partial \rho)_T = (\partial^2 P/\partial \rho^2)_T = 0$. For each confinement we find that the LLCP shifts to lower T, higher ρ, and higher P relative to the bulk liquid (Fig.8.2a). As the disorder in the confining matrix increases, T shift becomes more pronounced while ρ and P shifts are reduced. We find the same qualitative trend in the LLCP shifts for the liquid with potential (ii), and a progressive approach of the LLCP to the bulk case when the NPs concentration decreases (Fig.8.2b), consistent with previous results for NP-liquid mixtures [218].

Although the periodic DIST confinement preserves the LDL-HDL coexistence region observed in bulk liquid [100, 223, 269], which is consistent with a strong first-order LLPT, the RND confinement shrinks the coexistence region (Figs. 8.1c and 8.1d), hinting at a weakening in the LLPT. This weakening is qualitatively consistent with recent numerical results for supercooled water in random hydrophobic pore-like confinement [129].

The region of density anomaly is bounded by the lines of TMD and temperature of minimum density (TminD) located by the extrema of the isochores. In the bulk system the TminD line for high densities is hindered by the glass transition line and cannot be observed in the equilibrium liquid. Here we observe that the periodic structure of the confinement can dramatically affect density anomaly manifestations. Comparatively to the bulk, confinement decreases TMD and increases TminD, shrinking the T range of the

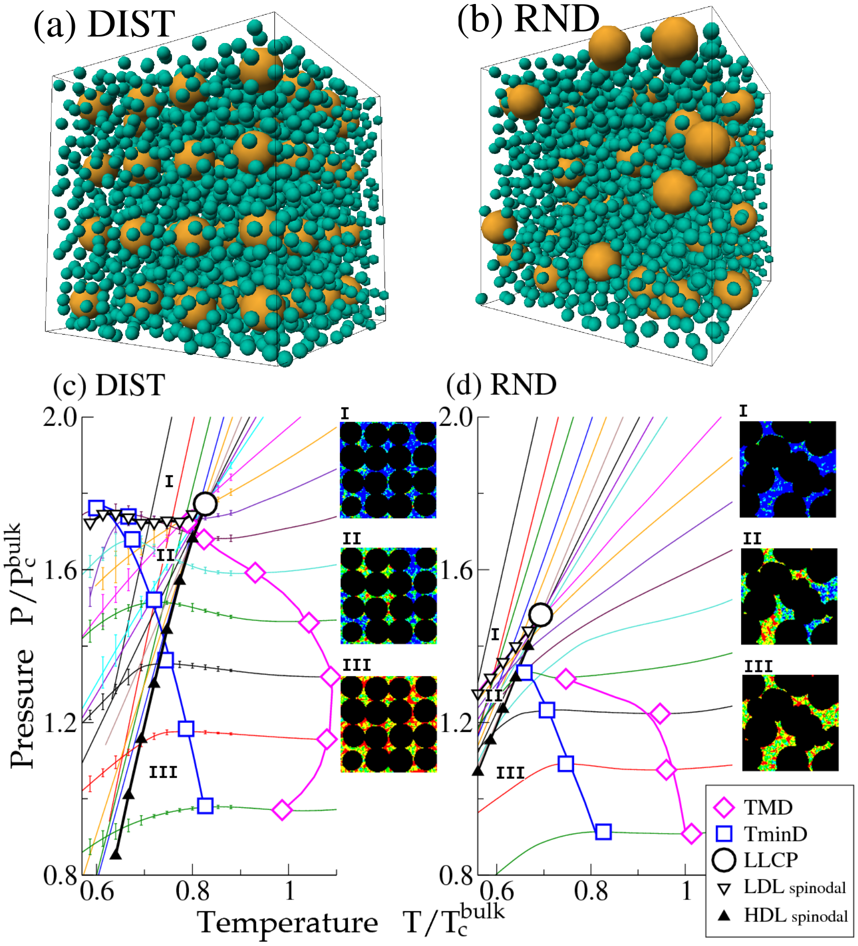

Figure 8.1: Effect of confinement. Snapshots of the anomalous liquid (green) confined in a fixed matrix of NPs (yellow) in a DIST (a) and RND (b) configuration. Polynomial fits of simulated isochores of densities $0.89 \leq \rho/\rho_C^{\mathrm{bulk}} \leq 1.59$ (bottom to top at $T/T_C = 1$) for DIST (c) and RND (d). Randomness reduces the temperature and pressure of the LLCP (circles), the separation between the HDL (lower filled triangles) and LDL spinodals (upper open triangles) and the separation between the TMD (diamonds) and the temperature of minima of densities (TminD, squares). Samples of error bars on P are given in panel (c). Lines connecting symbols are guides for the eyes. Insets: cuts through the simulation box at density above (I), between (II) and below (III) the coexistence densities. The black circles (with a maximal radius of $3.5a$) mark regions where liquid particles stick to the NPs, as discussed in the text. Outside these regions the liquid density is represented by a color code going from blue (high liquid density) to red (low liquid density).

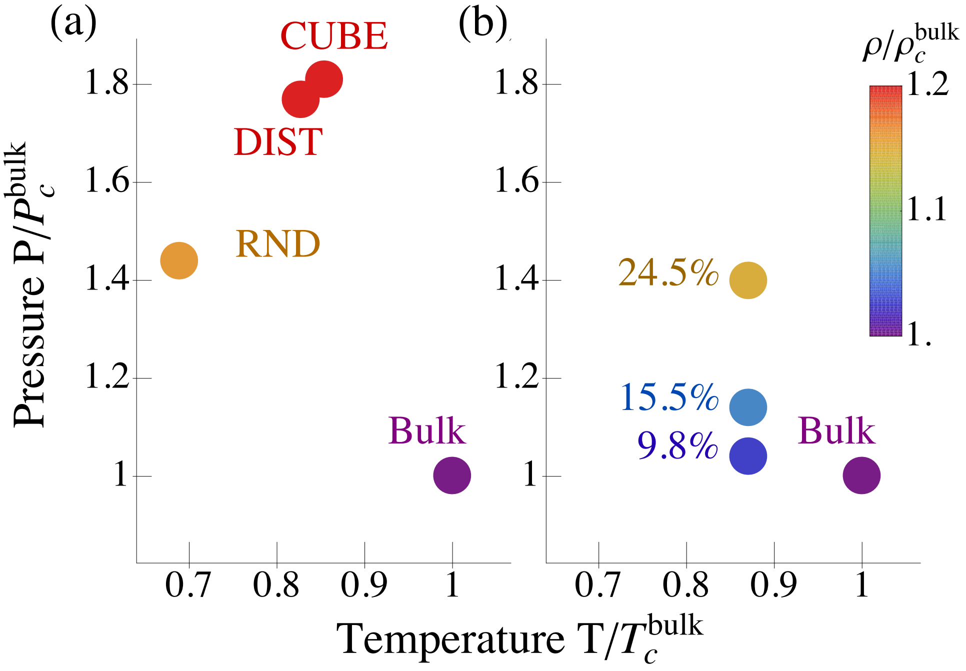

Figure 8.2: The confinement affects the parameters of the LLCP. Color-coded circles represent the LLCP parameters in the $P-T-\rho$ phase space (a) for the liquid confined in the fixed matrix of NPs with CUBE, DIST and RND configuration. Increasing disorder in the confinement, from CUBE to DIST to RND, shifts the LLCP down in ρ, T, and P. (b) Upon decreasing concentration x_{NP} (label near the symbols) for the CUBE confinement of the liquid with potential (ii), the LLCP approaches the bulk case. We find the same behavior for potential (i).

density anomaly. While for the DIST confinement the density anomaly is still well defined, it appears much less pronounced in RND case. For a RND matrix of large confining NPs with diameter $5a$, TMD and TminD are completely absent (not shown).

8.3 Discussion

To understand the origin of the different effects for the different confinements, we first study the density of the liquid in the vicinity of NPs. We find that a layer of liquid adsorbs onto the NPs, as emphasized by the NP-liquid particle radial distribution functions $g_{\mathrm{NP-liq}}(r)$(Fig.8.3a). We understand the increase of density near the NP surface as a consequence of the maximization of entropy. By sticking to the fixed NPs, the adsorbed liquid particles allow more free space to the the rest of the liquid, maximizing the entropy of the system (depletion effect). This result evokes a similar effect found for water forming a high-density layer of ≈ 5 Å at confining surfaces, regardless of the hydrophobic or hydrophilic interaction with the surface [191, 271–274].

We find that, by increasing randomness in the confinement, the probability of overlap of NP exclusion volumes increases and the depletion effect decreases. As a consequence, the density of liquid near the NPs decreases (Fig.8.3b). In addition, we analyze the density fluctuations and the associated measurable response function, the isothermal compressibility K_T (Fig.8.3a), of the liquid in the vicinity of the NPs. We find that the local K_T is extremely small right at the interface, consistent with a tight packing of liquid particles around the NPs. Near the first minimum of $g_{\mathrm{NP-liq}}(r)$ the local K_T is, instead, twice as high as the bulk, consistent with [271]. High vicinal density of liquid rationalizes the density increase of the LLCP (Fig.8.2), because, when part of the liquid is adsorbed onto the NPs, an average liquid density larger than bulk is necessary to build up the critical fluctuations. The shift is more pronounced for CUBE and DIST confinement, with respect to RND, because the more ordered the confinement the larger the NP surface available for the depletion effect.

To understand the distribution of local density inside the simulation box, we performed Delaunay tessellation for a set of NPs in both RND and DIST confinements, partitioning

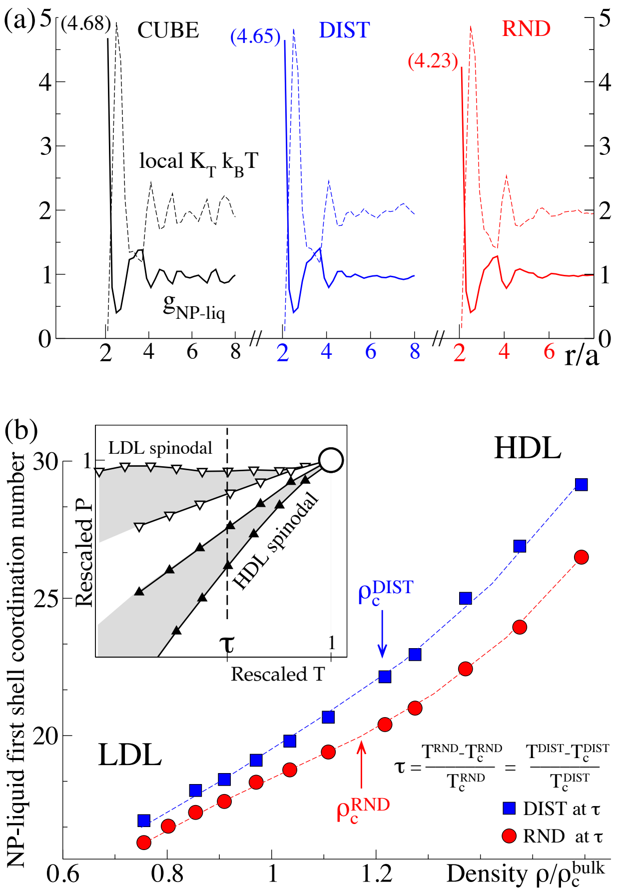

Figure 8.3: (a) The liquid adsorbs onto the NPs. The NP-liquid particle radial distribution functions $g_{\mathrm{NP-liq}}(r)$ at $T/T_C^{\mathrm{bulk}} = 1.12$ for CUBE (leftmost), DIST (center) and RND (rightmost) confinements for density $\rho/\rho_c^{\mathrm{bulk}} = 1.59$ (thick lines) display large maxima (in parenthesis) at the closest NP-liquid particle distance $r = r_0 \equiv 2a$. Normalized local compressibility $K_T k_B T$ (broken lines) computed from the fluctuations of the number of particles in volume $5.5a^3$ shows large peaks near the minimum of $g_{\mathrm{NP-liq}}(r)$. The results for different confinements are shifted horizontally for clarity. (b) Number of liquid particles adsorbed onto a NP, at a distance $r_0 \leq r \leq 2.5a$, where the first minimum of $g_{\mathrm{NP-liq}}(r)$ occurs, for DIST (blue squares) and RND (red circles) for a range of densities at fixed rescaled temperature $\tau = (T^{\mathrm{RND}} - T_c^{\mathrm{RND}})/T_c^{\mathrm{RND}} = (T^{\mathrm{DIST}} - T_c^{\mathrm{DIST}})/T_c^{\mathrm{DIST}} = -0.13$. Arrows mark the location of the critical density ρ_c^{RND} (red) for RND and ρ_c^{DIST} (blue) for DIST. Lines are guides for the eyes. (Inset) The rescaled LDL-HDL coexistence region, with the chosen value for τ, for DIST (gray) and RND (white) confinements, ending in the LLCP (circles).

the total volume into space-filling irregular tetrahedra with four nearest neighbor NPs as vertices (Fig.8.4a,b insets). We find that the RND confinement, with respect to the DIST case, induces a larger heterogeneity in the distribution of local densities ρ_v in each tetrahedra at any fixed value of the global density ρ (Fig.8.4a,b). The significant overlap of ρ_v distributions for the HDL and the LDL phases in RND confinement (Fig.8.4a) suggests the presence of disordered mesoporous microdomains of various densities (Fig.8.1d insets) that contribute to the weakening of the LLPT. This is not observed in DIST case (Fig.8.4b), where the distributions of ρ_v are closely centered around the average global ρ with no overlap between HDL and LDL phases, preserving a strong LLPT.

The fact that for RND confinement the local density is more heterogeneous and the liquid-liquid coexistence occurs at the local scale within Delaunay tetrahedra, allows us to rationalize the T-decrease of the LLCP with respect to the more ordered confinements and the bulk. Local heterogeneity inhibits the global LLPT, driving the LLCP temperature to a lower value. Due to the positive slope of the LLPT, the decrease of LLCP temperature implies a decrease of the LLCP pressure (Fig. 8.2). The presence of density heterogeneity, along with the reduced depletion effect in the RND confinement matrix, gives us the key to understand the differences between ordered and disordered confinement.

8.4 Conclusion

In conclusion, we predict that anomalous liquids, with a LLPT, preserve their bulk phase diagram and density anomalies when are confined in a matrix of periodically ordered NPs. Moreover, in the case of small distortion of the ordered confinement, the homogeneous crystal nucleation is inhibited at temperatures lower than in bulk, allowing the direct observation of the TminD locus. A strong depletion effect induces a large increase of density in the vicinity of the NPs. The effect is smaller when the confinement has a random structure. Randomness induces the occurrence of disordered density domains weakening the LLPT, narrowing the LLPT coexistence region, and washing out the density anomalies.

It is interesting to mention that these results could qualitatively explain recent experiments for confined water, the prototypical anomalous liquid. While the TminD locus

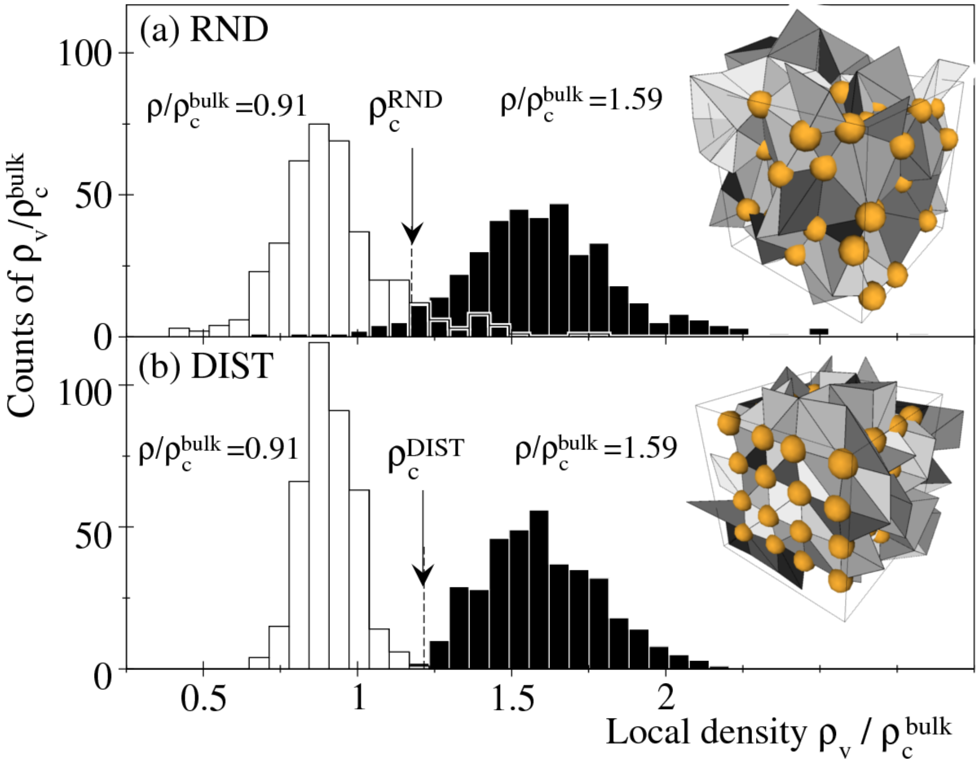

Figure 8.4: RND confinement induces heterogeneity in local densities. (a) The distribution of local density $\rho_v/\rho_c^{\text{bulk}}$ of the liquid included in Delaunay tetrahedra of the RND confinement for the LDL global density $\rho/\rho_c^{\text{bulk}} = 0.91$ (white histogram) partially overlaps with that for the HDL $\rho/\rho_c^{\text{bulk}} = 1.59$ (black histogram). (b) The overlap is not present for the DIST case. In both panels an arrow marks the critical density, ρ_c^{RND} for RND and ρ_c^{DIST} for DIST. Insets: Delaunay tetrahedra for RND (top) and DIST (bottom) case, colored according to the value of ρ_v, from high (dark gray) to low (light gray).

has been observed in supercooled water under hydrophilic confinement by MCM-41 silica nanoporous matrix [69], its absence has been reported in hydrophobic mesoporous material CMK [150]. MCM-41 forms a very regular matrix [69], while CMK consists of grains, each with a disordered, 3D interconnected bicontinuous, pore structure [150]. Therefore, as shown in our model for a generic anomalous liquid, the disparity of results for different kinds of confinements may arise from the different amount of disorder in the confining structures.

Part IV

Lysozyme in an aqueous solution of sugar

Chapter 9

All-atom simulations of lysozyme in aqueous solution of trehalose

9.1 Introduction

Water molecules play a crucial role in determining protein structure, dynamics, and functionality. As a result of the essential presence of water, preservation of the structural and functional integrity of biomolecules is a key problem in current research. One of the most interesting state-of-the-art question is to find methods of preserving proteins at low temperatures while avoiding water crystallization. It is generally accepted that carbohydrates are one of the most important classes of pharmaceutical glass-formers for prolonging the shelf life of labile biological molecules. Sugars are often used in pharmaceutical, food industry, and biomedical applications to prepare glassy matrices for long-term storage of biological materials [284]. In recent years, trehalose, a naturally occurring disaccharide of glucose [285], received considerable attention for its extraordinary biopreservation ability [286, 287]. It has been demonstrated that trehalose is naturally produced by several organisms in response to severe external stresses such as temperature changes or dehydration [288]. In addition, trehalose showed the ability to stabilize living cells subjected to freezing [289, 290].

Despite its importance in cryopreservation and desiccation protection, the microscopic mechanism responsible for the ability of trehalose, and sugar in general, as an effective bioprotectant is still unclear.

It has been previously demonstrated that water molecules interacting with trehalose have completely different dynamical behavior with respect to that of bulk-like water [220]. In aqueous solutions of trehalose, a “destructuring” effect on the water network has been observed in addition to a dramatic slowing-down of water dynamics [291].

Several hypotheses have been suggested to explain the superior effectiveness of trehalose in preserving biomolecules. The “water-replacement” hypothesis assumes that sugars hydrogen-bond to biomolecules during dehydration or freeze-drying, acting as substitutes of hydration water molecules [292]. Alternative scenarios have been proposed in which some specific properties of sugar/water solutions are responsible for the bioprotective capability. Similarly to the encapsulation of insects in amber, Green and Angell [293] advanced that biomolecule motions are inhibited due to the vitrification upon cooling of the sugar/water solutions. Raman scattering results about protein-trehalose interactions led Belton and Gil [294] to propose a different mechanism: trehalose would be particularly capable of creating a cage containing sluggish water molecules around the protected biostructure which would serve both for maintaining a high level of hydration and for smoothing molecular motions, which would lead to denaturation of proteins upon cooling.

9.2 Computational setup

We performed molecular dynamics (MD) all-atoms simulations on the on the hen-egg lysozyme protein immersed in a mixture of water and and α, α-trehalose. The system contained 1 lysozyme protein, 491 trehalose molecules and 13982 water molecules. The charges on the lysozyme residues were neutralized adding 8 Cl^- counterions. The ratio of trehalose to water molecules 1:28.5 corresponds to a weight percentage $\phi = 40$ wt% (not considering the protein and the ions), with the trehalose molarity being approximately $M \simeq 1.33$ mol/l. This concentration was chosen because previous studies have shown that the relative effect of trehalose on water dynamics becomes particularly noticeable at this threshold concentration [295, 296].

The geometrical structure of the lysozyme was obtained from crystallographic experimental data [297] (Protein Data Bank entry 193L). The bonded and non-bonded interactions parameters for the lysozyme and for trehalose were taken from the CHARMM force-field for proteins [298, 299] and for sugars [300, 301]. The water solvent was modeled using the SPC/E potential [302].

The initial configuration of the system was obtained placing the lysozyme at the center of the cubic simulation box and distributing the other molecules at random positions. After a short energy minimization run, the system was equilibrated for 4 ns with the position of the protein atoms restrained, after which the starting configuration was produced. We studied three temperatures $T = 300$ K, $T = 280$ K and $T = 260$ K. At all temperatures the system was equilibrated for 10 ns before running the production run for another 10 ns. Configurations of the the higher temperatures were used as starting configuration for the lower ones. The pressure was kept fixed at the atmospheric pressure. Temperature and pressure were controlled by weak coupling algorithms [276]. At all temperatures the average density of the system is $\rho \simeq 1.2$ g/cm^3.

The equation of motions were integrated using the Verlet leap-frog algorithm and a time step of 1 fs. Periodic boundary conditions were applied. The cut-off radius for non-bonded Lennard-Jones short ranged interactions was set to 1 nm, while the electrostatics was dealt employing the particle-mesh Ewald (PME) method. The simulation package GROMACS 4.5.3 [303] was used to carry out the simulations.

The simulations for bulk water were conducted on a sample of 500 SPC/E water molecules, with simulations conditions identical to the one of the lysozyme–trehalose–water–counterions system, where applicable.

9.3 Dynamics of water

To study the dynamical behavior of water in the lysozyme–trehalose aqueous solution, we calculated for water oxygens the dynamical structure factor, $F_S(q,t)$, which is the spatial Fourier transform of the tag-particle density autocorrelation function defined as

$$F_S(q,t) = \frac{1}{N}\left\langle \sum_{i=1}^{N} \exp\left[i\overrightarrow{q}\cdot(\overrightarrow{r}(t) - \overrightarrow{r}(0))\right]\right\rangle, \tag{9.1}$$

where N denotes the number of atoms, $\overrightarrow{q}$ the transfer momentum, and $\overrightarrow{r}_i(t)$ the position of atom i at time t. The brackets $\langle\cdots\rangle$ stand for the average over all time origins.

The oxygen $F_S(q,t)$ for bulk water shows a two-step relaxation behavior, a fast one corresponding to the initial ballistic regime leading to the rattling in the cage, and a slow one corresponding to the relaxing cage time region and referred to as α relaxation region. It was proposed and verified by simulations that the $F_S(q,t)$ for supercooled water can be well-described by the equation [304, 305]:

$$F_S(q_{\max},t) = (1 - f_{q_{\max}})\exp\left[-\left(\frac{t}{\tau_{\text{short}}}\right)^2\right] + f_{q_{\max}}\exp\left[-\left(\frac{t}{\tau_\alpha}\right)^{\beta_\alpha}\right] \tag{9.2}$$

where $q_{\max}$ is the peak of the structure factor. The Gaussian form takes into account the initial fast relaxation of the particle trapped in the cage. $f_{q_{\max}}$ is the Debye-Waller factor related to the cage. The stretched exponential is the functional form connected to the cage relaxation typical of glass formers.

For temperatures $T = 300$ K, 280 K, and 260 K, we compare in Fig. 9.1 the $F_S(q_{\max},t)$ of the oxygen atoms of water molecules in the lysozyme–trehalose aqueous solution at the peak of the oxygen–oxygen static structure factor with that of the bulk water. In the insets, we emphasize the changes in $F_S(q_{\max},t)$ with temperature in bulk water and in the lysozyme–trehalose aqueous solution.

It can be observed that whereas the fits of $F_S(q_{\max},t)$ for bulk water are consistent with eq.(9.2), for water in the presence of trehalose in lysozyme–trehalose aqueous solution, already at ambient temperature, the correlator shows an additional tail at long times, which does not allow to fit $F_S(q_{\max},t)$ with the eq.(9.2). The dynamics slows down dramatically and a two-step process is seen. Computational and experimental results have found that hydration water, that is, water in direct contact with biological molecules like proteins, shows strong differences in the dynamics with respect to the bulk [130]. It was shown by Magno and Gallo [220] that the tail appearing in the correlator of the aqueous solutions comes from hydration water, and they proposed a new relation to fit the $F_S(q_{\max},t)$ that

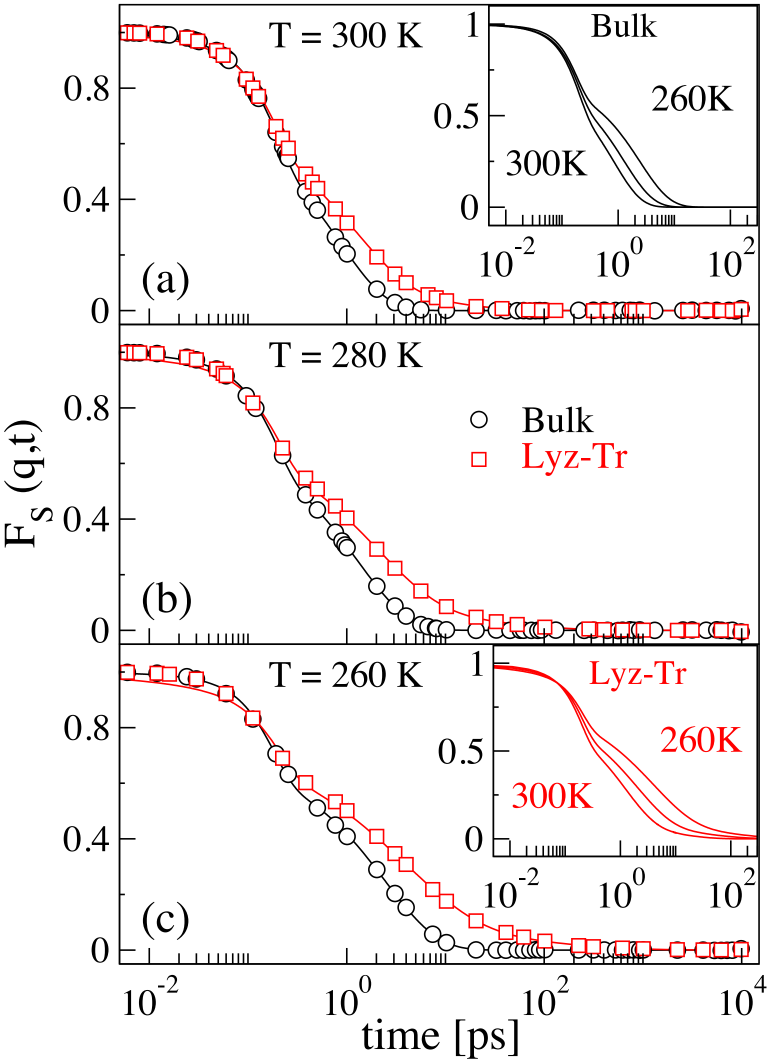

Figure 9.1: Self-intermediate scattering function $F_S(q_{\max}, t)$ of the oxygen atoms of bulk water, “Bulk”, (black circles) and of water in the aqueous solution of lysozyme in the presence of trehalose, “Lyz-Tr”, (red squares) at the peak of the oxygen–oxygen structure factor $q = 2.25$ Å^{-1}, for $T = 300$ K (a), 280 K (b), and 260 K (c). Black lines are fits to eq.(9.2), red lines are fits to eq.(9.3), only few of the simulated data points (symbols) are shown for clarity. The tails of the correlators calculated for water in the lysozyme–trehalose aqueous solution indicate the presence of an additional slower relaxation with respect to the bulk. Insets: For temperatures $T = 300$ K, 280 K, and 260 K, (top) fits to eq.(9.2) show changes in $F_S(q_{\max}, t)$ with temperature for bulk water, “Bulk”, (black lines); (bottom) fits to eq.(9.3) show changes in $F_S(q_{\max}, t)$ with temperature for water in the aqueous solution of lysozyme and trehalose, “Lyz-Tr”, (red lines).

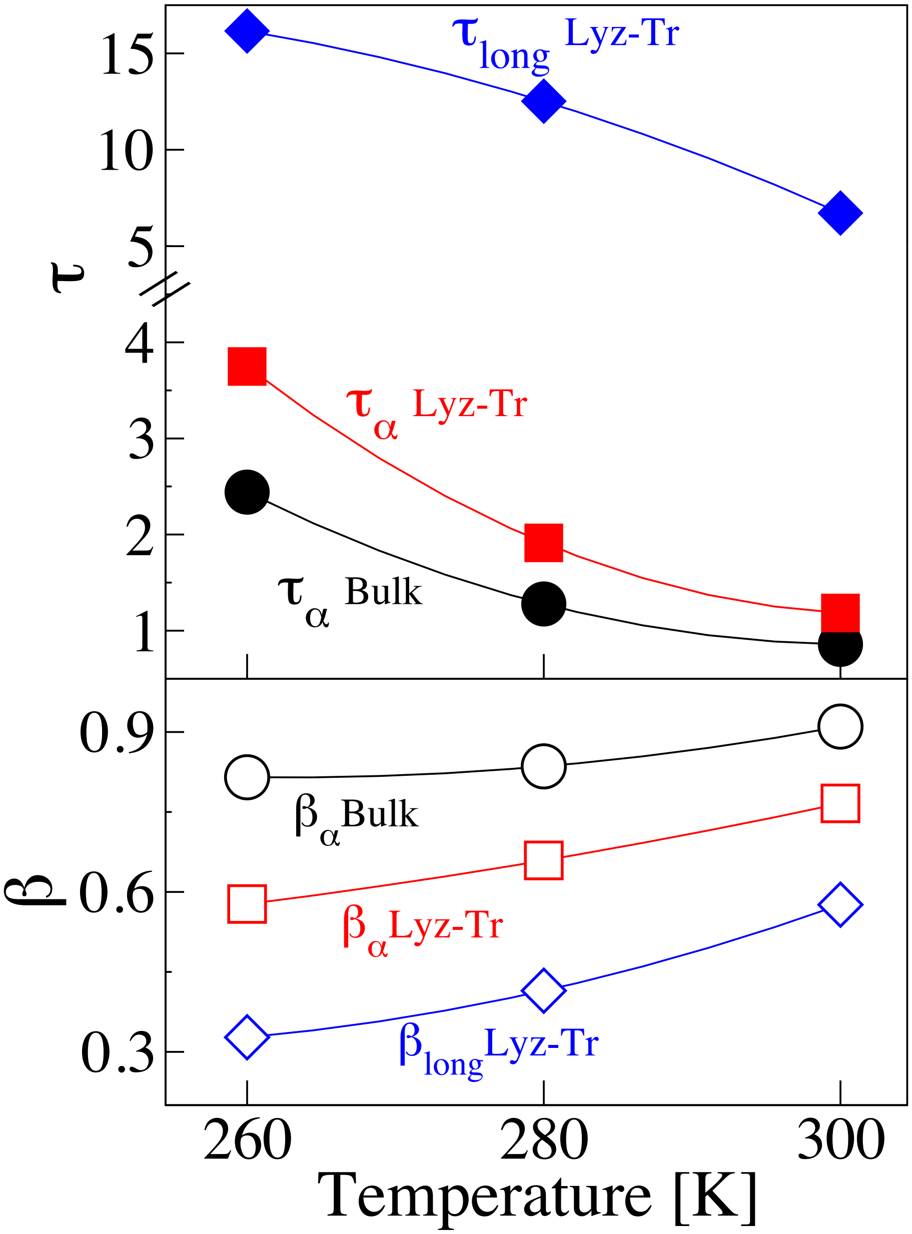

Figure 9.2: Top: relaxation times τ_α for α-relaxation, and τ_{long} for long-relaxation. Bulk water, "Bulk", (black solid circles) shows only α-relaxation, while water in the lysozyme–trehalose aqueous solution, "Lyz-Tr", shows both τ_α (red solid squares) and τ_{long} (blue solid diamonds). Bottom: β_α and β_{long} stretching parameters. Bulk water, "Bulk", (black empty circles) has only β_α stretching parameter, while water in lysozyme–trehalose aqueous solution, "Lyz-Tr", has both β_α (red empty squares) and β_{long} (blue empty diamonds). Lines are guides for the eyes.

implies two very well distinct dynamic behavior for water close to the biomolecules and the remaining water:

$$F_S(q_{\max}, t) = \left(1 - f_{q_{\max}} - f'_{q_{\max}}\right) \exp\left[-\left(\frac{t}{\tau_{\text{short}}}\right)^2\right]$$
$$+ \quad f_{q_{\max}} \exp\left[-\left(\frac{t}{\tau_\alpha}\right)^{\beta_\alpha}\right] \quad + \quad f'_{q_{\max}} \exp\left[-\left(\frac{t}{\tau_{\text{long}}}\right)^{\beta_{\text{long}}}\right]. \tag{9.3}$$

In this equation, in addition to the Gaussian relaxation at short times, there are two distinct Kohlrausch-William-Watts (KWW) functions. The first one corresponds to the α relaxation of the systems and origins from the bulk-like water molecules that are not in direct contact with the sugars. The second stretched exponential function accounts for the much slower dynamical behavior of hydration water molecules. We see in Fig. 9.1 that this functional form is able to reproduce perfectly the shape of the $F_S(q_{max}, t)$ of the water molecules in lysozyme–trehalose aqueous solutions. From the fits, we extracted the α relaxation time τ_α and the relaxation time of the hydration water molecules τ_{long} and the respective stretching parameters. The α-relaxation times of pure water are also given for comparison.

We present in Fig. 9.2, the temperature dependence of the relaxation times τ_α and τ_{long} and of the stretching parameters β_α and β_{long} for the bulk water and water in the aqueous solution of lysozyme in the presence of trehalose.

The above results indicate that water in aqueous solution of lysozyme in the presence of trehalose can be maintained in a slow–dynamics regime at higher temperatures. Therefore, upon a temperature change, trehalose protects earlier biomolecules by reducing their conformational relaxations.

To study the dynamical behavior of water at some distance away from the surface of trehalose or lysozyme, we define the following hydration shells. Water that forms hydrogen bonds with the lysozyme or the trehalose is defined as the first hydration shell, I, with a maximum distance of 3.4 Å away from the protein or sugar surface and *donor–H–acceptor* angle greater than 120°. The next hydration layer of water around trehalose, II, is defined at distance of 5.8 Å.

We then calculate the $F_S(q_{max}, t)$ for water excluding the first I^* and the second II^* hydration shells and observe that it is enough to exclude only I^* to find the long time tail disappearing in the $F_S(q_{max}, t)$, Fig.9.3. We observe that as we progressively exclude water layers close to the trehalose surface, water dynamics become bulk-like and can be fitted with eq.(9.2). We conclude that the dynamic properties of noninterfacial water are similar to those of the bulk. This is analogous to what is found for water close to hydrophilic surfaces where a bulk-like behavior is recovered once the water closest to the surface is excluded [168, 306, 307]. These findings confirm the hypothesis that the bioprotecting functions of disaccharides are connected to their ability to maintain a favorable environment for water in contact with biomolecules also despite the lowering temperature or water content [294].

It is interesting to note that when we exclude the first hydration shell of water I^* around the lysozyme, we find that water dynamics are not dramatically changed in comparison to the total unexcluded water behavior in the lysozyme–trehalose aqueous solution, Fig.9.4.

9.4 Residence Times

Water residence times could provide useful insights into the structural and dynamical behavior of water in the first, or successive, hydration shells of protein or sugar atoms exposed to the solvent [308].

At a given molecule (protein or sugar), $C(t)$ is defined in terms of a binary function $p_i(t, t' + t; t_0)$ that takes the value of 1 if the i^{th} water molecule stays in the coordination shell from the time origin t' to time $t'+t$ without getting out, in the interim, of this interval, (except for a short interval of time t_0) and takes the value of zero otherwise. Formally,

$$C(t) = \sum_{i=1}^{N} \frac{1}{t_{\text{run}} - t} \sum_{t'=0}^{t_{run}-t} p_i(t, t' + t; t_0) \tag{9.4}$$

where N is the total number of water molecules in the system and t_{run} is the length of the simulation time; $C(t)$ gives the average fraction of water molecules that still remain in the coordination shell after a time t.

The relaxation trend of the $C(t)$ provides information about the local dynamics of

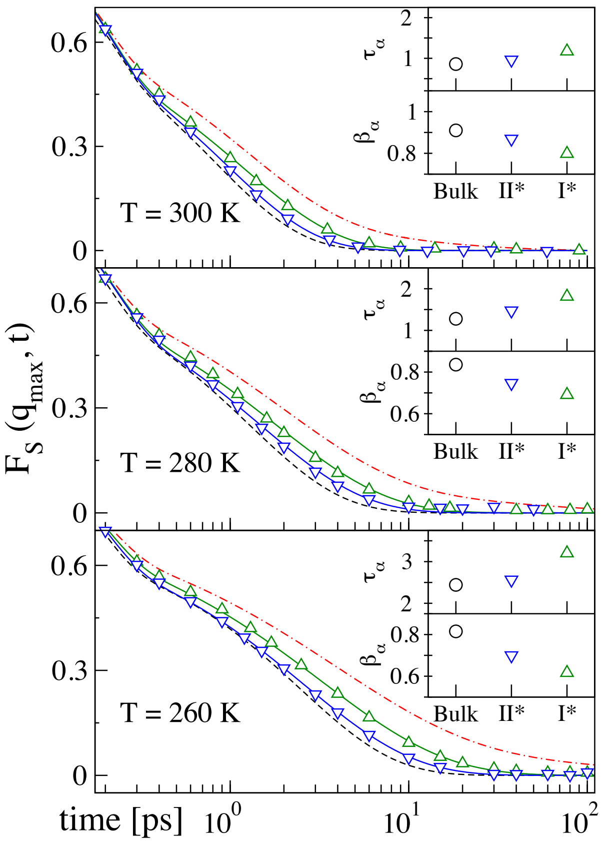

Figure 9.3: $F_S(q_{max}, t)$ for water with progressive exclusion of first hydration layer, $I*$, (green triangles up), and then second hydration layer, $II*$, (blue triangles down) around trehalose in the lysozyme–trehalose aqueous solution show approach to the relaxation found in the bulk water (black dashed line reploted from Fig.9.1) for all investigated temperatures $T = 300$ K (top), $T = 280$ K (middle) and $T = 260$ K. Only few of the simulated data points (symbols) are shown for clarity. Solid lines (blue and green) and dashed line (black) are fits to eq.(9.2) for water with excluded $I*$ and $II*$ shells, and bulk water respectively. Dash-dotted lines (red) are fits to eq.(9.3) for all water in the lysozyme–trehalose aqueous solution (reploted from Fig.9.1). Therefore, the long time tails of the total correlator of the solution shown in the Fig. 9.1 come only from water hydrogen bonded to the disaccharides. Symbols in insets: (top) α-relaxation, τ_α, times for water in bulk, "Bulk", and in aqueous solution of lysozyme and trehalose excluding first $I*$ and second $II*$ hydration layers around trehalose. (bottom) β_α stretching parameters for water in bulk, "Bulk", and in aqueous solution of lysozyme in the presence of trehalose excluding first $I*$ and second $II*$ hydration layers around trehalose.

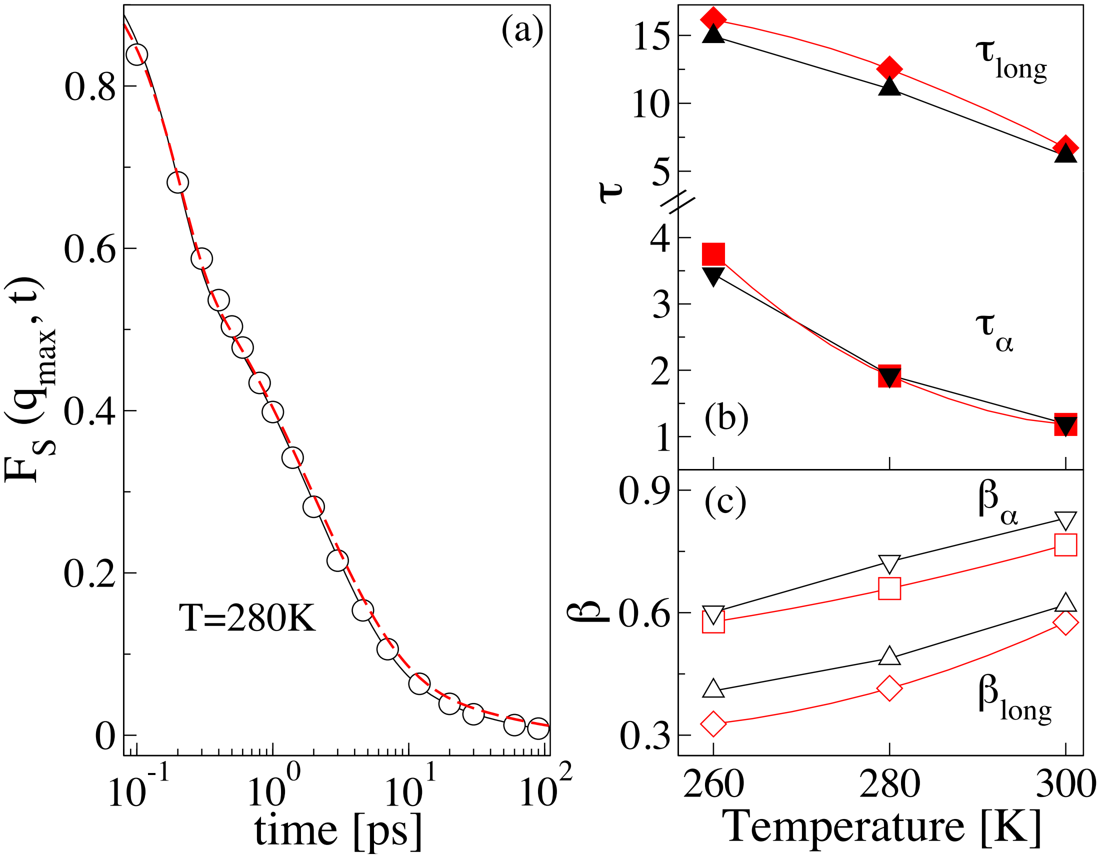

Figure 9.4: (a) $F_S(q_{max}, t)$ for water excluding first layer, I^*, close to the lysozyme surface at $T = 280$ K (black open circles). Only few of the simulated data points (symbols) are shown for clarity. Fits to eq.(9.3) for total water (red dashed line reploted from Fig.9.1) and water excluding I^* around lysozyme (black solid line) in the lysozyme–trehalose aqueous solution are also presented. Similar behavior is found for $T = 300$ K and $T = 260$ K (not shown). (b) α-relaxation τ_α and long-relaxation τ_{long} times for total water in aqueous solution of lysozyme in the presence of trehalose (red filled symbols) and in water excluding the first I^* hydration layer around lysozyme in the presence of trehalose (black filled symbols). (c) β_α and β_{long} stretching parameters for total water in aqueous solution of lysozyme in the presence of trehalose (red empty symbols) and in water excluding the first I^* hydration layer around lysozyme in the presence of trehalose (black empty symbols). Lines in (b) and (c) are guides for the eyes.

hydration water. The survival time correlation functions of water in the proximity of the protein or sugar surface [310] is usually fitted with a KWW function:

$$C(t) = A \cdot \exp\left[-\left(\frac{t}{\tau_{\mathrm{R}}}\right)^{\beta_{\mathrm{R}}}\right] \tag{9.5}$$

where τ_{R} provides the time scale over which the process evolves and gives an estimate of the residence time of water in the considered solvent layer; the stretching parameter β_{R} is a signature of the nonexponential trend of the phenomenon.

We were able to fit $C(t)$ with the eq. (9.5) for water in the second hydration layer around the trehalose Fig.9.5. However, two distinct KWW were required to fit water in the first hydration shell of both trehalose and lysozyme:

$$C(t) = (1-A) \cdot \exp\left[-\left(\frac{t}{\tau'_{\mathrm{R}}}\right)^{\beta'_{\mathrm{R}}}\right] + A \cdot \exp\left[-\left(\frac{t}{\tau''_{\mathrm{R}}}\right)^{\beta''_{\mathrm{R}}}\right] \tag{9.6}$$

where τ'_{R} and τ''_{R} are a short and a long time decay constants, respectively. These decays correspond to solvent molecules that stay in the hydration shell for prolonged periods of time or enter and then immediately leave [309, 311, 312].

Stretched exponential functions are commonly used to describe the relaxation in amorphous, disordered systems, we can then relate the above-reported behavior for the survival distribution function with an additional phenomenological indication of the glassy character of hydration water.

9.5 Radial distribution

The structural organization of water at the protein interface can be described by the protein–solvent radial distribution function $g(r)$ representing the relative probability of finding any solvent molecule whose oxygen is at a distance r from a specific solute atom. We measure $g(r)_{Lyz-W}$ of water and $g(r)_{Lyz-Tr}$ trehalose around the center of mass of the lysozyme.

From Fig.9.6 we observe that aqueous solution of trehalose is distributed very close to the surface of the lysozyme. We also notice that as the temperature decreases to $T = 260$ K, there is an increase in both water and trehalose at the protein surface.

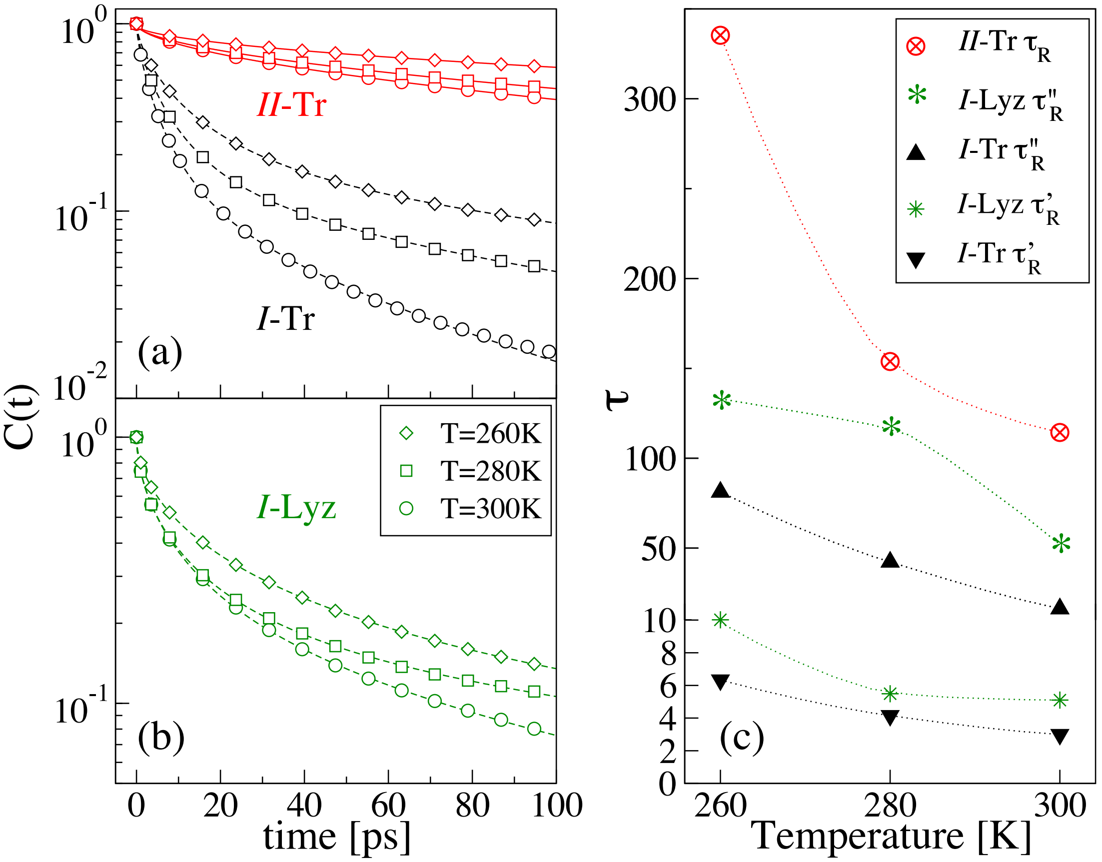

Figure 9.5: Semi-log plot of the survival time correlation function $C(t)$ of (a) water in the first I (black empty symbols) and second II (red empty symbols) layers around trehalose labeled "I-Tr" and "II-Tr" respectively; (b) water in the I layer around lyzosyme (green empty symbols labeled "I-Lyz"). Only few simulated data points (symbols) are shown for clarity. The red solid lines (a) are the fitting curves obtained by eq.(9.5) for simulated data points inside the II layer around trehalose, II-Tr; black (a) and green (b) dashed lines are the fitting curves obtained by eq.(9.6) for I layer around trehalose (I-Tr) and lysozyme (I-Lyz) respectively. (c) τ'_{R} and τ''_{R} times are short and long decay constants respectively for all water in the first I hydration layer around lysozyme (green stars) and trehalose (black filled triangles). Decay constant τ_{R} for water in the second II hydration layer around trehalose (red crossed circle). Dotted lines are guides for the eyes.

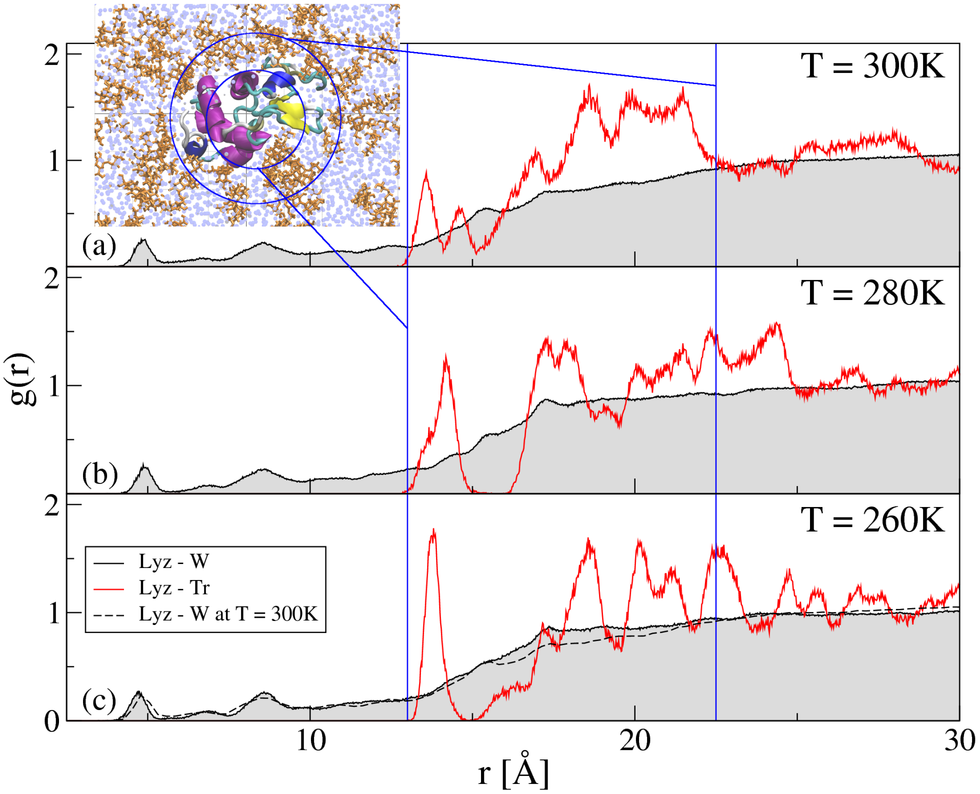

Figure 9.6: Radial distribution functions $g(r)_{Lyz-W}$ of water (black lines with gray shading to baseline) and $g(r)_{Lyz-Tr}$ trehalose (red lines) around the center of mass of the lysozyme. We present three investigated temperatures $T = 300$ K (top), $T = 280$ K (middle), $T = 260$ K (bottom). Blue vertical lines mark the minor and major radii of an approximately elliptical shape of the lysozyme. Inset: pictorial representation of the 2 nm × 6 nm × 8 nm cut of the simulation box of aqueous solution of lysozyme (colorful cartoon representation), trehalose molecules (orange segments), and water molecules (blue spheres). Blue circles mark the minor and major radii of lysozyme respectively.

In addition in Fig.9.7, we present 2 nm layer of the simulation box at $T = 300$ K with the following dimensions 2 nm × 6 nm × 8 nm in three dimensions looking down the x, y, and z axes respectively. Together with the radial distribution function, Fig.9.7, suggests that the aqueous solution of trehalose with very slow dynamics of water (as we shoved earlier) surrounds the lysozyme. Thus we support the hypotheses of the inhibition of protein motion due to the vitrification upon cooling, "insect in amber" as proposed by Green and Angell [293].

9.6 Conclusion

In summary, we have shown that water slow dynamics in the presence of disaccharides such as trehalose shows two different well distinct relaxation processes, a faster one that shows bulk-like features due to noninterfacial water and a slower one characterizing the dynamical properties of hydration water molecules. This well-distinct dynamic differentiation has recently been observed through light scattering [313, 314] and Fourier transform infrared spectroscopy [315] experiments on trehalose aqueous solutions.

This work supports the hypothesis that trehalose has effect in "destructuring" the network of water and in slowing down its dynamics around the lysozyme, as was previously reported by [295].

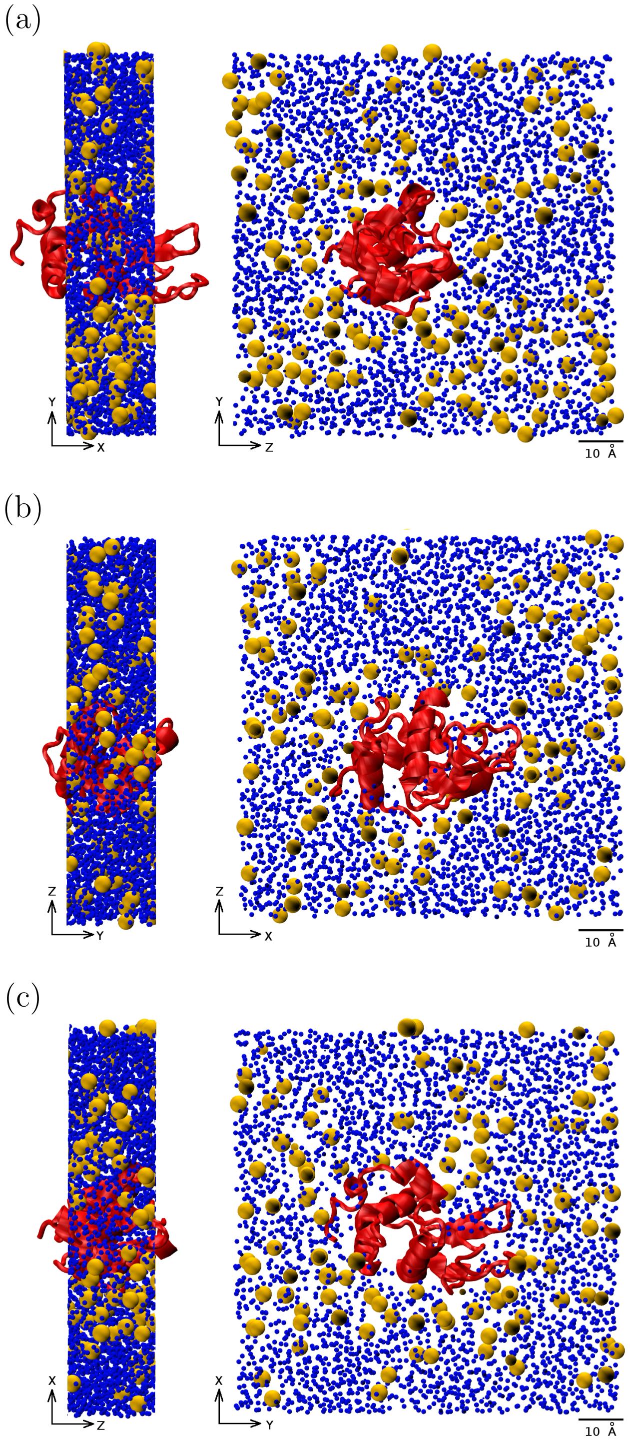

Figure 9.7: Visualization of lysozyme–trehalose aqueous solution layer of thickness 2 nm at T = 300 K with the following dimensions 2 nm × 6 nm × 8 nm in three dimensions looking down the x (a), y (b), and z (z) axes respectively. Lysozyme is visualized in red cartoon, trehalose in yellow spheres, and water in blue spheres.

Bibliography

[1] M. Chaplin, http://www.lsbu.ac.uk/ .

[2] G. W. Robinson, S.-B. Zhu, S. Singh, M. W. Evans, *Water in Biology, Chemistry, and Physics: Experimental Overviews and Computational Methodologies*, World Scientific, Singapore (1996).

[3] M.-C. Bellissent-Funel, *Hydration Processes in Biology: Theoretical and Experimental Approaches*, IOS Press, Amsterdam, (1999).

[4] P. Ball, *H2O - A biography of water*, Phoenix, London, (2000).

[5] Americal Museum of Natural History, *W*ater: H2O=Life, http://www.amnh.org/exhibitions/water/

[6] R. Waller, *Essayes of natural experiments* (English translation from Italian by the Secretary of the Academie del Cimento), Johnson Reprint Corporation, New York, (1964).

[7] *Handbook of Chemistry and Physics*, 92nd edition, (2011-2012)

[8] *NIST Chemistry WebBook*, http://webbook.nist.gov/chemistry/fluid/

[9] C. A. Angell, J. Shuppert, J. C. Tucker, The Journal of Physical Chemistry **77**, 3092 (1973).

[10] H. E. Stanley, *Introduction to phase transitions and critical phenomena*, Oxford University Press, New York, (1971).

[11] H. E. Stanley, S. V. Buldyrev, M. Canpolat, O. Mishima, M. R. Sadr-Lahijany, A. Scala, and F. W. Starr, Physical Chemistry Chemical Physics **2**, 1551 (2000).

[12] H. Kanno, R. J. Speedy and C. A. Angell, Science **189**, 880 (1975).

[13] M. D. Ediger, C. A. Angell, and S. R. Nagel, Journal of Physical Chemistry **100**, 13200 (1996).

[14] C. A. Angell, Chemical Reviews **102**, 2627 (2002).

[15] V. Velikov, S. Borick, and C. A. Angell, Science **294**, 2335 (2001).

[16] K. Winkel, M. S. Elsaesser, E. Mayer and T. Loerting, Journal of Physical Chemistry **128**, 044510 (2008).

[17] F. Sciortino, E. La Nave, P. Tartaglia, Physical Review Letters **91**, 155701 (2003).

[18] F. Sciortino, P. H. Poole, U. Essmann, H. E. Stanley, Physical Review E **55**, 727 (1997).

[19] S. Maruyama, K. Wakabayashi, M. Oguni, American Institue of Physics Conference Proceedings **708**, 675 (2004).

[20] A. K. Soper, M. A. Ricci, M. G. Sceats, The Journal of Chemical Physics **69**, 3468 (2000).

[21] M. C. Bellissent-Funel, M. V. Krongauz, The Journal of Chemical Physics **102**, 2881 (1995).

[22] J. M. Zanotti, M. C. Bellissent-Funel, S,-H. Chen, Europhysics Letters **71**, 91 (2005).

[23] G. E. Walrafen, M. S. Hokmababi, W. H. Yang, The journal of Chemical Physics **85**, 6964 (1986).

[24] G. Franzese and M. Rubi, *Aspects of Physical Biology: Biological Water, Protein Solutions, Transport and Replication*, Springer, Berlin, 2008.

[25] P. G. Debenedetti, Journal of Physics: Condensed Matter **15**, R1669 (2003).

[26] P. G. Debenedetti and H. E. Stanley, Physics Today **56**, 40 (2003).

[27] G. Franzese, K. Stokely, X.-q. Chu, P .Kumar, M. G. Mazza, S.-H. Chen, and H. E. Stanley, Journal of Physics: Condensed Matter **20**, 494210 (2008).

[28] C. A. Angell, Science **319**, 582 (2008).

[29] H. E. Stanley, P. Kumar, G. Franzese, L. Xu, Z. Yan, M. G. Mazza, S.-H. Chen, F. Mallamace, S. V. Buldyrev, *Liquid polyamorphism: Some unsolved puzzles of water in bulk, nanoconfined, and biological environments*, in *AIP Conference Proceedings*, volume 982, page 251, M. Tokuyama, I. Oppenheim, and H. Nishiyama, eds. AIP Conference Proceedings, 2008.

[30] H. E. Stanley, S. V. Buldyrev, G. Franzese, N. Giovambattista, F. W. Starr, Philosophical Transactions of the Royal Society A: Mathematical, Physical, and Engineering Sciences **363**, 509 (2005).

[31] P. Kumar, G. Franzese, S. V. Buldyrev, and H. E. Stanley, Physical Review E **73**, 041505 (2006).

[32] P. Kumar, G. Franzese and H. E. Stanley, Physical Review Letters **100**, 105701 (2008).

[33] U. Wolff, Physical Review Letters **62**, 361 (1989).

[34] G. Franzese and H. E. Stanley, Journal of Physics: Condensed Matter **14**, 2201 (2002).

[35] G. Franzese and H. E. Stanley, Physica A **314**, 508 (2002).

[36] K. Stokely, M. G. Mazza, H. E. Stanley, G. Franzese, Proceedings of the National Academy of Sciences of the United States of America **107**, 1301 (2010).

[37] G. Franzese and H. E. Stanley, Journal of Physics: Condensed Matter **19**, 205126 (2007).

[38] P. Kumar, G. Franzese and H. E. Stanley, Journal of Physics: Condensed Matter **20**, 244114 (2008).

[39] G. Franzese, M. I. Marqués, and H. E. Stanley, Physical Review E **67**, 011103 (2003).

[40] M. I. Marqués, Physical Review E **76**, 021503 (2007).

[41] M. Ricci, F. Bruni, and A. Giuliani Faraday Discussion **141**, 347 (2009).

[42] M. F. Chaplin, Water's hydrogen bond strength, in *Water of Life: Counterfactual Chemistry and Fine-Tuning in Biochemistry*, ed. R. M. Lynden-Bell, S. C. Morris, J. D. Barrow, J. L. Finney, and C. L. Harper, Jr. CRC Press, Boca Raton ppage 69-86 (2010).

[43] V. Cataudella, G. Franzese, M. Nicodemi, A. Scala, and A. Coniglio, Physical Review E **54**, 175 (1996).

[44] G. Franzese, Journal of Physics A **29**, 7367 (1996) .

[45] A. Coniglio and F. Peruggi, Journal of Physics A **15**, 1873 (1982).

[46] M. G. Mazza, K. Stokely, S. E. Pagnotta, F. Bruni, H. E. Stanley, and G. Franzese, Proceedings of the National Academy of Sciences of the United States of America **108**, 19873 (2011).

[47] M. G. Mazza, N. Giovambattista, F. W. Starr, and H. E. Stanley, Physical Review Letters **96**, 057803 (2006).

[48] N. Giovambattista, M. G. Mazza, S. V. Buldyrev, F. W. Starr, and H. E. Stanley, The Journal of Physical Chemistry B **108**, 6655 (2004).

[49] M. G. Mazza, N. Giovambattista, H. E. Stanley, and F. W. Starr, Physical Review E **76**, 031203 (2007).

[50] A. Oleinikova, I. Brovchenko, Journal of Physics: Condensed Matter **18**, S2247 (2006).

[51] C. A. Angell and J. C. Tucker, Science **181**, 342 (1973).

[52] R. J. Speedy and C. A. Angell, The Journal of Chemical Physics **65**, 851 1976.

[53] D. E. Hare and C. M. Sorensen, The Journal of Chemical Physics **84**, 5085 (1986).

[54] P. G. Debenedetti, *Metastable Liquids. Concepts and Principles*, Princeton University Press, Princeton NJ, 1996.

[55] C. G. Salzmann, P. G. Radaelli, E. Mayer, and J. L. Finney, Physical Review Letters **103**, 105701 (2009).

[56] P. Bruggeller and E. Mayer, Nature **288**, 569 (1980).

[57] P. Jenniskens and D. Blake, Science **265**, 753 (1994).

[58] O. Mishima, L. Calvert, and E. Whalley, Nature **314**, 76 (1985).

[59] G. Strazzulla, G. A. Baratta, G. Leto, and G. Foti, Europhysics Letters **18**, 517 (1992).

[60] T. Loerting and N. Giovambattista, Journal of Physics: Condensed Matter **18**, R919 (2006).

[61] E. F. Burton and W. F. Oliver, Proceedings of the Royal Society of London A **153**, 166 (1935).

[62] O. Mishima, L. Calvert, and E. Whalley, Nature **310**, 393 (1984).

[63] T. Loerting, C. Salzmann, I. Kohl, E. Mayer, and A. Hallbrucker, Physical Chemistry Chemical Physics **3**, 5355 (2001).

[64] A. Soper and M. Ricci, Physical Review Letters **84**, 2881 (2000).

[65] R. J. Speedy, The Journal of Physical Chemistry **86**, 3002 (1982).

[66] P. Poole, F. Sciortino, U. Essmann, and H. E. Stanley, Nature **360**, 324 (1992).

[67] H. Tanaka, Nature **380**, 328 (1996).

[68] S. Sastry, P. G. Debenedetti, F. Sciortino, and H. E. Stanley, Physical Review E **53**, 6144 (1996).

[69] F. Mallamace, C. Branca, M. Broccio, C. Corsaro, C.-Y. Mou, and S.-H. Chen, Proceedings of the National Academy of Sciences of the United States of America **104**, 18387 (2007).

[70] S. Granick and S. C. Bae, Science **322**, 1477 (2008).

[71] A. Faraone, K.-H. Liu, C.-Y. Mou, Y. Zhang, and S.-H. Chen, Journal Of Chemical Physics **130**, 134512 (2009).

[72] A. K. Soper, Molecular Physics **106**, 2053 (2008).

[73] M. C. Bellissent-Funel, Journal of Physics: Condensed Matter **20**, 244120 (2008).

[74] M. Vogel, Physical Review Letters **101**, 225701 (2008).

[75] S. Pawlus, S. Khodadadi, and A. P. Sokolov, Physical Review Letters **100**, 108103 (2008).

[76] S.-H. Chen, L. Liu, E. Fratini, P. Baglioni, A. Faraone, and E. Mamontov, Proceedings of the National Academy of Sciences of the United States of America **103**, 9012 (2006).

[77] D. Chandler, Nature **437**, 640 (2005).

[78] K. A. Dill, T. M. Truskett, V. Vlachy, and B. Hribar-Lee, Annual Review of Biophysics and Biomolecular Structure **34**, 173 (2005).

[79] N. Giovambattista, C. F. Lopez, P. J. Rossky, and P. G. Debenedetti Proceedings of the National Academy of Sciences of the United States of America **105**, 2274 (2008).

[80] P. Gallo and M. Rovere, Physical Review E **76**, 061202 (2007).

[81] M. C. Bellissent-Funel, S.-H. Chen, and J. M. Zanotti, Physical Review E **51**, 4558 (1995).

[82] S. Takahara, M. Nakano, S. Kittaka, Y. Kuroda, T. Mori, H. Hamano, and T. Yamaguchi, The Journal of Physical Chemistry B **103**, 5814 (1999).

[83] A. Faraone, L. Liu, C.-Y. Mou, P. C. Shih, J. R. D. Copley, and S.-H. Chen, The Journal of Chemical Physics **119**, 3963 (2003).

[84] S.-H. Chen, F. Mallamace, C.-Y. Mou, M. Broccio, C. Corsaro, A. Faraone, and L. Liu, Proceedings of the National Academy of Sciences of the United States of America **103**, 12974 (2006).

[85] V. Crupi, D. Majolino, P. Migliardo, and V. Venuti, The Journal of Physical Chemistry B **106**, 10884 (2002).

[86] V. Crupi, D. Majolino, P. Migliardo, V. Venuti, U. Wanderlingh, T. Mizota, and M. Telling, The Journal of Physical Chemistry B **108**, 4314 (2004).

[87] X.-q. Chu, A. I. Kolesnikov, A. P. Moravsky, V. Garcia-Sakai, and S.-H. Chen, Physical Review E **76**, 021505 (2007).

[88] A. Faraone, L. Liu, C.-Y. Mou, C. W. Yen, and S.-H. Chen, The Journal of Chemical Physics **121**, 10843 (2004).

[89] F. Mallamace, M. Broccio, C. Corsaro, A. Faraone, U. Wanderlingh, L. Liu, C.-Y. Mou, and S.-H. Chen, The Journal of Chemical Physics **124**, 161102 (2006).

[90] L. Liu, S.-H. Chen, A. Faraone, C. W. Yen, and C.-Y. Mou, Physical Review Letters **95**, 117802 (2005).

[91] S.-H. Chen, L. Liu, X.-q. Chu, Y. Zhang, E. Fratini, P. Baglioni, A. Faraone, and E. Mamontov, The Journal of Chemical Physics **125**, 171103 (2006).

[92] X.-q. Chu, E. Fratini, P. Baglioni, A. Faraone, and S.-H. Chen, Physical Review E **77**, 011908 (2008).

[93] S. Cerveny, J. Colmenero, and A. Alegría, Physical Review Letters **97**, 189802 (2006).

[94] H. Jansson and J. Swenson, The European Physical Journal E: Soft Matter and Biological Physics **12**, 51 (2003).

[95] S. Sudo, S. Tsubotani, M. Shimomura, N. Shinyashiki, and S. Yagihara, The Journal of Chemical Physics **121**, 7332 (2004).

[96] S. Cerveny, G. A. Schwartz, A. Alegría, R. Bergman, and J. Swenson, The Journal of Chemical Physics **124**, 194501 (2006).

[97] J. Swenson, Physical Review Letters **97**, 189801 (2006).

[98] J. Swenson, H. Jansson, and R. Bergman, *Aspects Of Physical Biology: Biological Water, Protein Solutions, Transport And Replication*, Springer, Berlin, page 23, G. Franzese and M. Rubi, eds., 2008.

[99] S. Khodadadi, S. Pawlus, J. H. Roh, V. G. Sakai, E. Mamontov, and A. P. Sokolov, The Journal Of Chemical Physics **128**, 195106 (2008).

[100] L. Xu, P. Kumar, S. V. Buldyrev, S.-H. Chen, P. H. Poole, F. Sciortino, and H. E. Stanley, Proceedings of the National Academy of Sciences of the United States of America **102**, 16558 (2005).

[101] P. Kumar, Z. Yan, L. Xu, M. G. Mazza, S. V. Buldyrev, S.-H. Chen, S. Sastry, and H. E. Stanley, Physical Review Letters **97**, 177802 (2006).

[102] M. Lagi, X.-q. Chu, C. Kim, F. Mallamace, P. Baglioni, and S.-H. Chen, The Journal of Physical Chemistry B **112**, 1571 (2008).

[103] S. Cerveny, G. A. Schwartz, R. Bergman, and J. Swenson, Physical Review Letters **93**, 245702 (2004).

[104] P. Kumar, F. W. Starr, S. V. Buldyrev, and H. E. Stanley, Physical Review E **75**, 011202 (2007).

[105] B. Guillot, Journal of Molecular Liquids **101**, 219 (2002).

[106] G. Lamoureux, D. Alexander, J. MacKerell, and B. Roux, The Journal of Chemical Physics **119**, 5185 (2003).

[107] P. K. Mankoo and T. Keyes, The Journal of Chemical Physics **129**, 034504 (2008).

[108] J. P. Piquemal, R. Chelli, P. Procacci, and N. Gresh, The Journal of Physical Chemistry A **111**, 8170 (2007).

[109] J. Teixeira and M. C. Bellissent-Funel, Journal of Physics: Condensed Matter **2**, SA105 (1990).

[110] A. Luzar and D. Chandler, Physical Review Letters **76**, 928 (1996).

[111] M. Henry, A European Journal of Chemical Physics and Physical Chemistry **3**, 561 (2002).

[112] A. Baranyai, A. Bartók, and A. A. Chialvo, The Journal of Chemical Physics **123**, 054502 (2005).

[113] J. D. Smith, C. D. Cappa, K. R. Wilson, B. M. Messer, R. C. Cohen, and R. J. Saykally, Science **306**, 851 (2004).

[114] S. J. Suresh and V. M. Naik, The Journal of Chemical Physics **113**, 9727 (2000).

[115] A. H. Narten, M. D. Danford, and H. A. Levy, Discussions of the Faraday Society **43**, 97 (1967).

[116] A. K. Soper and M. G. Phillips, Chemical Physics **107**, 47 (1986).

[117] K. Stokely, M. G. Mazza, H. E. Stanley, and G. Franzese, *Metastable Systems under Pressure*, Springer, chapter *Metastable Water Under Pressure*, pages 197–216, NATO Science for Peace and Security Series A: Chemistry and Biology, 2010.

[118] G. Franzese, M. Yamada, and H. E. Stanley, *Aip Conference Proceedings* volume 519, pages 281–287, 2000.

[119] G. Franzese and H. E. Stanley, *Science And Culture Series: Physics* volume 26, pages 210–214, 2005.

[120] P. Kumar, G. Franzese, S. V. Buldyrev, and H. E. Stanley *Aspects Of Physical Biology: Biological Water, Protein Solutions, Transport And Replication*, Springer, Berlin, page 3, G. Franzese and M. Rubi, eds., 2008.

[121] X.-q. Chu, A. Faraone, C. Kim, E. Fratini, P. Baglioni, J. B. Leao, and S.-H. Chen, The Journal of Physical Chemistry B **113**, 5001 (2009).

[122] M. G. Mazza, K. Stokely, E. G. Strekalova, H. E. Stanley, and G. Franzese, *Computer Physics Communications* **180**, 497 (2009).

[123] G. Franzese and F. de los Santos, Journal of Physics: Condensed Matter **21**, 504107 (2009).

[124] K. Koga, H. Tanaka, and X. C. Zeng, Nature **408**, 564 (2000).

[125] G. Franzese and A. Coniglio, Physical Review E **59**, 6409 (1999).

[126] F. de los Santos and G. Franzese, *Modeling And Simulation Of New Materials: Proceedings Of Modeling And Simulation Of New Materials: Tenth Granada Lectures*, in *AIP Conference Proceedings*, volume 1091, pages 185–197, J. Marro, P. L. Garrido, and P. I. Hurtado, eds. AIP Conference Proceedings, Granada, Spain, 2009.

[127] T. M. Truskett, P. G. Debenedetti, and S. Torquato, The Journal of Chemical Physics **114**, 2401 (2001).

[128] P. Kumar, S. V. Buldyrev, F. W. Starr, N. Giovambattista, and H. E. Stanley, Physical Review E **72**, 051503 (2005).

[129] E. G. Strekalova, M. G. Mazza, H. E. Stanley, and G. Franzese, Physical Review Letters **106**, 145701 (2011).

[130] P. Ball, Chemical Reviews **108**, 74 (2008).

[131] P. De Los Rios and G. Caldarelli, Physical Review E **62**, 8449 (2000).

[132] Y. Levy and J. N. Onuchic, Annual Review of Biophysics and Biomolecular Structure **35**, 389 (2006).

[133] C. L. Dias, T. Ala-Nissila, M. Karttunen, I. Vattulainen, and M. Grant, Physical Review Letters **100**, 118101 (2008).

[134] J. Swenson, H. Jansson, and R. Bergman, Physical Review Letters, **96**, 247802 (2006).

[135] D. Liu, Y. Zhang,C.-C. Chen, C.-Y. Mou, P. H. Poole, and S.-H. Chen, Proceedings of the National Academy of Sciences of the United States of America **104**, 9570 (2007).

[136] G. H. Findenegg, S. Jähnert, D. Akcakayiran, A. Schreiber, A European Journal of Chemical Physics and Physical Chemistry, **9**, 2651 (2008).

[137] R. Mancinelli, F. Bruni and M. A. Ricci, The Journal of Physical Chemistry Letters, **1**, 1277 (2010).

[138] M. Majumder, N. Chopra, R. Andrews, and B. J. Hinds, Nature **438**, 44 (2005).

[139] S. Joseph and N. R. Aluru, Physical Review Letters **101**, 064502 (2008).

[140] D. Paschek, The Journal of Chemical Physics **120**, 10605 (2004);

[141] Y. Liu, A. Z. Panagiotopoulos, and P. G. Debenedetti, The Journal of Chemical Physics **131**, 104508 (2009);

[142] J. L. F. Abascal and C. Vega, The Journal of Chemical Physics **133**, 234502 (2010).

[143] R. Kurita and H. Tanaka, Physical Review Letters **98**, 235701 (2007).

[144] P. G. De Sanctis Lucentini and G. Pellicane, Physical Review Letters **101**, 246101 (2008).

[145] T. Urbic, V. Vlachy, O. Pizio, K. A. Dill, Journal of Molecular Liquids **112**, 71 (2004).

[146] H. S. Frank and M. W. Evans, The Journal of Chemical Physics **13**, 507 (1945).

[147] K. A. T. Silverstein, A. D. J. Haymet, and K. A. Dill, The Journal of Chemical Physics **111**, 8000 (1999).

[148] F. H. Stillinger, Journal of Solution Chemistry **2**, 141 (1973).

[149] N. Muller, Accounts of Chemical Research **23**, 23 (1990).

[150] Y. Zhang, K.-H. Liu, M. Lagi, D. Liu, K. C. Littrell, C.-Y. Mou, and S.-H. Chen, The Journal of Physical Chemistry B **113**, 5007 (2009).

[151] B. A. Patel, P. G. Debenedetti, F. H. Stillinger, P. J. Rossky, Biophysical Journal **93**, 4116 (2007).

[152] K. Binder, Physical Review Letters **47** 693 (1981).

[153] G. Franzese and A. Coniglio, Physical Review E **58**, 2753 (1998).

[154] N. Huang, D. Nordlung, C. Huang, T. Tyliszczak, T. M. Weiss, Y. Acremann, L. G. M. Pettersson, A. Nilsson, The Journal of Chemical Physics. (under review).

[155] F. Mallamace, C. Branca, C. Corsaro, N. Leone, J. Spooren, S.-H. Chen, and H. E. Stanley, Proceedings of the National Academy of Sciences of the United States of America **107**, 22457 (2010).

[156] G. Franzese, A. Hernando-Martínez, P. Kumar, M. G. Mazza, K. Stokely, E. G. Strekalova, F. de los Santos, and H. E. Stanley, Journal of Physics: Condensed Matter **22**, 284103 (2010).

[157] S.-H. Chen and C.-K. Loong, Nuclear Engineering and Technology **38** 201 (2006).

[158] A. Lervik, F. Bresme, S. Kjelstrup, D. Bedeaux, and J. M. Rubi, Physical Chemistry Chemical Physics **12**, 1610 (2010).

[159] A. Lervik, F. Bresme, and S. Kjelstrup, Soft Matter **5**, 2407 (2009).

[160] F. Bresme, E. Chacón, P. Tarazona, and K. Tay, Physical Review Letters **101** 056102 (2008).

[161] F. Bresme, E. Chacón, and P. Tarazona, Physical Chemistry Chemical Physics **10**, 4704 (2008).

[162] D. Liu, Y. Zhang, Y. Liu, J. Wu,C.-C. Chen, C.-Y. Mou, and S.-H. Chen, The Journal of Physical Chemistry B **112**, 4309 (2008).

[163] F. Mallamace, M. Broccio, C. Corsaro, A. Faraone, L. Liu, C.-Y. Mou, and S.-H.Chen, Journal of Physics: Condensed Matter **18**, S2285 (2006).

[164] F. Mallamace, M. Broccio, C. Corsaro, A. Faraone, D. Majolino, V. Venuti, L. Liu, C.-Y. Mou, and S.-H. Chen, National Academy of Sciences of the United States of America **104**, 424 (2007).

[165] S. Han, P. Kumar, and H. E. Stanley, Physical Review E **77**, 030201(R) (2008).

[166] N. Giovambattista, P. J. Rossky, and P. G. Debenedetti, Physical Review E **73**, 041604 (2006).

[167] N. Giovambattista, P. G. Debenedetti, and P. J. Rossky, The Journal of Physical Chemistry B **111**, 9581 (2007).

[168] P. Gallo, M. Rovere, and S.-H. Chen, The Journal of Physical Chemistry Letters **1**, 729 (2010).

[169] O. Mishima and H. E. Stanley, Nature **396**, 329 (1998).

[170] P. H. Poole, U. Essmann, F. Sciortino, and H. E. Stanley, Physical Review E **48**, 4605 (1993).

[171] S. Harrington, P. H. Poole, F. Sciortino, and H. E. Stanley, Journal of Chemical Physics **107**, 7443 (1997).

[172] O. Mishima and H. E. Stanley, Nature **392**, 164 (1998).

[173] O. Mishima, The Journal of Chemical Physics **133**, 144503 (2010).

[174] F. Sciortino, P. Poole, H. E. Stanley, and S. Havlin, Physical Review Letters **64**, 1686 (1990).

[175] F. de los Santos and G. Franzese, The Journal of Physical Chemistry B **115**, 14311 (2011).

[176] P. H. Poole, I. Saika-Voivod, and F. Sciortino, Journal of Physics: Condensed Matter **17**, L431 (2005).

[177] J. L. F. Abascal and C. Vega, The Journal of Chemical Physics **123** 234505 (2005).

[178] D. T. Limmer and D. Chandler, The Journal of Chemical Physics **135** 134503 (2011).

[179] P. H. Poole, S. R. Becker, F. Sciortino, and F. W. Starr, The Journal of Physical Chemistry B **115** 14176 (2011).

[180] F. Sciortino, I. Saika-Voivod, and P. Poole, Physical Chemistry Chemical Physics **13** 19759 (2011).

[181] T. A. Kesselring, G. Franzese, S. V. Buldyrev, H. J. Herrmann, and H. E. Stanley, arXiv:1112.2186 (2011).

[182] P. G. Debenedetti, private communication (2011).

[183] D. Corradini, P. Gallo, and M. Rovere, The Journal of Chemical Physics **128**, 244508 (2008).

[184] M. E. Fisher and H. Nakanishi, The Journal of Chemical Physics **75** 5857 (1981).

[185] F. W. Starr, J. K. Nielsen, and H. E. Stanley, Physical Review Letters **82**, 2294 (1999).

[186] H. E. Stanley, Journal of Physics A **12**, L329 (1979).

[187] S. O. Yesylevskyy, L. V. Schäfer, D. Sengupta, and S. J. Marrink, PLoS Computational Biology **6**, e1000810 (2010).

[188] R. Zangi and A. E. Mark, Physical Review Letters **91**, 025502 (2003).

[189] A. M. Pendás, M. A. Blanco, E. Francisco, The Journal of Chemical Physics **125**, 184112 (2006).

[190] J. Israelachvili and R. Pashley, Nature **300**, 341 (1982).

[191] G. Cicero, J. C. Grossman, E. Schwegler, F. Gygi, and G. Galli, Journal of the American Chemical Society **130**, 1871 (2008).

[192] W. Doster and T. Gutberlet, Biochimica et Biophysica Acta **1804**, 3 (2010).

[193] B. Lee and G. Graziano, Journal of the American Chemical Society **118**, 5163 (1996).

[194] K. Vollmayr, J. D. Reger, M. Scheucher, K. Binder, Zeitschrift für Physik B **91**, 113 (1993).

[195] C. E. Bertrand and M. A. Anisimov, The Journal of Physical Chemistry B **115**, 14099 (2011).

[196] B. B. Machta, S. Papanikolaou, J. P. Sethna and S. L. Veatch, Biophysical Journal **100**, 1668 (2011).

[197] J. Ehrig, E. P. Petrov, and P. Schwille, New Journal of Physics **13**, 045019 (2011).

[198] T. Fischer and R. L. C. Vink, The Journal of Chemical Physics **134**, 055106 (2011).

[199] M. Laradji and G. MacNevin, The Journal of Chemical Physics **119**, 2275 (2003).

[200] Y. Imry and S. K. Ma, Physical Review Letters **35**, 1399 (1975).

[201] Y. Imry and M. Wortis, Physical Review B **19**, 3580 (1979).

[202] M. Aizenman and J. Wehr, Physical Review Letters **62**, 2503s (1989).

[203] F. Franks, *Water: a Matrix for Life*, 2nd edn., Royal Society of Chemistry, Cambridge (2000).

[204] C. A. Angell, W. J. Sichina, M. Oguni, The Journal of Physical Chemistry **86**, 998 (1982).

[205] G. S. Kell, Journal of Chemical & Engineering Data **12**, 66 (1967).

[206] H. Tanaka, The Journal of Chemical Physics **105**, 5099 (1996).

[207] P. Jedlovszky and R. Vallauri, The Journal of Chemical Physics **122**, 81101 (2005).

[208] D. Paschek, A. Rüppert, and A. Geiger, A European Journal of Chemical Physics and Physical Chemistry **9**, 2737 (2008).

[209] P. Pittia and A. Cesàro, Food Biophysics **6**, 183 (2011).

[210] M. Oguni and C. A. Angell, The Journal of Physical Chemistry **87**, 1848 (1983).

[211] D. Corradini, M. Rovere, and P. Gallo, The Journal of Chemical Physics **132**, 134508 (2010).

[212] D. Corradini, M. Rovere, and P. Gallo, The Journal of Physical Chemistry B **115**, 1461 (2011).

[213] O. Mishima, The Journal of Chemical Physics **123**, 154506 (2005).

[214] O. Mishima, The Journal of Chemical Physics **126**, 244507 (2007).

[215] C. Huang, T. M. Weiss, D. Nordlund, K. T. Wikfeldt, L. G. M. Pettersson, and A. Nilsson, The Journal of Chemical Physics **133**, 134504 (2010).

[216] D. Corradini, P. Gallo, and M. Rovere, The Journal of Chemical Physics **130**, 154511 (2009).

[217] D. Corradini, P. Gallo, and M. Rovere, Journal of Physics: Condensed Matter **22**, 284104 (2010).

[218] D. Corradini, S. V. Buldyrev, P. Gallo, and H. E. Stanley, Physical Review E **81**, 061504 (2010).

[219] S. Chatterjee and P. G. Debenedetti, The Journal of Chemical Physics **124**, 154503 (2006).

[220] A. Magno and P. Gallo, The Journal of Physical Chemistry Letters **2**, 977 (2011).

[221] P. Ball P, *Life's Matrix: a Biography of Water*, Farrar, Straus, and Giroux, New York (2000).

[222] P. H. Poole, F. Sciortino, U. Essmann, and H. E. Stanley, Physical Review E **48**, 3799 (1993).

[223] L. Xu, S. V. Buldyrev, C. A. Angell, and H. E. Stanley, Physical Review E **74**, 031108 (2006).

[224] G. Franzese, V. Bianco, and S. Iskrov, Food Biophysics **6**, 186 (2011).

[225] S. V. Buldyrev, Lecture Notes in Physics **752**, 97 (2008).

[226] M. Canpolat, F. W. Starr, M. R. Sadr-Lahijany, A. Scala, O. Mishima, S. Havlin, and H. E. Stanley, Chemical Physics Letters **294**, 9 (1998).

[227] M. R. Sadr-Lahijany, A. Scala, S. V. Buldyrev, and H. E. Stanley, Physical Review Letters **81**, 4895 (1998).

[228] L. Xu, S. V. Buldyrev, N. Giovambattista, C. A. Angell, and H. E. Stanley, The Journal of Chemical Physics **130**, 054505 (2009).

[229] L. Xu, I. Ehrenberg, S. V. Buldyrev, and H. E. Stanley, Journal of Physics: Condensed Matter **18**, S2239 (2006).

[230] P. Kumar, S. V. Buldyrev, F. Sciortino, E. Zaccarelli, and H. E. Stanley, Physical Review E **72**, 021501 (2005).

[231] H. M. Gibson and N. B. Wilding, Physical Review E **73**, 061507 (2006).

[232] E. Lomba, N. G. Almarza, C. Martín, and C. McBride, The Journal of Chemical Physics **126**, 244510 (2007).

[233] G. Franzese, G. Malescio, A. Skibinsky, S. V. Buldyrev, and H. E. Stanley, Nature **409**, 692–695 (2001).

[234] S. V. Buldyrev, G. Franzese, N. Giovambattista, G. Malescio, M. R. Sadr-Lahijany, A. Scala, A. Skibinsky, and H. E. Stanley, *Double-step potential models of fluids - Anomalies and a liquid-liquid phase transition*, in *New Kinds of Phase Transitions:*

Transformation in Disordered Substances, NATO Science Series, series II: Mathematics, Physics and Chemistry, volume 81, page 672, V. V. Brazhkin, S. V. Buldyrev, V. N. Ryzhov, H. E. Stanley, eds., Proceedings of the NATO Advanced Research Workshop, 2002.

[235] G. Franzese, G. Malescio, A. Skibinsky, S. V. Buldyrev, and H. E. Stanley, Physical Review E**66**, 051206 (2002).

[236] G. Malescio, G. Franzese, G. Pellicane, A. Skibinsky, S. V. Buldyrev, and H. E. Stanley, Journal of Physics: Condensed Matter **14**, 2193 (2002),

[237] S. V. Buldyrev, G. Franzese, N. Giovambattista, G. Malescio, M. R. Sadr-Lahijany, A. Scala, A. Skibinsky, and H. E. Stanley, Physica A **304**, 23 (2002).

[238] A. Skibinsky, S. V. Buldyrev, G. Franzese, G. Malescio, and H. E. Stanley, Physical Review E **69**, 061206 (2004).

[239] G. Malescio, G. Franzese, A. Skibinsky, S. V. Buldyrev, and H. E. Stanley, Physical Review E **71**, 061504 (2005).

[240] G. Franzese, Journal of Molecular Liquids **136**, 267 (2007).

[241] A. B. de Oliveira, G. Franzese, P. A. Netz, and M. C. Barbosa, The Journal of Chemical Physics **128**, 064901 (2008).

[242] P. Vilaseca and G. Franzese, The Journal of Chemical Physics **133**, 084507 (2010).

[243] P. Vilaseca and G. Franzese, Journal of Non-Crystalline Solids **357**, 419 (2011).

[244] E. A. Jagla, The Journal of Chemical Physics **111**, 8980 (1999).

[245] E. A. Jagla, Physical Review E **58**, 1478 (1998).

[246] Z. Yan, S. V. Buldyrev, N. Giovambattista, and H. E. Stanley, Physical Review Letters **95**, 130604 (2005).

[247] Z. Yan, S. V. Buldyrev, N. Giovambattista, P. G. Debenedetti, and H. E. Stanley, Physical Review E **73**, 051204 (2006).

[248] Z. Yan, S. V. Buldyrev, P. Kumar, N. Giovambattista, and H. E. Stanley, Physical Review E **77**, 042201 (2008).

[249] L. Xu, F. Mallamace, Z. Yan, F. W. Starr, S. V. Buldyrev, and H. E. Stanley, Nature Physics **5**, 565 (2009).

[250] D. Paschek, Physical Review Letters **94**, 217802 (2005).

[251] S. V. Buldyrev, P. Kumar, P. G. Debenedetti, P. Rossky, and H. E. Stanley, Proceedings of the National Academy of Sciences of the United States of America **104**, 20177 (2007).

[252] S. V. Buldyrev, P. Kumar, S. Sastry, H. E. Stanley, and S. Weiner, Journal of Physics: Condensed Matter **22**, 284109 (2010).

[253] H. E. Stanley, S. V. Buldyrev, G. Franzese, P. Kumar, F. Mallamace, M. G. Mazza, K. Stokely, and L. Xu, Journal of Physics: Condensed Matter **22**, 284101 (2010).

[254] Y. Katayama, T. Mizutani, W. Utsumi, O. Shimomura, M. Yamakata, and K.-i. Funakoshi, Nature **403**, 170 (2000).

[255] Y. Katayama, Y. Inamura, T. Mizutani, M. Yamakata, W. Utsumi, and O. Shimomura, Science **306**, 848 (2004).

[256] G. Monaco, S. Falconi, W. A. Crichton, and M. Mezouar, Physical Review Letters **90**, 255701 (2003).

[257] R. Kurita and H. Tanaka, Science **306**, 845 (2004).

[258] R. Kurita and H. Tanaka, Journal of Physics: Condensed Matter **17**, L293 (2005).

[259] H. Tanaka, R. Kurita, and H. Mataki, Physical Review Letters **92**, 025701 (2004).

[260] G. N. Greaves, M. C. Wilding, S. Fearn, D. Langstaff, F. Kargl, S. Cox, Q. Vu Van, O. Majérus, C. J. Benmore, R. Weber, C. M. Martin, and L. Hennet, Science **322**, 566 (2008).

[261] C. A. Angell, S. Borick, and M. Grabow, Journal of Non-Crystalline Solids **207**, 463 (1996).

[262] D. J. Lacks, Physical Review Letters **84**, 4629 (2000).

[263] M. van Thiel and F. H. Ree, Physical Review B **48**, 3591 (1993).

[264] V. V.‘Brazhkin, E. L. Gromnistkaya, O. V. Stalgorova, and A. G. Lyapin, Rev High Pressure Science & Technology **7**, 1129 (1998).

[265] M. G. Vasin and V. I. Ladýanov, Physical Review E **68**, 051202 (2003).

[266] S. Aasland and P. F. McMillan, Nature **369**, 633 (1994).

[267] M. C. Wilding and P. F. McMillan, Journal of Non-Crystalline Solids **293**, 357 (2001).

[268] M. C. Wilding, C. J. Benmore, P. F. McMillan, Journal of Non-Crystalline Solids **297**, 143 (2002).

[269] E. A. Jagla, Physical Review E **63**, 061501 (2001).

[270] T. Head-Gordon and F. H. Stillinger, The Journal of Chemical Physics **98**, 3313 (1993).

[271] R. Godawat, S. N. Jamadagni, and S. Garde, Proceedings of the National Academy of Sciences of the United States of America **106**, 15119 (2009).

[272] T. Werder, J. H. Walther, R. L. Jaffe, T. Halicioglu, and P. Koumoutsakos, The Journal of Physical Chemistry B **107**, 1345 (2003).

[273] J. Marti, G. Nagy, M. C. Gordillo, and E. Guàrdia, The Journal of Chemical Physics **124**, 094703 (2006).

[274] M. C. Gordillo and J. Marti, Physical Review B **78**, 075432 (2008).

[275] S. V. Buldyrev and H. E. Stanley, Physica A **330**, 124 (2003).

[276] H. J. C. Berendsen, J. P. M. Postma, W. F. van Gunsteren, A. DiNola and J. R. Haak, The Journal of Chemical Physics **81**, 3684 (1984).

[277] P. A. Netz, S. V. Buldyrev, M. C. Barbosa and H. E. Stanley, Physical Review E **73**, 061504 (2006).

[278] D. C. Rapaport, The Journal of Chemical Physics **71**, 3299 (1979).

[279] N. V. Dokholyan, E. Pitard, S. V. Buldyrev, and H. E. Stanley, Physical Review E **65**, R030801 (2002)

[280] S. V. Buldyrev, P. Kumar, P. G. Debenedetti, P. J. Rossky, and H. E. Stanley, Proceedings of the National Academy of Sciences of the United States of America **101**, 21077 (2007).

[281] A. J. Moreno, S. V. Buldyrev, E. La Nave, I. Saika-Voivod, F. Sciortino, P. Tartaglia, E. Zaccarelli, Physical Review Letters **95**, 157802 (2005).

[282] E. Zaccarelli,S. V. Buldyrev,E. La Nave,A. J. Moreno,I. Saika-Voivod, F. Sciortino, P. Tartaglia, Physical Review Letters **94**, 218301 (2005).

[283] C. Davis, H. Nie, and N. V. Dokholyan, Physical Review E, **75**, 051921 (2007).

[284] F. Franks, Biophysics and Biochemistry at Low Temperatures, Cambridge University Press, Cambridge (1985).

[285] T. Taga, M. Senma, K. Osaki, Acta Crystallographica Section B **28**, 3258 (1972).

[286] J. H. Crowe, L. M. Crowe, and S. A. Jackson, Archives of Biochemistry and Biophysics **220**, 477 (1983).

[287] S. L. Lee,A. E. Hafeman, P. G. Debenedetti, B. A. Pethica, and D. J. Moore, Industrial & engineering chemistry research **45**, 5134 (2006).

[288] J. H. Crowe, L. M. Crowe, A. E. Oliver, N. Tsvetkova, W. Wolkers, and F. Tablin, Cryobiology **43**, 89 (2001).

[289] C. H. Robinson, New Phytol **151**, 341 (2001).

[290] G. M. Wang and A. D. J. Haymet, The Journal of Physical Chemistry B **102**, 5341 (1998).

[291] . P. Bordat, A. Lerbret, J.-P. Demaret, F. Affouard, and M. Descamps, Europhysics Letters **65**, 41 (2004).

[292] J. H. Crowe, S. B. Leslie, and L. M. Crowe, Cryobiology **31**, 355 (1994).

[293] J. L. Green. and C. A. Angell, The Journal of Physical Chemistry **93**, 2880 (1989).

[294] P. S. Belton and A. M. Gil, Biopolymers **34**, 957 (1994).

[295] P. Bordat, A. Lerbret, J.-P. Demaret, F. Affouard, and M. Descamps, Europhysics Letters **65**, 41-47 (2004).

[296] A. Lerbret, P. Bordat, F. Affouard, A. Hédoux, Y. Guinet, and M. Descamps, The Journal of Physical Chemistry B **111**, 9410 (2007).

[297] M. C. Vaney, S. Maignan, M. Riès-Kautt, and A. Ducriux, Acta Crystallographica Section D **52**, 505 (1996).

[298] A. D. MacKerell, Jr., M. Feig, and C. L. Brooks, III. Journal of Computational Chemistry **25**, 1400 (2004).

[299] A. D. MacKerell, Jr., D. Bashford, M. Bellott, R. L. Dunbrack, Jr., J. D. Evanseck, M. J. Field, S. Fischer, J. Gao, H. Guo, S. Ha, D. Joseph-McCarthy, L. Kuchnir, K. Kuczera, F. T. K. Lau, C. Mattos, S. Michnick, T. Ngo,D. T. Nguyen, B. Prodhom, W. E. Reiher, III, B. Roux, M. Schlenkrich, J. C. Smith, R. Stote, J. Straub, M. Watanabe, J. Wiórkiewicz-Kuczera, D. Yin, and M. Karplus, The Journal of Physical Chemistry B **102**, 3586 (1998).

[300] O. Guvench, S. N. Greene, G. Kamath, J. W. Brady, R. M. Venable, R. W. Pastor, A. D. Mackerell, Jr. Journal of Computational Chemistry **29**, 2543 (2004).

[301] O. Guvench, E. Hatcher, R. M. Venable, R. W. Pastor and A. D. MacKerell Jr., Journal of Chemical Theory and Computation **5**, 2553 (2009).

[302] H. J. C. Berendsen, J. R. Grigera and T. P. Straatsma, The Journal of Physical Chemistry **91**, 6269 (1987).

[303] B. Hess, C. Kutzner, D. van der Spoel and E. Lindahl, Journal of Chemical Theory and Computation **4**, 435 (2008).

[304] P. Gallo, F. Sciortino, P. Tartaglia, and S.-H. Chen, Physical Review Letters **76**, 2730 (1996).

[305] F. Sciortino, P. Gallo, P. Tartaglia, and S.-H. Chen, Physical Review E **54**, 6331 (1996).

[306] P. Gallo, M. Rovere, and E. Spohr, Physical Review Letters **85**, 4317 (2000).

[307] P. Gallo, M. Rovere, and E. Spohr, The Journal of Chemical Physics **113**, 11324 (2000).

[308] G. N. Jr. Phillips, B. M. Pettitt, Protein Science **4**, 149 (1995).

[309] A. R. Bizzarri and S. Cannistraro, The Journal of Physical Chemistry B, **106**, 6617 (2002)

[310] C. Rocchi, A. R. Bizzarri, S. Cannistraro, Physical Review E **57**, 3315 (1998).

[311] A. E. Garcia, and L. Stiller, Journal of Computational Chemistry **14**, 1396 (1993).

[312] C. Rocchi, A. R. Bizzarri, and S. Cannistraro, Chemical Physics 1997, **214**, 261 (1997).

[313] M. Paolantoni, L. Comez,M. E. Gallina, P. Sassi, F. Scarponi, D. Fioretto, and A. Morresi, The Journal of Physical Chemistry B **113**, 7874 (2009).

[314] M. E. Gallina, L. Comez, A. Morresi, M. Paolantoni, S. Perticaroli, P. Sassi, and D. Fioretto, The Journal of Chemical Physics **132**, 214508 (2010).

[315] J. Malsam, A. Aksan, The Journal of Physical Chemistry B **113**, 6792 (2009).

Curriculum Vitae

Elena G. Strekalova

Office Address

590 Commonwealth Avenue
Department of Physics, Boston University
Boston, MA 02215, U.S.A.

Office: (617)353-3891
Mobile:(617)960-7610
E-mail: elena@bu.edu

EDUCATION

- 2012 (expected May 2012): Doctor of Philosophy (Physics), Boston University, Boston, MA 02215 USA
(Thesis Advisor: H. Eugene Stanley).
- 2006: Master of Science (Chemistry) *summa cum laude*, University of Massachusetts Boston, Boston, MA 02125 USA
- 2006: Bachelor of Science (Chemistry and Physics) *summa cum laude*, Biology Minor, University of Massachusetts Boston, Boston, MA 02125 USA

LIST OF PUBLICATIONS

1. E. G. Strekalova, J. Luo, H. E. Stanley, S. V. Buldyrev, G. Franzese, *Nanoparticle confinement in anomalous liquids*,preprint available arXiv:1107.1926 (2011).

2. E. G. Strekalova, M. G. Mazza, H. E. Stanley, and G. Franzese, *Hydrophobic nanoconfinement suppresses fluctuations in supercooled water*, Journal of Physics: Condensed Matter, **24**, 064111 (2012).

3. E. G. Strekalova, D. Corradini, M. G. Mazza, S. V. Buldyrev, P. Gallo, G. Franzese, and H. E. Stanley, *Effect of Hydrophobic Environments on the Hypothesized Liquid-Liquid Critical Point of Water*, Journal of Biological Physics, **38**, 97 (2011).

4. E. G. Strekalova, M. G. Mazza, H. E. Stanley, and G. Franzese, *Large Decrease of Fluctuations for Supercooled Water in Hydrophobic Nanoconfinement*, Physical Review Letters **106**, 145701 (2011).

5. G. Franzese, A. Hernando-Martinez, P. Kumar, M. G. Mazza, K. Stokely, E. G. Strekalova, F. de los Santos, H. E. Stanley, *Phase Transitions and Dynamics in Bulk and Interfacial Water*, Journal of Physics: Condensed Matter **22**, 284103 (2010).

6. M. G. Mazza, K. Stokely, E. G. Strekalova, H. E. Stanley, and G. Franzese, *Cluster Monte Carlo and numerical mean field analysis for the water liquid-liquid phase transition*, Computer Physics Communications **180**, 497502 (2009).

ADDITIONAL RESEARCH EXPERIENCE

- 2004-2006: Masters thesis in Inorganic Physical Chemistry Studied the stability of transition metal complexes of bis(1,4,7-triazacyclononane) ligands with unusual stereochemistry. Synthesised and structurally characterized via X-ray diffraction the active sites of metalloproteins, binuclear metal complexes. University of Massachusetts Boston, Boston, MA 02125 USA
  (Thesis Advisor: Leverett Zompa).

- 2004: Studied the kinetics of catalytic decomposition of peroxynitrite using stopped-flow spectrophotometry and NMR spectroscopy. Princeton University, Princeton, NJ
  (Research Advisor: John T. Groves)

- 2003-2004: Study of patient's operative reports to determine the rate of tympanic membrane perforation following tympanostomy tube removal with and without Gelfilm myringoplasty, and to examine patient characteristics that may predispose to failure of the tympanic membrane closure. Massachusetts Eye and Ear Infirmary, Boston, MA
  (Research Advisor: Michael J. Cunningham)

TEACHING EXPERIENCE AT BOSTON UNIVERSITY

- PY 211 Discussion and Laboratory: Mechanics and Thermodynamics (Undergraduate).
- PY 212 Laboratory: Electricity and Magnetism (Undergraduate).

TEACHING EXPERIENCE AT UNIVERSITY OF MASSACHUSETTS BOSTON

- Laboratory: Organic Chemistry (Undergraduate).
- Laboratory: Freshman Chemistry (Undergraduate).
- Group tutoring: Calculus, Physics, Biology and Chemistry (Undergraduate).

TALKS/PRESENTATIONS

- “Confinement of anomalous liquids in nanoporous matrices”, Talk at APS March Meeting 2012, Boston Convention and Exhibition Center, Boston MA, USA. 02/29/2012.
- “Butterfly thin films”, Invited talk, Shapiro Family Science Live! Stage, Museum of Science, Boston MA, USA. 02/15/2012.
- “Nanoparticle confinement in anomalous liquids”, Seminar speaker, Department of Civil and Environmental Engineering, Massachusetts Institute of Technology, Cambridge MA, USA. 01/30/2012.
- “Effects of hydrophobic confinement on the hypothesized liquid-liquid critical point of water ”, Colloquium speaker, Department of Physics, University of Massachusetts Boston, Boston MA, USA. 12/07/2011.
- “Effects of structure of the confinement matrix on liquid-liquid phase transition”, Poster presentation, Perspectives and Challenges in Statistical Physics and Complex Systems for the Next Decade, Natal, Rio Grande do Norte, Brazil. 11/10/2011.
- “‘Effects of structure of the confinement matrix on liquid-liquid phase transition”, Seminar speaker, Department of Physics, Boston University, Boston MA, USA. 10/19/2011.
- “Large decrease of fluctuations for supercooled water in hydrophobic nanoconfinement”, Poster presentation, HES70:Horizons in Emergence and Scaling the H.Eugene Stanley Symposium, Boston University, Boston MA, USA. 03/18/2011.
- “Phase diagram of supercooled water in a disordered matrix of hydrophobic nanoparticles” Poster presentation, Water & Aqueous Solutions Gordon Research Conference, Holderness NH, USA. 08/10/2010.
- “Structural study of copper(II) complexes of bis(1,4,7-triaza-cyclononane) ligands with polymethylene bridging groups”, Seminar speaker, Department of Chemistry, University of Massachusetts Boston, Boston MA, USA. 03/08/2005.

AWARDS

- Provost Award, Science and Engineering poster competition, Boston University, Boston MA, USA. 2011
- University Honors, University of Massachusetts Boston, Boston MA, USA. 2006
- Departmental Honors in Physics and Chemistry, University of Massachusetts Boston, Boston MA, USA. 2006
- Ethel and Herman Rosansky Chemistry Award, University of Massachusetts Boston, Boston MA, USA. 2005
- ACS Award in Analytical Chemistry, University of Massachusetts Boston, Boston MA, USA. 2004
- Undergraduate Summer Research Fellowship, Princeton University, Princeton NJ, USA. 2004
- Litton Industries Merit Award, University of Massachusetts Boston, Boston MA, USA. 2003
- Women Merit Award, University of Massachusetts Boston, Boston MA, USA. 2003
- Director's List for consistent summa cum laude performance, University of Massachusetts Boston, Boston MA, USA. 2002-2006
- Dean's list, University of Massachusetts Boston, Boston MA, USA. 2001-2006